Entropy as a Material Response to Fatigue in Metals and Related Thermographic Assessment

Dissertation
zur Erlangung des akademischen Grades
des Doktors der Ingenieurwissenschaften
der Naturwissenschaftlich-Technischen Fakultät
der Universität des Saarlandes

von

Zhenjie TENG

Saarbrücken
2022

Tag des Kolloquiums: 25.03.2022

Dekan: Prof. Dr. rer. nat. Jörn Walter

Berichterstatter: Prof. Dr.-Ing. Christian Boller

Prof. Dr.-Ing. Peter Starke

Akad. Mitarbeiter: Dr.-Ing. Frank Aubertin

Vorsitz: Prof. Dr.-Ing. Dirk Bähre

“We are all in the gutter,”

— Oscar Wilde (A.D. 1854 – 1900)

Preface

This dissertation is submitted to Saarland University to fulfill the doctoral degree requirements. This work has been carried out in the period from Oct. 2017 to Sep. 2021 under the supervision of Prof. Dr. -Ing. Christian Boller and Prof. Priv.-Doz. Dr. -Ing. habil. Peter Starke. The main experimental and theoretical work was conducted at the Chair of Non-Destructive Testing and Quality Assurance (LZfPQ) at the Department of Materials Science within the Faculty of Natural Sciences and Technology at Saarland University.

The dissertation was financially supported by the China Scholarship Council (Grant No. 201706240269).

The dissertation comprises a summary of the Ph.D. work and five articles that have been published in scientific journals.

Zhenjie Teng
Saarbrücken, Germany

Declaration of Originality

I declare that this dissertation does not incorporate without acknowledgement any material previously submitted for a degree or diploma in any university. Information derived from the published and unpublished work of others has been acknowledged in the text and references are given in the list of sources.

Zhenjie Teng

Saarbrücken, Germany

Acknowledgments

The four-year funding supporting this dissertation has been fully sponsored by China Scholarship Council, which is highly appreciated.

Foremost, I would like to express my sincere gratitude to my supervisor, Prof. Christian Boller, who allowed me to join his chair (Chair of Non-Destructive Testing and Quality Assurance) and shared his scientific research experience. I appreciate his help and guidance in my research work. During the past years, I saw the love and persistence he fell in scientific science, which will encourage me in the years to come.

I am then equally thankful to my co-supervisor, Prof. Peter Starke, who gave me the scientific support, without whom this doctoral degree project could not have been established. I spent most of the time in his group (WWHK in Kaiserslautern). Thanks to his guidance and patience, I was fortunate to finish many achievements, including publications and the presentation at the conference on Fatigue 2021, UK. I appreciate him more than he knows.

My colleague Haoran Wu is acknowledged. He was the right one who helped me in testing details during my doctoral journey and the German version of the abstract for this thesis was translated by him. My sincere gratitude goes to those who helped or encouraged me in the past years, including but not limited to Bixian Ying, Yingke Wu, Po Yuan, Ping Liu, Lei Yi, Hanqing Liu, Zhen Zhang, Yukang Wang, Haoran Jiang, Yunguang Ye, Yifan Li, Ruth Acosta, Tobias Bill, Denis Baczynski, Srinivasa Raghuraman, and many others.

Last but not least, I would like to explicitly acknowledge my parents, sister, and brother-in-law for their comprehension and support during my studying period.

Zhenjie Teng
Saarbrücken, Germany

List of Papers

- **Z.J. Teng,** H. Wu, S. Pramanik, K.-P. Hoyer, M. Schaper, H.L. Zhang, C. Boller, P. Starke. Characterization and analysis of plastic instability in an ultrafine-grained medium Mn TRIP steel. *In manuscript.*
- **Z.J. Teng**, H. Wu, C. Boller, P. Starke. Thermodynamic entropy as a marker of high-cycle fatigue damage accumulation: Example for normalized SAE 1045 steel. *Fatigue & Fracture of Engineering Materials & Structures*. 2020; 43:2854-2866.
- **Z.J. Teng**, H. Wu, C. Boller, P. Starke. A unified fatigue life calculation based on intrinsic thermal dissipation and microplasticity evolution. *International Journal of Fatigue*. 2020; 131:105370.
- **Z.J. Teng**, H. Wu, C. Boller, P. Starke. Thermography in high cycle fatigue short term evaluation procedures applied to a medium carbon steel. *Fatigue & Fracture of Engineering Materials & Structures*. 2020; 43:515-526.
- **Z.J. Teng**, H. Liu, Q. Wang, Z. Huang, P. Starke. Fretting behaviors of a steel up to very high cycle fatigue. *Wear*. 2019; 438-439:203078.
- **Z.J. Teng**, H. Wu, Z. Huang, P. Starke. Effect of mean stress in very high cycle fretting fatigue of a bearing steel. *International Journal of Fatigue*. 2021; 149:106262.
- H. Wu, T. Bill, **Z.J. Teng**, S. Pramanik, K.-P. Hoyer, M. Schaper, P. Starke. Characterization of the fatigue behaviour for SAE 1045 steel without and with load-free sequences based on non-destructive, X-ray diffraction and transmission electron microscopic investigations. *Materials Science & Engineering A*. 2020; 139597.
- Z. Huang, Z. Zhang, **Z.J. Teng**, M.K. Khan, Q. Wang, J. Wang. Effect of fretting damage on characteristics of high strength bearing steel up to very high cycle fatigue. *Engineering Fracture Mechanics*. 2019; 217:106526.

Table of Contents

Preface I
Declaration of Originality III
Acknowledgments V
List of Papers VII
Table of Contents IX
Abstract XI
Kurzfassung XIII
List of Abbreviations XV
PART I 1
1. Motivation and Objectives 3
1.1 Introduction 3
1.2 Objectives and scope 7
1.3 Dissertation overview 8
2. State of the Art 10
2.1 Difference between quasistatic and fatigue failure 10
2.2 High cycle fatigue 10
2.3 Fatigue damage mechanics 12
2.4 Infrared thermography 16
2.5 Magnetic Barkhausen noise 38
3. Materials and Methods 41
3.1 Materials 41
3.2 Mechanical testing 43
3.3 NDT-methods 44
4. Main Results 46
4.1 Fatigue testing 46
4.2 Quasistatic tensile testing 48

5. Conclusions and Outlooks....51
6. Summary of Papers....53
7. Contribution to Science....57
Reference....60
PART II....71
PAPER 1....73
PAPER 2....99
PAPER 3....125
PAPER 4....153
PAPER 5....180
Scientific Curriculum Vitae....202

Abstract

Entropy as a Material Response to Fatigue in Metals and Related Thermographic Assessment

By Zhenjie Teng

The dissertation comprehensively proposes multi non-destructive testing methods investigation in mechanical degradation of metallic materials. First, high cycle fatigue of an unalloyed medium carbon steel SAE1045 is quantified investigated through thermographic measurement; a short-term evaluation procedure is proposed based on the intrinsic thermal dissipation model to determine the S-N curves by performing two constant amplitude tests and one load increase test. Second, a unified approach is developed by evaluating the evolution of intrinsic dissipation and microplasticity. This plasticity is derived from temperature and is correlated to the fatigue process and related to fatigue life. Furthermore, a modified fracture fatigue entropy (FFE) method is modeled to evaluate the fatigue damage. It is shown that the FFE can be better used as an index to trace the fatigue damage as an irreversible degradation of a metallic material of its non-linearity. Finally, the mechanical and magnetic behavior of an ultrafine-grained medium manganese transformation-induced plasticity steel is investigated in its plastic instability. Lüders bands are characterized by digital image correlation and magnetic Barkhausen noise (MBN), and the final results show that MBN can be used as a potential means for the non-destructive evaluation for the strengthening of this steel.

Keywords: Mechanical Degradation; Intrinsic Dissipation; Fatigue Life Evaluation; Plastic Instability; Non-destructive Testing

Kurzfassung

Entropie als Materialreaktion auf Ermüdung in Metallen und damit verbundene thermografische Bewertung

By Zhenjie Teng

In der Dissertation werden mehrere zerstörungsfreie Prüfverfahren zur Untersuchung der mechanischen Degradation metallischer Werkstoffe vorgeschlagen. Erstens wird das Ermüdungsverhalten in dem Zeitfestigkeitsbereich (engl. high cycle fatigue) eines unlegierten Kohlenstoffstahls (SAE1045/C45E) durch thermografische Messungen quantifiziert ermittelt, wobei ein Kurzzeitverfahren zur Lebensdauerberechnung abgeleitet wird, das auf dem Modell der intrinsischen Wärmedissipation basiert, sodass die Bestimmung der Wöhlerkurven mit zwei Einstufenversuchen und einem Laststeigerungsversuch ermöglicht wird. Darüber hinaus wird ein einheitlicher Ansatz entwickelt, indem die Entwicklung der intrinsischen Dissipation und der Mikroplastizität bewertet wird. Diese Plastizität wird hierbei von der Temperatur abgeleitet, mit dem Ermüdungsprozess korreliert und auf die Ermüdungslebensdauer bezogen. Zudem wird eine modifizierte Fracture Fatigue Entropy-Methode (FFE) modelliert, um die Ermüdungsschädigung zu evaluieren. Schließlich wird das mechanische und magnetische Verhalten in der plastischen Instabilität eines ultrafeinkörnigen TRIP-Stahls mit mittlerem Mangangehalt untersucht. Lüders-Bänder werden durch digitale Bildkorrelation (DIC) und magnetisches Barkhausenrauschen (MBN) charakterisiert. Die Ergebnisse zeigen, dass MBN als potenzielles Mittel für die zerstörungsfreie Bewertung der Festigkeit dieses Stahls verwendet werden kann.

Schlagwörter: mechanische Degradation; intrinsische Dissipation; Ermüdungslebensdauerberechnung; plastische Instabilität; zerstörungsfreie Prüfung

List of Abbreviations

CAT	constant amplitude test
CDM	continuum damage mechanics
DIC	digital image correlation
DIMT	deformation-induced martensitic transformation
EBSD	electron backscatter diffraction
ELCF	extremely low cycle fatigue
FFE	fatigue fracture entropy
HCF	high cycle fatigue
IRT	infrared thermography
LCF	low cycle fatigue
LIT	load increase test
MBN	magnetic Barkhausen noise
MOKE	magneto-optical Kerr effect microscopy
NDT	non-destructive testing
PHYBAL	physically based fatigue life
PSB	persistent slip band
SteBLife	step-bar fatigue life approach
STEP	short-term evaluation procedure
StrainLife	strain-based fatigue life calculation
StressLife	stress-based fatigue life calculation
TEM	transmission electron microscopy
TRIP	transformation-induced plasticity
UFG	ultrafine-grained medium
VHCF	very high cycle fatigue
XRD	X-ray diffraction

PART I

1. Motivation and Objectives

1.1 Introduction

Fatigue and tensile loadings are very common in engineering applications, which can result in mechanical degradation and further change in the integrity of material or structural properties. More serious, the component can no longer serve in the intended manner as it was initially designed because of the probabilistic mechanical failure. Since stress and strain as well as time are the factors that play an essential role in mechanical degradation, the research of proposing new models of fatigue life-, fatigue damage evaluation, and plastic instability of medium Mn transformation-induced plasticity steel that based on non-destructive testing (NDT) are the main points investigated in this thesis. In the following sections, a brief description of the related degradation process will be given.

1.1.1 Fatigue

Metallic materials are the best choice for many infrastructure applications due to these materials' excellent synergy between strength and ductility. However, these structural applications are easier to be affected by the external alternating loadings, and the essence is that the material must suffer cyclic loads, and such stress can cause damage or even failure in those applications after a certain number of cycles, which is also considered as fatigue [1]. The official definition of fatigue used herein is cited from American Society for Testing and Materials (ASTM E206-72) [2]: "the development process of local and permanent structural changes of materials that are subjected to disturbance load at a certain point and undergo crack or complete fracture after sufficient cyclic loading." The fatigue failure, normally, will plague all the metals, and thus, it is essential to investigate their fatigue behavior.

Time goes back to the first industrial revolution. With the progress of technology, especially the improvement of steam engines, traditional manual labor was gradually replaced by mechanized production, and steel materials have been widely used. Steel structures will undergo fatigue damage during the service period due to the cyclic load. Especially the railway traffic accident caused by the fatigue fracture of the train axle in

1842, the event “Catastrophe ferroviaire de Meudon” (as shown in Fig. 1-1) killed at least 55 passengers in France [4]. After that, it has aroused people's attention to the fatigue failure problem.

Fig. 1-1 Schematic drawing of the event “Catastrophe ferroviaire de Meudon” [3].

According to the literature [5], the German engineer August Wöhler (1819-1914), as shown in Fig. 1-2, was the first to systematically study the fatigue life of railway wheel axles under cyclic loadings. He found that the fatigue failure of metal materials still occurs under load conditions much lower than their static strength. Under different cyclic loading conditions, the material can withstand the different cyclic load cycles. The diagram showing the number of cycles to failure of specimens fatigued under the-

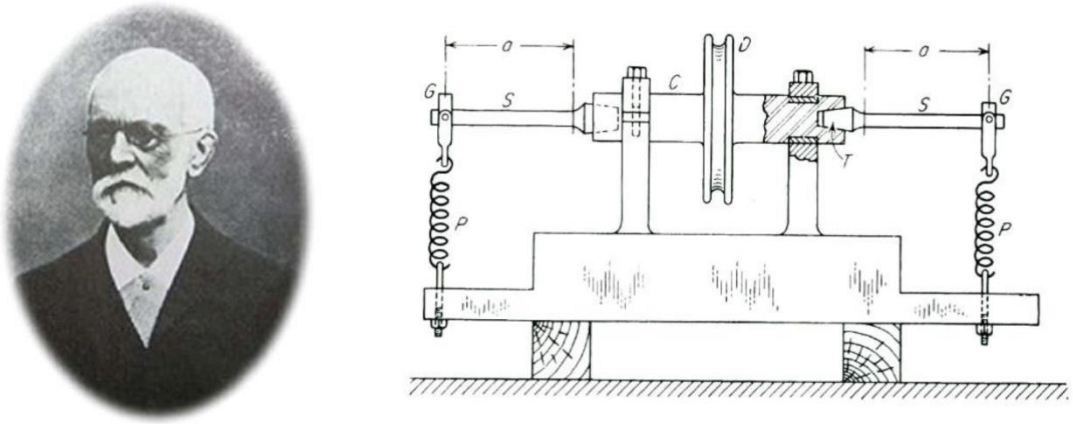

Fig. 1-2 August Wöhler and the schematic fatigue system [6].

same loading conditions but different load levels are named as “Wöhler-curves”

according to his name, or “S-N curves” in the international terminology, where S and N are the stress and number of cycles to failure [6], respectively. Since then, scholars and engineers have made long-term efforts to understand fatigue better and tried to control it with near to 200 years’ development. They accumulated rich experience in the understanding of fatigue mechanisms, fatigue life prediction, and anti-fatigue design.

Fatigue fracture is an important and prevalent failure mode that occurs in mechanical equipment and engineering structures. There are no apparent signs on the surface of an element or structure before fatigue fracture occurs, e.g., macroscopic plastic deformation or macroscopic cracks. The sudden failure often brings disastrous results to the safety production of industrial projects, causing significant economic losses and enormous casualties [7], e.g.,

- Around World War II, about 20 "Wellington" heavy bombers crashed in the UK.
- Between 1951-1954, the British "Pigeon" aircraft and the “Comet” jetliner crashed.
- The DC-10 large passenger plane crashed after taking off at Chicago O’Hare International Airport in 1979.
- In 1985, the JAL flight 123 passenger plane of Japan Airlines crashed due to cracking of the tail bulkhead.
- In 2002, a Boeing 747 of Taiwan's China Airlines suddenly disintegrated over the Taiwan Strait, killing 225 people on board.
- On 20th February this year, after the United Airlines passenger plane took off from Denver International Airport, the right engine (PW4000-112) shell disintegrated, exploded, and caught fire. Fortunately, no casualties were caused. According to the National Transportation Safety Board (NTSB) survey, the damaged engine fan blade was related to metal fatigue.

Thus, the investigations aforementioned found that those catastrophic accidents are closely related to the local metal fatigue failure. It is estimated that 80% of the failures of engineering alloys are due to fatigue [8]. The economic loss caused by fatigue fracture has reached 6-8% of gross national product per year of the United States, Japan, the European Community, and other countries and regions [9]. Therefore, the fatigue

failure of materials has been a topic of research.

Through the long-term research on the fatigue behavior of metal materials, researchers have accumulated a series of experimental data and fundamental theories related to fatigue. One of the most important findings is that ferrous metals such as structural steel exhibit significant fatigue limits in the 10^6-10^7 cycle life range. Through the comparative analysis of many fatigue test data, people have established the proportional relationship between the fatigue limit and the material's tensile properties. It is generally believed that the fatigue strength of structural steel at 10^7 cycles is approximately equal to half of the material's tensile strength, and the fatigue limit of non-ferrous metal materials is about 1/3 of its tensile strength [10].

1.1.2 Plastic instability

During mechanical loading, e.g., tensile, fatigue, some metallurgical instabilities can produce Lüders bands, Portevin-Le Chatelier bands, twinning, and/or phase transformation [11-14]. Some plastic instabilities can cause the crystallographic structure to change, and others are attributed to the solute atoms spreading over the crystal lattice [15].

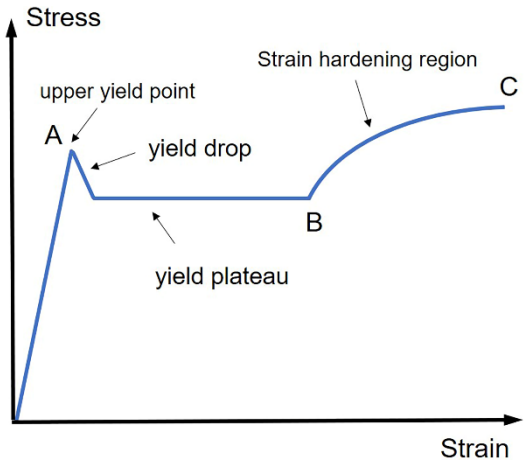

Fig. 1-3. The schematic diagram for Lüders phenomenon [15].

Typically, when loading metallic materials such as carbon steels, there are some inflection points on the stress-strain curve as shown in Fig. 1-3. The yield stress continuously decreases from the upper yield point to the lower yield point. The phenomenon of yield point corresponds to the dislocation glide, dislocation multiplication, and dislocation velocity. It is attributed to the local yielding. This also

includes the adjacent areas where the local plastic strain changes. Such a phenomenon can also be regarded as non-uniform/ discontinuous yielding. After that, the yield point elongation is followed, where the strain increases while the stress stays constant or changes roughly. Lüders propagation occurs typically in this yield plateau. It is proposed that the interstitial atoms, e.g., carbon and nitrogen, cause Lüders strain through the formation of the Cottrell atmosphere during the quasi-static tensile deformation [16]. In Cottrell atmospheres, the interstitial atoms can segregate to the dislocations and pin them in the place to reduce the energy of lattice distortion. During the stage of Lüders band propagation, there are free dislocations in the elastic zones, whereas the Lüders band areas have high dislocation density. The upper yield stress is designated as the nucleation stress of the Lüders band, while the lower yield stress is regarded as the growth stress.

As a kind of plastic instability or localized deformation behavior, the Lüders band in the tensile test is not desired in cases for automotive applications. Since such a behavior can deteriorate the surface quality of the material and result in an unexpected weakening of the material's structural stability and even premature failure in some cases [17], hence, this plastic instability problem has been investigated previously by a considerate number of studies with different characterization methods, e.g., digital image correlation (DIC) [18], neutron diffraction [19], infrared thermography (IRT) [17], Electron Back Scatter Diffraction (EBSD) [20], X-ray diffraction (XRD) [21], as well as transmission electron microscopy (TEM) [22]. Nowadays, non-destructive testing (NDT) is in huge demand due to its enhanced capabilities for evaluating mechanical properties. With many of those techniques, the operation becomes increasingly intuitive, the measurement is non-invasive, and can even be contactless. Amongst the wide range of NDT techniques, magnetic Barkhausen noise (MBN) has been chosen to characterize the plastic instability of the material along tensile tests, which will be presented here.

1.2 Objectives and scope

The traditional approach to get an S-N dataset for materials in the range of 10^4 to 10^7 cycles usually requires ~20 to 30 specimens under 4 to 5 stress levels and it takes about two months to get the fatigue data at a relatively low frequency. It is very specimen-, time-, and cost-consuming. Therefore, it finally seeks a more effective method. Among

them, the non-destructive testing (NDT) methods make up-and-coming prospects for the short-term evaluation procedures (STEPs) of fatigue life evaluation or monitoring the structural health of the components.

The NDT methods usage in obtaining properties of mechanical degradation under cyclic and quasi-static tensile loading can provide more specific information concerning the mechanical deformation behavior of the material. The physical quantities measured by NDT methods can link cross-effects and can be bridged with the microstructural changes of the material obtained during fatigue and tensile loading.

Within the scope of this doctoral thesis, thermography as an NDT technique was used to build new approaches of the STEP for fatigue life calculation, and fatigue damage was developed and verified on specimens of the SAE 1045 steel. In addition to the fatigue tests, some other NDT methods, such as MBN and DIC, were successfully used to make an exploration to investigate the plastic instability of a medium Mn steel during the tensile test. As an 'extensive' characterization, TEM was performed to further investigate the fatigue and tensile behavior of the materials, which is of decisive importance for the damage of a material or a component.

1.3 Dissertation overview

The doctoral thesis is a collection of research papers that obtained during the four-year research period at the Char of Non-Destructive Testing and Quality Assurance (LZfPQ) at Saarland University and the Materials Science and Testing Group (WWHK) at the University of Applied Sciences Kaiserslautern.

Part I is the introduction to the dissertation including the research motivation and objectives, state of the art, and followed by the main results from the Ph.D. work. Part II includes research papers (four have been published, and one has been submitted to a scientific journal), those five papers are listed below and the summary of the papers is given in Chapter 6. The highlights or the contribution of the papers to science are also presented in Chapter 7.

Journal Papers:

- **Z.J. Teng**, H. Wu, C. Boller, P. Starke. Thermography in high cycle fatigue short

term evaluation procedures applied to a medium carbon steel. Fatigue & Fracture of Engineering Materials & Structures. 2020; 43:515-526.

- **Z.J. Teng**, H. Wu, C. Boller, P. Starke. A unified fatigue life calculation based on intrinsic thermal dissipation and microplasticity evolution. International Journal of Fatigue. 2020; 131:105370.

- **Z.J. Teng**, H. Wu, C. Boller, P. Starke. Thermodynamic entropy as a marker of high-cycle fatigue damage accumulation: Example for normalized SAE 1045 steel. Fatigue & Fracture of Engineering Materials & Structures. 2020; 43:2854-2866.

- H. Wu, T. Bill, **Z.J. Teng**, S. Pramanik, K.-P. Hoyer, M. Schaper, P. Starke. Characterization of the fatigue behavior for SAE 1045 steel without and with load-free sequences based on non-destructive, X-ray diffraction and transmission electron microscopic investigations. Materials Science & Engineering A. 2020; 139597.

- **Z.J. Teng**, H. Wu, S. Pramanik, K.-P. Hoyer, M. Schaper, H.L. Zhang, C. Boller, P. Starke. Characterization and analysis of plastic instability in an ultrafine-grained medium Mn TRIP steel. In manuscript.

The statement of author contributions for Zhenjie Teng in each paper is supplied as a supplementary document and which has been signed by all co-authors.

2. State of the Art

2.1 Difference between quasistatic and fatigue failure

From the aforementioned information, we can have a shallow knowledge of the concept of fatigue. Here follows the difference between the fatigued and traditional quasistatic failure of the mechanical degradation:

- The quasistatic failure is generally under the maximum load condition. In comparison, the fatigue failure is under the status of repeated loads, which will not happen quickly.
- The failure will not happen when the quasistatic stress is lower than the yield limit. However, the fatigue failure can still occur when the alternating stress is much less than the yield stress after a specific number of cycles.
- Quasistatic failure usually has obvious plastic deformation that can be observed by the naked eye. Fatigue failure usually has no obvious signs of external plastic deformation. It is not easy to detect in advance, which indicates that fatigue failure has great potential of danger.
- The fracture surface of quasistatic failure usually presents a dimple. On the fatigue damaged part, there are always two regional characteristics, one part is smooth due to repeated deformation, named “crack source”, and the other part is a dimple.
- The resistance to quasistatic damage mainly depends on the material itself. In contrast, the resistance to fatigue damage is related to the material’s chemical composition/mechanical properties, shape geometry and surface condition of the specimen or component, and external environment of service, etc.

2.2 High cycle fatigue

The number of cycles of stress or strain experienced by an element or a sample when fatigue failure occurs under cyclic loading usually is named fatigue life, N_f, as aforementioned. Historically, based on the lifetime of fatigue failure, the fatigue life

estimations have been classified into categories of low cycle fatigue (LCF) and high cycle fatigue (HCF), taking a lifetime of 10^4 cycles as the transition point [23]. More detailed, the fatigue process within a lifetime that fewer than 10^2 cycles is regarded as the extremely-low-cycle fatigue (ELCF) [23], and oppositely, lifetime higher than 10^7 cycles is termed as the very-high-cycle fatigue (VHCF) [24]. Normally, the test of LCF is controlled in strain, and HCF is controlled in stress. The fatigue tests are usually implemented by a conventional hydraulic fatigue machine, which comprises a power group, test control system, test frame, sensors, etc. One of the sensors, the extensometer, can measure the deformation of the specimen, especially necessary for LCF.

The fatigue life depends on material's intrinsic properties, extrinsic applied stress or strain amplitude, and other environmental conditions, e.g., fretting, high temperature, corrosion, and vacuum. Generally, the higher strength of the material or the lower stress or strain level applied, the longer the fatigue life will be, and vice versa. The curve representing this applied stress level versus the fatigue life of the material becomes the S-N curve. The S-N curve usually takes the fatigue life as the abscissa and the cyclic stress amplitude as the ordinate. The most classical fatigue description for the relationship between stress and lifetime in the HCF regime, the Wöhler-curve, is formulated as a straight line in the bi-logarithmic coordinates:

$$\lg N_f = -m \cdot \lg \sigma_a + A \tag{2-1}$$

where m and A are material constants and are determined by ASTM [25].

For a power-law expression, it can be written as:

$$\sigma_a = \sigma_f' \cdot (2N_f)^b \tag{2-2}$$

where σ_f' is the fatigue strength coefficient,

$$\sigma_f' = 10^{(A+\lg 2)/m} \tag{2-3}$$

and b is the fatigue strength exponent,

$$b = -1/m \tag{2-4}$$

During the fatigue test, the metals can undergo cyclic hardening or softening. Cyclic

plastic deformation happens through the metals. Generally, the metals respond differently to the stress amplitude than to the strain amplitude cycling. A bi-logarithmic map of stress versus fatigue life is recognized in the HCF regime by separating the total strain from the elastic strain and plastic strain. A classical relation of strain range vs. fatigue life is well expressed by the Manson-Coffin law [26,27]. The law describes the fatigue behavior of metals in the LCF and HCF regime and is given as follows:

$$\frac{\Delta\varepsilon_e}{2} = \sigma_f' \cdot (N_f)^b \tag{2-5}$$

$$\frac{\Delta\varepsilon_p}{2} = \varepsilon_f' \cdot (N_f)^c \tag{2-6}$$

$$\frac{\Delta\varepsilon}{2} = \frac{\Delta\varepsilon_e}{2} + \frac{\Delta\varepsilon_p}{2} = \varepsilon_f' \cdot (N_f)^c + \sigma_f' \cdot (N_f)^b \tag{2-7}$$

where ε_e and ε_p are the elastic and plastic strains, ε_f' and c are the fatigue ductility coefficient and exponent, respectively. The ductile metals, with high ε_f', give high resistance in the low cycle regime and the strong metals, with high σ_f', are preferred in the high cycle regime.

Fatigue failure of alloys is staged [28]: (1) dislocation and persistent slip band (PSB) formed, (2) dislocations nucleated with the transition to micro-cracks, (3) micro-cracks propagated perpendicular and then towards the maximum shear stress direction, (4) macro-cracks formed and resulted in the generation of high-stress intensities at the crack tips. Each of the stages is interesting and important; however, the relative contribution to the overall fatigue life is dependent on the external loading conditions. In the HCF regime, the cyclic stress is lower than the monotonic yield strength. Most of the fatigue life is consumed by plastic localization and critical size fatigue cracks [29]. In many structure applications, but not all, the cycles of cyclic stress decrease in the HCF regime. In that case one needs to pay attention to the properties of HCF.

2.3 Fatigue damage mechanics

Metal fatigue is usually discussed as a cumulative damage process due to the permanent nature of the process namely, such as fatigue degradation to be irrecoverable [30]. The intrinsic mechanism of fatigue damage is very complicated, e.g., cyclic

softening/hardening, phase transformation, dislocation migration, macro band formation, etc. Therefore, the intrinsic damage mechanism contributes to the microplastic deformation, and the accumulated local plastic deformation will finally lead to the crack initiation. After that, the crack can further propagate until the component reaches the final fracture. To sum up, the fatigue damage of metals during a material's entire lifetime can be classified into three phases, represented such as (i) crack initiation, (ii) crack propagation, and (iii) final fracture. A more detailed description of crack initiation and propagation is given as follows:

- Crack initiation: There is no macrocrack in the initial stage of fatigue damage. The permanent change in microstructure occurs within this period. This change will lead to the initiation of microcracks due to the accumulation of local microplasticity. The stress concentration is resulted from lattice defects, e.g., dislocations, vacancies, boundaries. Therefore, the microstructure participates in the fatigue process. According to [31,32], the micromechanical models of crack initiation include dislocation and slip band micro-cracking at the grain boundaries because of dislocation pile-ups. Some of the microcracks stop propagate, and some continue to grow, and new cracks may form. Finally, the main crack generates and plays an essential role in the lifetime of the component. Such fatigue process period can be regarded as an early stage of fatigue. In conclusion, this period includes the initial microstructural change, leading to fatigue accumulation, e.g., lattice defects, slip band formation, and fatigue cracks initiation.

- Crack propagation: The crack propagation occurs after the crack initiation, and it can be observed on the fracture surface by the striations. The main focus of crack propagation is the growth of a single dominant crack, which plays a disadvantage in the residual fatigue life. Namely, the residual lifetime and fatigue failure relies on the dynamics of crack growth. The related fatigue damage mainly accumulates in the crack area in a localized manner. Fracture mechanics is developed during this phase, and some approaches are proposed to predict the residual lifetime. Among them, the Paris crack growth law, based on the identified crack length, mechanical loading, and critical stress intensity factor,

is highly used because of its simplicity: [33]:

$$\frac{da}{dN} = C(\Delta K)^m \tag{2-8}$$

where a is the fatigue crack length, and thus $\frac{da}{dN}$ is the fatigue crack growth for a load cycle N, C and m are the material constants, and ΔK is the stress intensity range, which is written by:

$$\Delta K = K_{max} - K_{min} \tag{2-9}$$

where K_{max} is the maximum stress intensity factor and K_{min} the minimum.

From the viewpoint of continuum damage mechanics, the damage in materials is a process of accumulation, starting from microcrack initiation and growth to follow. Once it reaches a threshold state, the structural applications contain failures and cannot be serviced anymore.

In the last several decades, the fatigue damage has been evaluated by various models, based on the different experimental methods, and they can be classified as:

- Dynamic response, such as stress and strain [34,35]
- Mechanical property, including hardness, elastic modulus, tensile strength, reduction in area, etc. [36-39].
- Physical property, such as electric, thermal, and magnetic properties. [40-42].

Such methods mentioned above are mainly deduced from the theories of plastic or creep damage. However, there always exists a margin to make them more precise for the brevity of the microscopic defects on the fatigue damage of material. Miner and Palmgren proposed a linear cumulated fatigue damage model named the Palmgren-Miner (P-M) rule [43,44]. It is stated that the fatigue damage being linearly cumulated with respect to various stress levels in the spectrum loadings and the rule can be written as:

$$D = \sum_{i=1}^{k} \frac{n_i}{N_i} \tag{2-10}$$

where n_i and N_i are the number of cycles at a given stress amplitude and the fatigue life at the same stress amplitude from the corresponding S-N curve, respectively. It is noted that fatigue damage D accumulates continuously from a pristine stage with $D = 0$, up to failure occurs and $D = 1$.

The P-M rule is a classic and most used model for estimating the fatigue damage under multi-level loadings. But the quality of the residual lifetime assessment depends on the parameter describing the fatigue life curve, and it has some limitations. For example, the approximation of linear damage accumulation does not allow load sequence effects to be interpreted [45]. It is found that the loading history can affect the fatigue damage leading to nonlinear relations. In such cases, the fatigue damage parameter D can vary to 1.2 or more because of material intrinsic effects being uncovered in the linear accumulation model [46].

Considering damage evolution in terms of micro-cracks of the microstructure of a material can be analyzed by Continuum Damage Mechanics (CDM). It was initially developed by Kachanov [47] and Rabotnov [48] and further investigated by Lemaitre [49] and Chaboche [50]. The general theory of CDM is a function of time, deformation, and stress. In the case of fatigue, the cyclic loading cycles can be used for evaluating the damage and measuring the fatigue life. Then, the evaluation of fatigue damage can be written as [50]:

$$\delta D = f(\dots)\delta N \tag{2-11}$$

where $f(\dots)$ is the function of the variables' state parameters, such as temperature, cyclic hardening, softening, etc., or loading parameters, like stress, strain, or stress-ratio.

It can cause uncertainty in the evaluation of the fatigue damage by using the ratio of N/N_f, since a bit of change of the parameter, the value of the fatigue damage will change a lot. Then, the fatigue damage D can be rewritten by $1-(1-D)^{\beta+1}$ according to [50] for combing the evaluations with the corresponding remaining fatigue lifetime. The model of 1-D damage differential can be used [51]:

$$\frac{dD}{dN} = [1-(1-D)^{\beta+1}]^{\alpha(\sigma_a)} \left[\frac{\sigma_a - \sigma_{l_0}}{M(1-D)}\right]^{\beta} \tag{2-12}$$

where σ_{l_0} is the fatigue limit, M and β are the material parameters. Solving Eq. (2-12), the fatigue life can be written as:

$$N_f = \frac{1}{(\beta+1)[1-\alpha(\sigma_a)]}\left(\frac{\sigma_a-\sigma_{l_0}}{M}\right)^{-\beta} \tag{2-13}$$

Using the ratio of n_i/N_f, the fatigue damage can be rewritten as:

$$D = 1 - \left[1 - \left(\frac{n_i}{N_f}\right)^{\frac{1}{1-\alpha}}\right]^{\frac{1}{\beta+1}} \tag{2-14}$$

where $\alpha(\sigma_a) = 1 - a\langle\frac{\sigma_a-\sigma_{l_0}}{\sigma_u-\sigma_a}\rangle$, and σ_u is the static fracture strength.

2.4 Infrared thermography

2.4.1 Introduction of the infrared thermography

Fatigue tests are an essential foundation for establishing and developing fatigue theories and fatigue parameters such as the fatigue limit and the fatigue life curve of the material. However, the traditional way of determining an S-N curve is laborious and costly. In recent years NDT techniques have been used in fatigue research, such as for predicting the fatigue limit and fatigue life of materials, evaluating structural integrity, and preventing fatigue failure [52,53]. Universal NDT techniques mainly include eddy current inspection, ultrasonic testing, radiography, magnetic particle testing, acoustic emission testing, and others. Infrared thermography, an emerging NDT technique, has also been widely used in engineering and has begun to become a relevant method in fatigue research. Infrared thermography has the characteristics of high speed, high sensitivity, full-field, and more. It allows the change in temperature of the loaded component in operando to be obtained, which can be related to the evolution of fatigue damage. Therefore, the evaluation of fatigue properties based on thermal response has been a very promising research directions in metal fatigue. Thus, temperature measurement based on infrared thermography plays a critical role in the research being discussed in this dissertation.

Since 1992, the International Conference on Quantitative InfRared Thermography

(QIRT) held every two years (the recent one was in Porto, Portugal 2020) has attracted an increasing number of scientists from all over the world. They have promoted the development of infrared thermography technology in the field of fatigue and stress evaluation. With the development of the infrared camera, the researchers not only take the application of infrared thermography technology in the field of NDT into consideration, but also pay more attention to the study of the heat of materials and components in the process of fatigue failure, especially in the energy dissipation and storage. From then on, a variety of fatigue damage models and failure criteria have been proposed to evaluate the fatigue response of materials and components, which can monitor its degradation degree in situ [7]. Correspondingly, the probability of catastrophic accidents can be reduced.

The fatigue failure results from the accumulation of local fatigue damage, can be considered as a process of energy dissipation [54]. The mechanical energy during the fatigue process will transform into energy dissipation, energy storage, elastoplastic strain energy, anelastic internal friction, and other energy forms. Most of the energy is released in the form of heat, mainly about 90% [55]. The related macroscopic performance is the non-uniform temperature change on the surface of the material or component. Such fatigue damage is very closely associated with the evolution of its internal microstructure. What is more is that both the Bauschinger effect and the hysteresis phenomenon have proven that the evolution of fatigue damage is a non-equilibrium thermodynamic process with energy dissipation [15]. Thus, the close relationship between this energy dissipation and the internal crystal microstructure movement of the material has inspired people to investigate the initiation and accumulation of fatigue damage based on the energy storage and dissipation during its failure process [7].

2.4.2 The evolution of thermography

As early in 1830, Weber observed the thermoelastic effect in the experiment [56]. In 1853, Load Kelvin established the theory of thermoelasticity, which is given as [57]:

$$\Delta T = -\frac{\alpha}{\rho C_p} T \Delta \sigma \tag{2-15}$$

where ΔT and T are the change in temperature and measured temperature, respectively, $\Delta\sigma$ the stress range, and α is the thermoelastic coefficient. Strometry observed that the cyclic mechanical loading was accompanied by self-heating [58] in 1914. Twenty years later, Toyler measured the stored energy during a metal's plastic deformation [59]. In 1967, Belgen investigated the thermoelastic effect using non-contact infrared thermal imaging technology [60]. Mountain and Webber developed the system of SPATE (stress pattern analysis by thermal emission) in 1978 [61]. In the last two decades, researchers have carried out many studies on the heat dissipation behavior of materials under fatigue loading by using infrared thermography (IRT), which will be described in detail in the following paragraphs.

IRT is a valuable technique, that is used to monitor the evolution of surface temperature variation of the component or specimen during fatigue or tensile deformation. Luong [62] used IRT to inspect the fatigue-induced damage processes, and it can detect the intrinsic dissipation and give a fast fatigue strength determination. Rosa and Risitano [63] applied IRT for determining the fatigue limit via the analysis of surface temperature. Fargione et al. [64] indicated that the IRT could measure the temperature variation during fatigue testing. It is reported that such a method can give a rapid evaluation of fatigue curves of the material. Plekhov et al. [65] found that the IRT can be used to collect the data of spatial stand deviation of temperature and monitor fatigue crack initiation and crack tip location. Pastor et al. [66] used the IRT to observe temperature oscillations of the 2024-T3 aluminum alloy during HCF testing due to thermoelastic coupling. This research found that a sudden temperature increment occurrs when the transient loading is higher than the yield stress. Morabito [67] found that the IRT can analyze heat sources during a fatigue process. The onset zones of fatigue cracking were associated with high thermoelastic sources. Ummenhofer et al. [68] used the IRT to evaluate the material's localized fatigue damage during fatigue testing.

After a deep investigation into the thermo-mechanical process of material fatigue, researchers realized that the thermodynamic method directly based on temperature lacks a physical background. This seriously hinders the extensive range of application and popularization of such practices in industrial production [69]. As a macroscopic phenomenon of dissipated energy, the temperature is not only determined by the

evolution of fatigue damage, but it is also severely affected by the external environment, such as heat conduction, heat convection, and heat radiation. Thus, using the temperature signals to rebuild the heat sources during fatigue loading and replacing temperature as the damage indicators for fatigue evaluation is an effective method [69].

In the framework of quasistatic thermodynamics under the perturbation hypothesis, Chrysochoos et al. [70] proposed the thermo-mechanical coupling equation in the material fatigue process via its internal variables. The equation divides the heat sources that cause temperature changes into intrinsic dissipation, thermoelastic, internal coupling, and external heat supply. They pointed out that the source of intrinsic dissipation is most closely related to fatigue damage and believed that it could use the intrinsic dissipation as a damage index. Finally, Chrysochoos et al. established a complete set of infrared thermography processing methods by using numerical methods such as local polynomial fitting Laplace transform, which can be used to extract the intrinsic dissipation source. Doudard et al. [71] and Munier et al. [72] performed extensive work on understanding the fatigue damage mechanics, and it resulted in self-heating. Particularly, Munier investigated the difference between the two stress-depended thermal regimes, stress below and above the fatigue limit, in the self-heating response. Khonsari's research term [73,74] introduced the concept of fatigue fracture entropy (FFE) when analyzing the temperature change during the fatigue process. They investigated that the continuous accumulation of the FFE is higher than a threshold value, and that will cause the fatigue failure of the material. This method can also present a quick way of predicting materials and components' fatigue life and damage.

Although the methods mentioned above have achieved specific scientific results, the utilization of temperature signals to rebuild the information of dissipated energy is a complex nonlinear inverse problem. The dissipated energy of materials in the fatigue process is often not very high, especially in the HCF and VHCF regimes. Therefore, it is of great scientific significance and application to build a complete analysis system from the theoretical fatigue mechanism point of view and seek for more efficient and stable calculation methods in view of data processing [69].

Damage in materials under the cyclic loading accumulates and hence progresses continuously until finally rupture appears. This is essentially an irreversible evolution

within the microstructure towards material degradation. For exploring the mechanisms of fatigue damage, it is inevitable explore the evolution of the microstructure of materials. Dissipated energy is a characterization of the irreversibility of the thermodynamic process. It can be used to describe a material's microstructure under cyclic loading in the macroscopic scale. Therefore, utilizing macroscopic dissipated energy to analyze the evolution of a microstructure and reveal the physical mechanism of the fatigue damage is a promising approach within fatigue research. At the same time, it is often necessary to comprehensively use various experimental approaches to achieve a multi-angle observation of a material's fatigue damage process [69].

Maquin et al. [75] measured the dissipated energy of 316L steel and DP600 steel under cyclic loading after different plastic deformations. The results showed that the rate of dissipated energy increased with increasing plastic strain and exhibited a nonlinear relationship. This is because the metallic materials' accumulated plastic strain is very closely related to its internal lattice structure, such as the dislocation movement. Therefore, Maquin et al. thought that the dissipated energy could be used as an indicator to describe the microstructure of materials. Wang et al. [76] combined IRT and digital image correlation (DIC) concurrently and used them to investigate the full-field strain and heat source of the martensite-related Lueders zone in-situ in a tensile test of the Medium Mn steel. IRT has been used for obtaining the field of dissipated energy, and DIC has been used for obtaining the corresponding strain field.

An essential goal of fatigue damage mechanism research is to build a constitutive model. Studying the constitutive relationship from the microscopic mechanism of material deformation allows the nature of material fatigue damage to be understood and to avoid blindly introducing some unnecessary material parameters into the constitutive relationship [69]. The existing formation, distribution, and dynamic characteristics of those defects have a decisive influence on the fatigue properties of the materials. Thus, it is difficult to establish the corresponding macro fatigue damage constitutive relationship from a microstructure structure's movement [69]. Using a meso-model as the bridge and combing the theory of dissipated energy to have a macro-meso-micro analysis is usually a practical research approach. Marcau et al. [77] studied the two mechanical behaviors exhibited by crystalline materials under different stress amplitudes, namely anelastic and inelastic. The movement of the internal

microstructure of material can be characterized by choosing the appropriate internal variables. The evolution of internal variables can then be linked with the dissipated- and stored energy. Doudard et al. [78] thought that the influence of micro-defects on fatigue properties could be characterized by introducing activation sites. The dissipated energy caused by the activation site's plastic work at the mesoscale can be linked with the macroscopic physical quantities. Doudard et al. then proposed a multi-scale probability model that can predict the dispersion with respect to the high-cycle fatigue life. Huang et al. [79,80] further improved the model and applied it to a study related to very high cycle fatigue of titanium alloys.

The above case-based investigations show that the IRT is a valuable tool for monitoring the mechanical degradation of materials. Thus, the IRT can be used to monitor the degradation properties of the materials remotely and avoid sudden catastrophic failures.

2.4.3 Application of IRT in fatigue limit prediction

The manifest evaluation of the material's fatigue somewhat determines the fatigue limit and the S-N curve. There are many methods for determining fatigue parameters in the engineering application, like single-point method, lifting method, group method, strain-controlled fatigue life method, multi-amplitude measurement method, amplification measurement method, etc. In this and the following sections, the fatigue limit and fatigue life evaluation methods will be introduced.

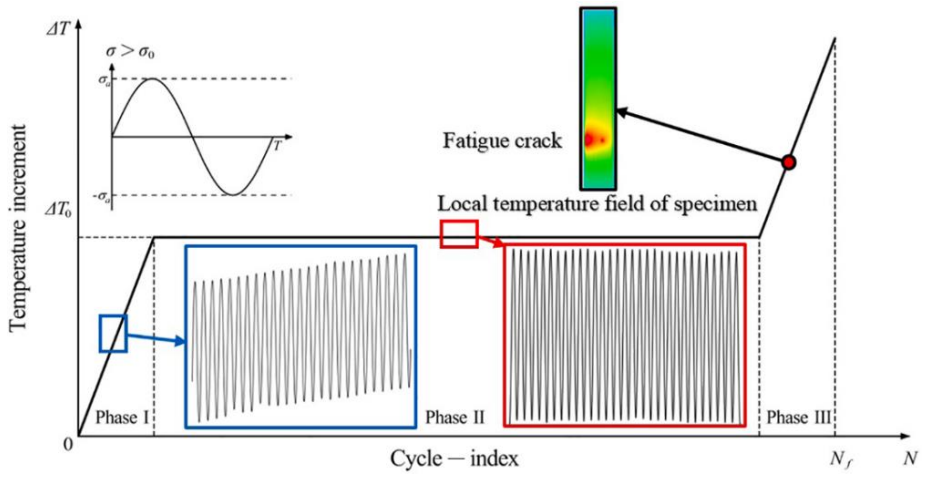

Fig. 2-1. Phases of temperature evolution during metal fatigue experiment [82].

When the loading stress amplitude is higher than the fatigue limit for many metallic materials, the temperature evolution during the fatigue process can be classified into three stages, such as the initial temperature increase phase (phase I), the predominant temperature stabilized phase (phase II), and the drastic temperature increase stage before the fatigue fracture (phase III) [81]. The typical temperature syllogism is shown in Fig. 2-1. Contrarily, when the stress amplitude is below the fatigue limit, it is challenging to observe temperature changes.

- *One-curve method*

As early in 1986, Curti [83] was the first who proposed a high-speed method to predict the fatigue limit of materials by measuring the surface temperature of specimens under cyclic loading. The Ristiano-method [84] was completed by performing a continuous load increase test, and the stabilized temperature (phase II) was then recorded under different stress levels. It takes the stress amplitude σ_a as the abscissa and the temperature increment θ_d^{sta} as the ordinate in the Cartesian coordinates. Fitting

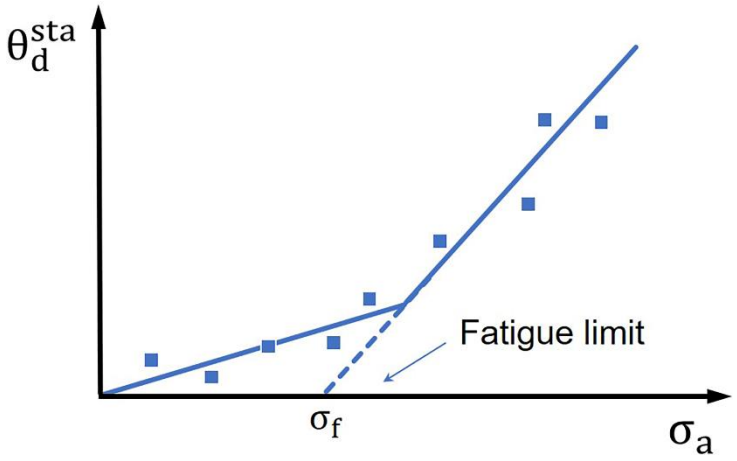

Fig. 2-2. Graphical determination of the fatigue limit by using the one-curve method.

the obtained data in terms of a bi-linear function and determining the intersection of the right-hand straight line and the abscissa of stress, allows the value of the corresponding fatigue limit σ_f to be obtained as shown in Fig. 2-2.

Risitano [84] summarized 23 sets of experimental data obtained by using the Risitano-method over 15 years. The test objects included several materials and components, such as steel, Al-alloy, fiberglass, butt welded joint, and a connecting rod.

Each test result was compared with the result from a traditional (stair-case) fatigue test method. Finally, the error was determined to be within 10%, and the average error was 4.7% only.

- *Two-curve method*

The two-curve method was proposed by Loung [85] in 1995. It is another fast fatigue limit prediction method after the Risitano-method, and it is the most popular in the research work at present. According to previous researchers' research related to cyclic loading, plastic strain, and fatigue damage, Loung investigated the relationship between the dissipated energy, and the fatigue damage of materials and found this to be very close. Thus, fatigue damage can be characterized by the material's intrinsic dissipation rate.

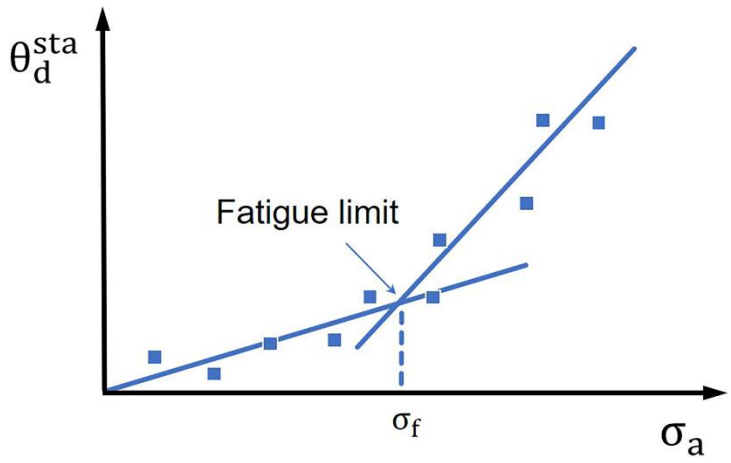

Fig 2-3. Graphical determination of the fatigue limit by using Luong's two-curve method.

When Luong performed experiments on XC55 steel under rotating bending, it was found that even at low-stress amplitudes the surface of the specimen can still have a small temperature increment [85]. Loung defined such a small increment to be caused by the viscoelastic effect of the material due to a theoretical analysis and numerical modeling. This part of the dissipated energy had nothing to do with the fatigue damage. However, such a small temperature increment cannot be ignored for the fatigue limit prediction. Thus, Luong used two straight lines to fit the data of temperature increment and defined the stress amplitude at the intersection of the two fitting lines as the predicted value of fatigue limit, as shown in Fig. 2-3.

- *Normalized angle method*

However, the Luong method has not correctly solved how to separate all the experimental points into two groups. When the stress amplitude is lower than the fatigue limit, the temperature in the stabilized phase does not change much, and the slope of the linear fitting is relatively similar. Oppositely, when the stress amplitude is higher than the fatigue limit, the temperature in the stabilized phase changes significantly. The slope of the straight line fitted by the temperature value will vary greatly, and the slope may change dramatically. The relation of the slope vs. the angle θ formed by the fitted line and the x-axis σ_a is not linear. Then, Jia et al. [86] used the angle change instead of the slope change.

In Huang's method, the normalized angle is used to characterize the angle change θ. Assuming that there are stress levels in the test, these can be named Q_1, Q_2, Q_3, …Q_i.Then the included angle is normalized to:

$$\theta_i^j = \left| \frac{\theta_{i+1} - \theta_i}{\max(\theta_{2,3,4\ldots}) - \min(\theta_{2,3,4\ldots})} \right| \tag{2-16}$$

where the subscript i is the sequence number of the points, θ_i the angle between lines determined by point-set $\{\theta_{i-1}, \theta_i\}$ and σ_a the x-axis, as shown in Fig. 2-4. The term $\max(\theta_{2,3,4\ldots}) - \min(\theta_{2,3,4\ldots})$ used to normalize the angle change and the θ_i^j is the normalized angle change between lines fitted by point-sets $\{P_{i-1}, P_i\}$ and $\{P_i, P_{i+1}\}$ $(i \geq 2)$.

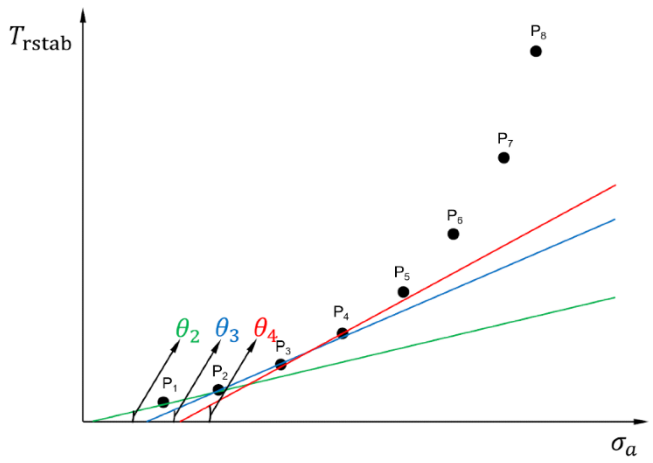

Fig. 2-4. Schematic definition of θ_i [86].

For a set of fatigue tests, the maximum value of θ_i^j can be determined through the normalized calculation of the included angle, which shows that at the i-th stress level, the angle between the two straight lines is the biggest. This point is set as the boundary point of the predicted fatigue limit. The results are divided into two groups according to the dividing point, and the temperature points before and after the dividing point are fitted. The stress value at the intersection point of the two fitting straight lines is the fatigue limit. This method is developed from the Luong method and is named the angle-normalized two-line method.

The previously mentioned three methods are based on the surface temperature of the specimen during cyclic loading and can give a rapid evaluation of the material fatigue limit. This may possibly be achieved with only one specimen to complete a fast prediction of fatigue parameters in one day maximum. The approach has arisen great attention in the academic and engineering field. Meanwhile, the methods for fatigue limit prediction are continuously developed and improved and have been widely used for the fatigue evaluation of different engineering materials and mechanical components.

2.4.4 Application of IRT in fatigue life evaluation

In order to achieve more fatigue evaluation related parameters in a fast way, many researchers have extended the application range of evaluation method by using the temperature data, such as to predict fatigue S-N curves. Since traditional experimental approaches for evaluating material fatigue lifetime are very cost-, specimen-, and time-consuming, alternative approaches have been developed for seeking a fast evaluation of fatigue life. In the last decades, many investigations have proven that in a fatigue loaded specimen three stages of temperature evolution can be observed if the stress amplitude is above the fatigue limit, as aforementioned, and the plasticity can become a factor relevant with respect to lifetime. Here are some approaches to fatigue life evaluation based on the IRT.

2.4.4.1 Macro relationship

- Phase I:

According to the initial slope of the temperature R_θ (as shown in Fig. 2-5) in the phase I as shown in Fig. 2-1, Amiri et al. [87] developed an approach for the evaluation of fatigue life N_f, where they found a relation of $R_\theta - N_f$, such as:

$$N_f = c_1 R_\theta^{c_2} \tag{2-17}$$

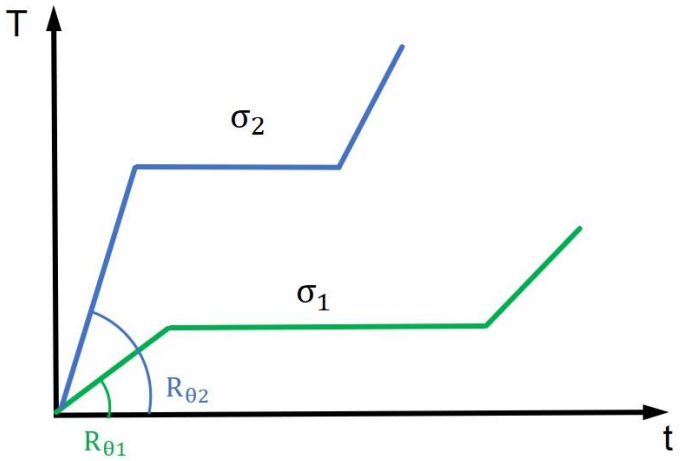

Fig. 2-5. The slop of temperature at the beginning of the test at two stress levels.

where c_1 and c_2 are material constants. What is more, after they performed under different fatigue loadings, they concluded that the experimental fatigue data represented as N_f/c_1 versus R_θ can be consolidated in a universal curve, which is shown in Fig. 2-6. Due to the fact that R_θ can be evaluated at the initial cycles of the fatigue testing, a result can be obtained in a relatively short time. Such a method can therefore provide a very fast prediction of fatigue failure.

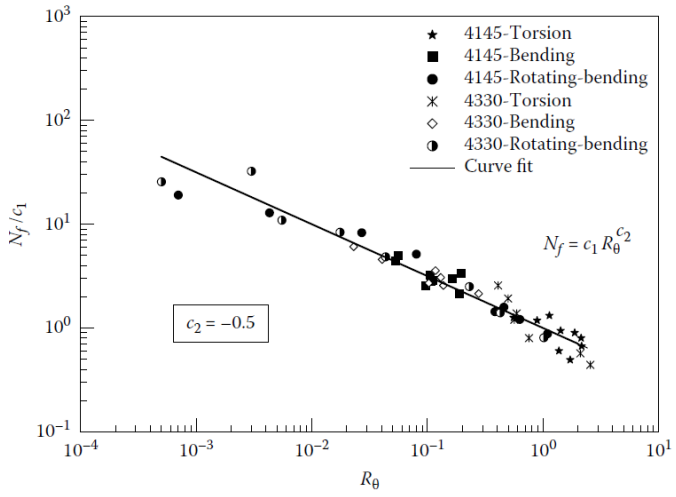

Fig. 2-6. Fatigue life prediction based on initial temperature rise [87].

- Phase II:

Jiang et al. [88] found that the difference between steady-state temperature (T^*) in phase II and ambient temperature (T_0), $\Delta T = T^* - T_0$ (as shown in Fig. 2-7), has a relation to the fatigue life N_f under axial fatigue loading:

$$(N_f)^m = C \cdot \Delta T \tag{2-18}$$

where m and C represent material constants. It is suggested that the temperature during the steady-state condition (phase II) could be utilized as an index for warning fatigue failure by using Eq. (2-18).

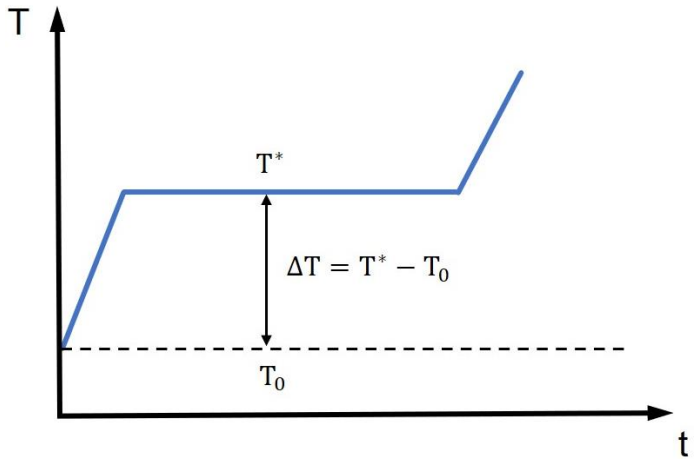

Fig. 2-7. Steady-state temperature rise in the second phase.

- Phase III:

Huang et al. [89] investigated the temperature rise rate very close to the end of a fatigue test of a high ductility material and found the sharp increase in temperature to be associated with the initiation and propagation of macro fatigue cracks and imminent fracture. Such a temperature rate R_γ (as shown in Fig. 2-8) after the steady-state is associated with the fatigue life N_f via:

$$R_\gamma = \frac{\Delta T}{\Delta t} = C' \cdot \exp\left(\frac{G}{(N_f)^{1/b}}\right) \tag{2-19}$$

where C', G, and b are material constants. The temperature in phase III can be used as an index of the warning of material failure and could help to prevent catastrophic failure.

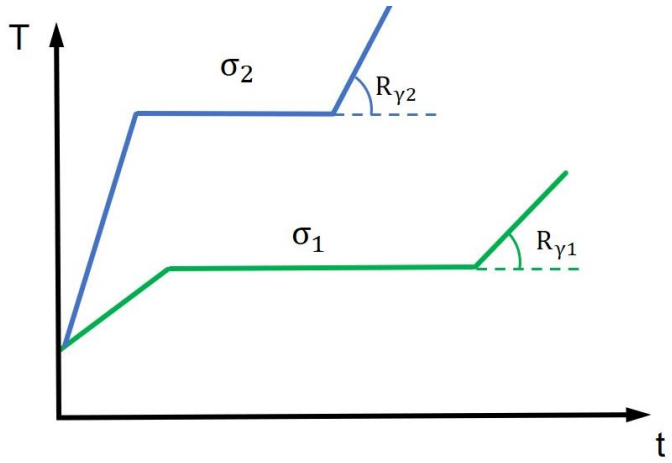

Fig. 2-8. Slope of the temperature rise in the third phase at two stress levels.

- Total area

Fargione et al. [64] proposed the concept of material's total dissipated energy for fatigue failure. As shown in Fig. 2-9, this method is based on the total dissipation value, which can be replaced by an integral value of the surface temperature increment over the entire fatigue life, and it is integrated as ϕ:

$$\phi = \int_0^{N_f} \Delta T \, dN \tag{2-20}$$

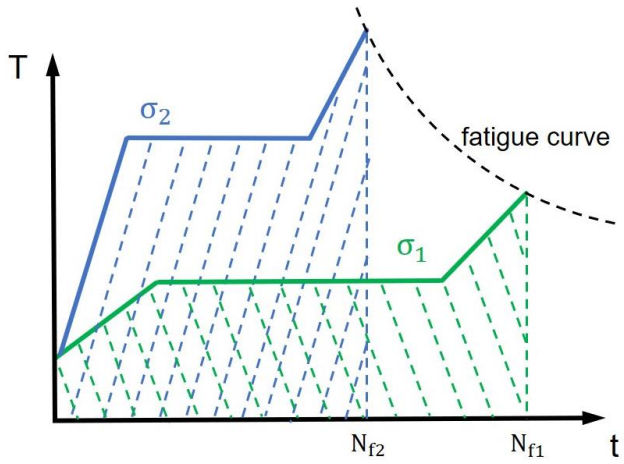

Fig. 2-9. Area under a temperature profile at two stress levels.

Fargione found this area to be a material constant regardless of the stress amplitude. Finally, using the calculated integral value, divided by the stabilized temperature, allows fatigue life under different stress amplitudes to be obtained.

2.4.4.2 Intrinsic dissipation

Based on the first and second laws of thermodynamics, a specific kind of heat diffusion was deduced by Boulanger et al. [90] to determine the heat source from the measured temperature fields of the specimen's surface during fatigue testing:

$$\rho C_p \dot{\theta} - \mathrm{div}(k: \mathrm{grad}\theta) = S_{the} + S_i + d_1 + r_{ext} \tag{2-21}$$

where ρ, C_p, and k are the mass density, specific heat capacity, and thermal conductivity, respectively. $\theta = T - T_0$ the change in temperature (T is the measured temperature and T_0 the equilibrium temperature). S_{the} is the thermoelastic source term, S_i the internal coupling source term, d_1 the intrinsic dissipation term, and r_{ext} the external heat source term. Since the thermal process during the fatigue test is considered as a pure dissipation mechanism, the internal coupling source S_i under the given boundary condition can then be neglected [91]. The external heat source r_{ext} is the heat loss. It is strongly dependent on the boundary condition of the test setup and is supposed to be the following simple time-independent and linear-solution: $r_{ext} = \rho C_p \frac{\theta}{\tau_{eq}}$. The thermoelastic source S_{the} vanishes in each loading cycle in the end, and the temperature variation tends to be asymptotic towards: $\frac{\partial \theta}{\partial t} = 0$. Finally, the dissipated energy per unit of time can be simplified as:

$$d_1 = \rho C_p \frac{\theta}{\tau_{eq}} \tag{2-22}$$

where τ_{eq} is a time constant characterizing the heat exchanges between the specimen surface and the environment.

- Uniaxial fatigue

Since the dissipated energy can be regarded as a fatigue index, Wang et al. [92] calculated the total cumulated energy dissipation $d_{1,cum}$, namely, the energy tolerance E_c to failure during a fatigue test to be:

$$E_c = d_{1,cum} = \int_0^{N_f} \frac{d_1}{f} dN \tag{2-23}$$

Since phase II occupies the main portion of the fatigue lifespan, the fatigue lifetime N_f can be assumed to be the span of phase II, and then energy tolerance to failure can

be calculated by:

$$E_c = \int_0^{N_f} \frac{d_1}{f} dN = \frac{\rho C}{f\tau} \theta N_f \tag{2-24}$$

Thus, the fatigue lifetime N_f is:

$$N_f = \frac{f\tau E_c}{\rho C \theta} \tag{2-25}$$

Some extensive studies showed that there exists a relation of θ and σ_a:

$$\theta = K_T \sigma_a^2 - m \qquad \text{when } \sigma_c \leq \sigma_a \leq \sigma_y \tag{2-26}$$

where σ_c and σ_y are the critical stress for the generation of dissipation and yield stress, respectively. Then, Then, Eq. (2-25) can be written as:

$$N_f = \frac{f\tau E_c}{\rho C (K_T \sigma_a^2 - m)} \tag{2-27}$$

However, phase II is not horizontal for some materials, as schematically shown in Fig. 2-10, e.g., the temperature evolution in the phase II of the commercially pure copper at a fatigue loading frequency of 20 kHz with a stress ratio of R = -1. Based on this problem, Wang et al. [92] considered the relevant incremental temperature variation rate and modified the fatigue life evaluation from intrinsic dissipation. In the first step, the energy tolerance E_c is modified as:

$$E_c = d_{1,cum} = \int_0^{N_f} \frac{\rho C}{f} \left(\frac{\partial \theta}{\partial N} + \frac{\theta}{\tau}\right) dN \tag{2-28}$$

Through a series of calculations, the fatigue lifetime N_f is finally given as:

$$N_f = \frac{1}{P} \sqrt{2PE_c + q^2} - q \tag{2-29}$$

where $p = \frac{\rho C \lambda}{f\tau}$, $q = \frac{\rho C}{f\tau}(\lambda\tau + \theta)$ and $\lambda = \frac{\theta_\Delta}{N}$.

Two fatigue methods, Eqs. (2-27) and (2-29), were proposed for fatigue life evaluation. The first one was attracted due to its simplicity, and the second considered the possible damage evolution during the fatigue test. It can be extended to materials with a temperature decrease in phase II, e.g., AZ31B magnesium alloy [93,94].

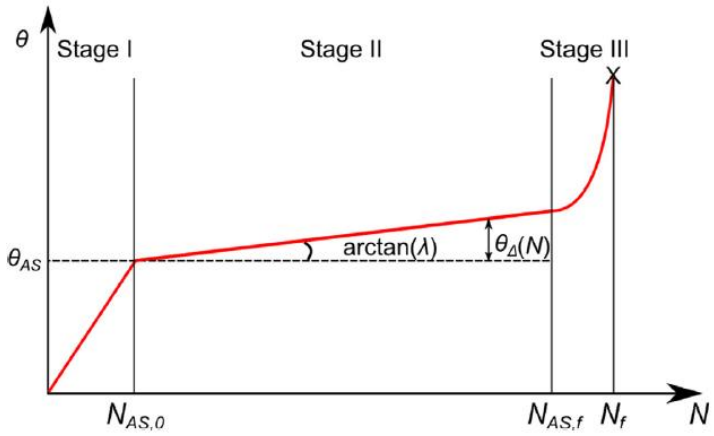

Fig. 2-10. Schematic presentation of the change in temperature during fatigue test under the assumption of linear temperature evolution in phase II [92].

- Multiaxial fatigue model

Taking the intrinsic dissipation as the damage index, Feng et al. [95] further developed a multiaxial fatigue model based on the viewpoint of dissipation energy. Five different loading paths applied in the fatigue tests for the 316L stainless steel are shown in Fig. 2-11. The results show that the energy tolerance E_c can be different for different tests. In that case, it can be indicated that the parameter E_c is a path-independent parameter in multiaxial fatigue. The authors regarded the tension-compression and torsion as the two basic loading models and proposed a factor K to express the relation between energy tolerance under the symmetric tension-compression ($E_{c,A}$) and under the pure torsion ($E_{c,T}$), where $K = E_{c,T}/E_{c,A}$.

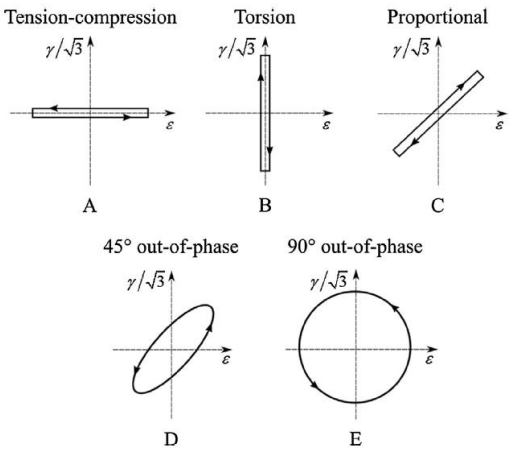

Fig. 2-11. Five different loading paths applied in fatigue tests [95].

In order to evaluate the energy tolerance under proportional loading, the strain-ratio-dependent parameter ξ was introduced to correlate $E_{c,P}$ with $E_{c,T}$ and $E_{c,A}$, which is given as:

$$E_{c,P} = [1 + \xi(K - 1)] \cdot E_{c,A} \tag{2-30}$$

Then, another factor K_P was given to bridge the two energy tolerances by

$$K_P = \frac{E_{c,P}}{E_{c,A}} = 1 + \xi(K - 1) \tag{2-31}$$

Thus, the fatigue life for the proportional loading can be calculated by

$$N_f = \frac{E_{c,P}}{d_1} = \frac{K_P \cdot E_{c,A}}{d_1} \tag{2-32}$$

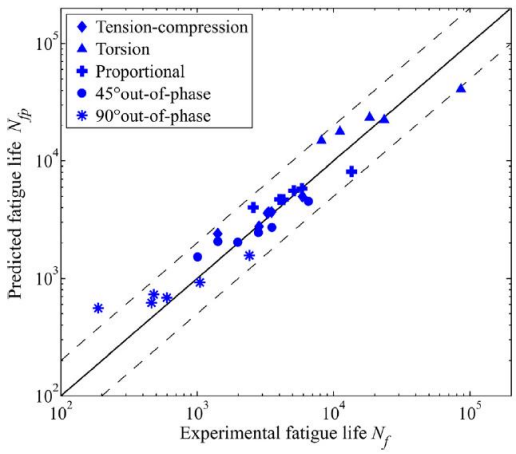

Fig. 2-12. Comparison of the predicted fatigue life with the experimental fatigue life for the applied fatigue tests [95].

For calculating the energy tolerance under the non-proportional loading $E_{c,NP}$, a factor F_{NP} was introduced to relate with $E_{c,P}$ by $F_{NP} = E_{c,P}/E_{c,NP}$, where F_{NP} can be calculated by:

$$F_{NP} = 1 + m \cdot f_{NP}^{n} \tag{2-33}$$

and where m and n are the material constants. The parameter $E_{c,NP}$ can then be rewritten as:

$$E_{c,NP} = \frac{E_{c,P}}{F_{NP}} = \frac{K_P \cdot E_{c,A}}{F_{NP}} \tag{2-34}$$

Finally, the fatigue life for the non-proportional loading can be calculated by

$$N_f = \frac{E_{c,NP}}{d_1} = \frac{K_P \cdot E_{c,A}}{F_{NP} \cdot d_1} \tag{2-35}$$

The final fatigue life evaluated by the proposed model was satisfied to meet the experimental data as shown in Fig. 2-12.

- Meneghetti-method

Meneghetti [96] proposed a fatigue life calculation method by measuring the temperature cooling rate, dT/dt (as shown in Fig. 2-13), after an interruption of phase II, where the steady-state temperature of a fatigue test is reached. The cooling rate is related to the specific heat energy Q by:

$$Q = -\frac{\rho c}{f} \cdot \left.\frac{dT}{dt}\right|_{t=t^*} \tag{2-36}$$

where ρ is the density, c the specific heat capacity, and f the load frequency. The fatigue life N_f is related to the specific heat energy in this study as

$$N_f = C \cdot Q^m \tag{2-37}$$

where C and m are material constants. This method can also quickly evaluate the S-N curve by estimating the energy converted into heat during a fatigue test.

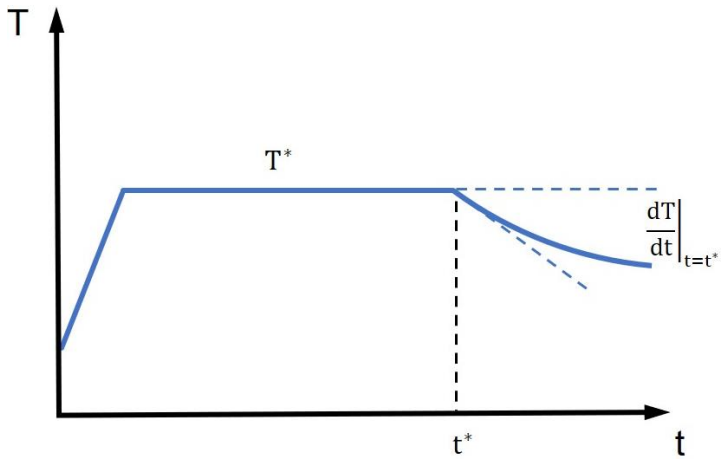

Fig. 2-13. The slope of the cooling rate after stopping a fatigue test.

2.4.4.4 Own methods proposed

In order to provide the S-N dataset in a small number of fatigue tests, some short-term evaluation procedures (STEPs), Stress-based fatigue life evaluation (StressLife), Strain-based fatigue life evaluation (StrainLife), and Step-Bar Fatigue Life approach (SteBLife) are developed at Chair of Non-Destructive Testing and Quality Assurance (LZfPQ) at Saarland University, which are based on the conventional-, e.g., strain, and non-destructive-, e.g., temperature, electrical resistance, methods. The STEPs have been well validated by different materials and the S-N data evaluated on such methods are competitive to conventionally determined S-N data.

- StressLife

The StressLife method [97] provides the possibility for evaluating an S-N curve based on a combination of Morrow [98], Manson- Coffin [26, 27], and Basquin [99] laws all merged into a set of equations. The schematic workflow for the StressLife evaluation method is shown in Fig. 2-14. The material response (M, e.g., change in temperature, change in electrical resistance, or magnetic-based measurements) data using NDT-based methods from LITs and CATs are utilized to derive a parameter related to fatigue for a fatigue life evaluation. The first step of this StressLife approach is to divide the σ_a-M relationship (Fig. 2-14b) from a LIT (Fig. 2-14a) into its mostly elastic and mostly plastic range independently, according to the modified Morrow law

$$\sigma_a = K_{e/p/CAT'} \times (M)^{n_{e/p/CAT'}} \tag{2-38}$$

where $n_{e/p'}$ is the cyclic hardening exponent (e: mostly elastic range, p: mostly plastic range). Then, the fatigue strength exponent b from the mostly elastic range and the fatigue ductility exponent c from the mostly plastic range can be determined by:

$$b = \frac{-n_{e'}}{5n_{e'}+1} \tag{2-39}$$

$$c = \frac{-1}{5n_{p'}+1} \tag{2-40}$$

The material response M during the fatigue test is the sum of an elastic and plastic portion: $M = M_e + M_p$. M_e can be described by the Basquin equation: $M_e = B \times (2N_f)^b$, where B is expressed through $\sigma_f' \times E^{-1}$ (σ_f' = fatigue strength coefficient,

E = Young's modulus); M_p can be represented by Manson-Coffin: $M_p = C \times (2N_f)^c$, where C corresponds to the fatigue ductility coefficient ε_f'. At a defined fatigue stage, e.g., 50% N_f, one obtains:

$$M_{1/2} = M_e = B \times \left(2N_{f,1/2}\right)^b + M_p = C \times \left(2N_{f,1/2}\right)^c \tag{2-41}$$

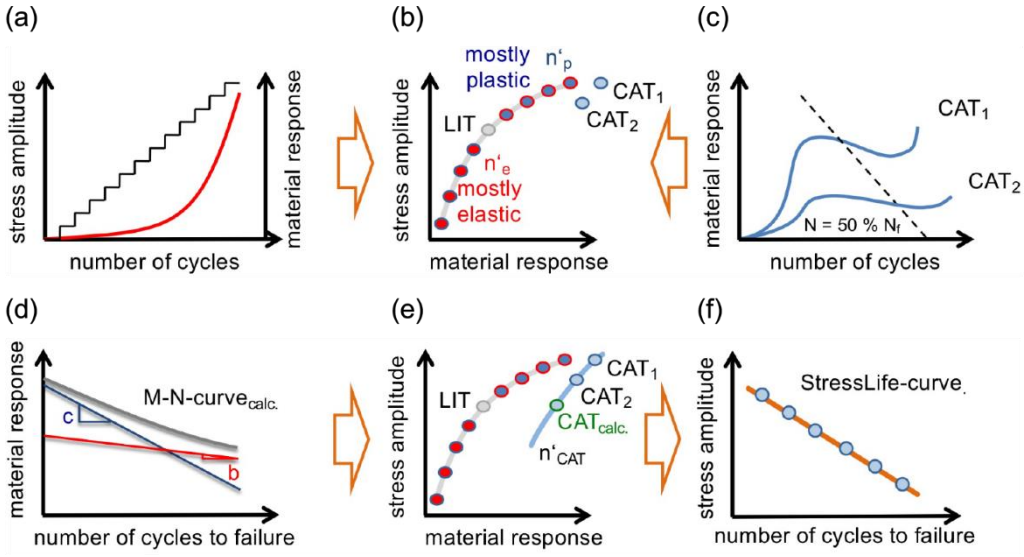

Fig. 2-14. Schematic workflow for the method StressLife [97].

Fig. 2-14c shows two CATs, which lead to different lifetimes and different values of the material response. Taking cyclic stress σ_1 and σ_2 into Eq. (2-41), one obtains:

$$B = \frac{M_1 - C \times \left(2N_{f,1}\right)^c}{\left(2N_{f,1}\right)^b} \tag{2-42}$$

$$C = \frac{\left(2N_{f,1}\right)^b \times M_2 - \left(2N_{f,1}\right)^b \times M_1}{\left(2N_{f,1}\right)^b \times \left(2N_{f,1}\right)^b - \left(2N_{f,1}\right)^b \times \left(2N_{f,1}\right)^b} \tag{2-43}$$

Using parameters b and B in M_e and c and C in M_p, the elastic and plastic portion of the material response can be plotted over lifetime as shown in Fig. 2-14d. Thus, the sum of both curves leads to the material response-lifetime curve. Based on the Ramberg-Osgood [100,101] relationship, the elastic behavior is assumed to be linear. Extrapolate the elastic portions of the material response of σ_1 and σ_2 to a σ_a-value ($CAT_{calc.}$) above the transition-point from the mostly elastic to the mixed elastic-plastic behavior, then the parameter $M_{e.}$ can be calculated for σ_a of $CAT_{calc.}$. Using the relation of M_e (slope b in Fig. 2-14d) vs. M-N curve, the M for a $CAT_{calc.}$ can be determined (Fig. 2-

14e). After the calculation of the third point, $K_{CAT'}$ and $n_{CAT'}$ can be solved according to Eq. (2-38).

Taking Eq. (2-41) into Eq. (2-38), one obtains:

$$\sigma_a = K_{CAT'} \times \left(B \times (2N_f)^b + C \times (2N_f)^c\right)^{n_{CAT'}} \quad (2\text{-}44)$$

By using the coefficients $K_{CAT'}$, B, C and the exponents $n_{CAT'}$, b, c, the S-N curve can be drawn finally as shown in Fig. 2-14f.

- StrainLife

The StrainLife method [102] is based on the same principles as StressLife mentioned before, and it is modified to meet the requirements of strain-controlled fatigue tests. A strain increase test (SIT) is carried out, and the relation of its material response M vs. the total strain amplitude $\varepsilon_{a,t}$ is given as shown in Figs. 2-15a and 2-15b, respectively.

Fig. 2-15c shows the total strain amplitude levels for two strain-controlled CATs. The M-$\varepsilon_{a,t}$ relationship is extracted at 50 % N_f from the two CATs and also plotted ins Fig. 2-15b and together with the M-$\varepsilon_{a,t}$ from the SIT. In what follows, the M-$\varepsilon_{a,t}$ data from the SIT are transferred via utilizing the M-$\varepsilon_{a,t}$ data from CATs, and which can provide a full M-$\varepsilon_{a,t}$ dataset for CAT, which is being described in Eq. (2-45) for the mostly elastic and mostly plastic range. Then, the effects due to pre-damage and cyclic hardening can be neglected:

$$M = K_{e/p/CAT'} \times (\varepsilon_{a,t})^{n_{e/p/CAT'}} \quad (2\text{-}45)$$

where the total strain amplitude is the addition of elastic strain amplitude $\varepsilon_{a,e}$ and plastic strain amplitude: $\varepsilon_{a,t} = \varepsilon_{a,e} + \varepsilon_{a,p}$. $\varepsilon_{a,e}$ can be described by Basquin law: $\varepsilon_{a,e} = B \times (2N_f)^b$, where B is expressed through $\sigma_f' \times E^{-1}$; $\varepsilon_{a,p}$ can be represented by Manson-Coffin: $\varepsilon_{a,p} = C \times (2N_f)^c$, and C corresponds to the fatigue ductility coefficient ε_f'. As the $n_{e/p/CAT'}$ can be derived from Eq. (2-45) and the exponents b and c can be calculated by the above equations; then, at a defined fatigue stage, e.g., 50% N_f, we can get

$$\varepsilon_{a,t,1/2} = B \times \left(2N_{f,1/2}\right)^{b} + C \times \left(2N_{f,1/2}\right)^{c} \quad (2\text{-}46)$$

The parameters B and C can be evaluated from Eqs. (2-42) and (2-43), and $M_{1/2}$ can be substituted by $\varepsilon_{a,t,1/2}$, Finally, the total strain vs. lifetime curve can be drawn as shown in Fig. 2-15d.

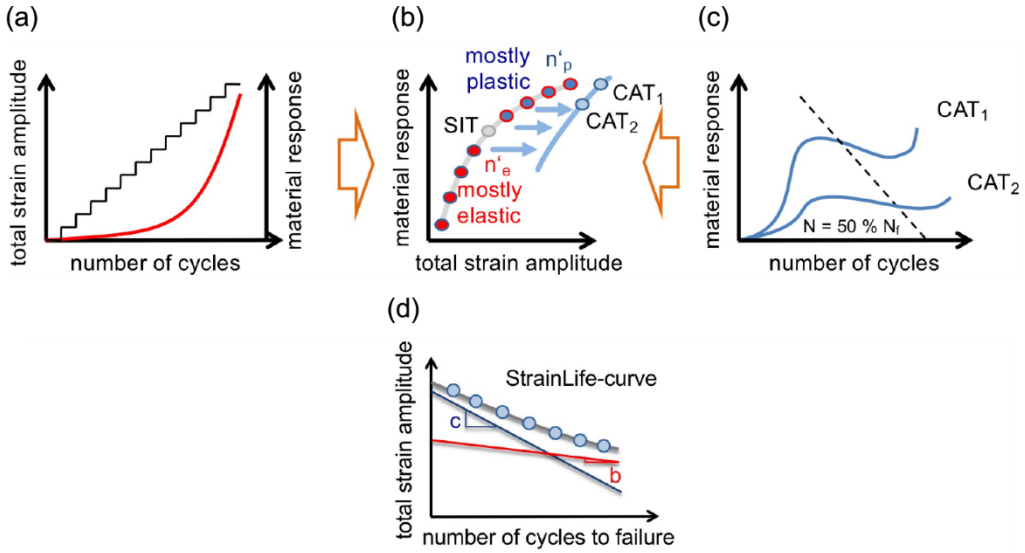

Fig. 2-15. Schematic workflow for the method StrainLife [103].

- SteBLife

The geometry of the specimen used for the SteBLife approach [104-106] is a stepped shape with different gauge length diameters, which results in different σ_a values during the fatigue test under constant amplitude loading. The schematic specimen shape is shown in Fig. 2-16. The material response (M) is measured by NDT methods like before, e.g., change in temperature. The relationships between load applied and materials response M under cyclic loading for the five sections of the specimen are obtained, where two are similar due to the symmetry of the specimen, this provides a database for the relation of σ_a-M. In what follows, the generalized Morrow and Basquin laws are combined to determine the fatigue life for the investigated material. In this approach, three different SteBLife modules were proposed, including $SteBLife_{stc}$ (stc: single test, trend curve), $SteBLife_{mtc}$ (mtc: multiple test, trend curve), and $SteBLife_{msb}$ (msb: multiple tests, scatter bands).

SteBLife$_{stc}$ allows a trend S-N curve with only one single test within 2-3 hours to be determined, and such a procedure is schematically provided in Fig. 2-16. SteBLife$_{mtc}$ is based on 2-5 SteBLife tests under different stress amplitudes, that allows statistics of the fatigue dataset to be improved and an S-N curve with a 50% failure/survival probability to be generated. SteBLife$_{msb}$ is based on 4-5 SteBLife tests performed at the same stress amplitude, and the received lifetimes are transferred into the Gaussian distribution to obtain the possibility to determine scatter bands for different failure probabilities, e.g., 5, 50, and 95%.

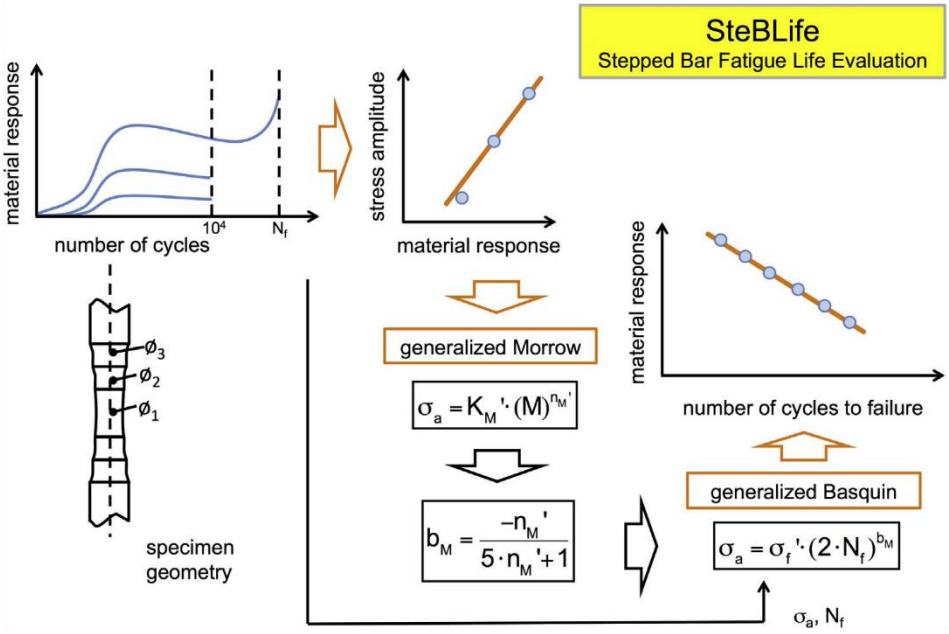

Fig. 2-16. Schematic workflow for the fatigue life calculation method SteBLife$_{stc}$ [104].

2.5 Magnetic Barkhausen noise

The Barkhausen noise is the magnetization of ferromagnetic materials from a demagnetized state to its magnetic saturation by applying a magnetic field. In the intermediate stage, the ferromagnetic materials are magnetized through the process of the sudden growth of magnetic domains and irreversible and discontinuous displacement. This movement of magnetic domains is called the Barkhausen effect, which was first discovered by the German physicist Barkhausen in 1919 [107]. During the magnetization process, the internal magnetic domains rotate, and the movement of the magnetic domain walls at 90° and 180° are discontinuous. The change of magnetization M of the material with the external magnetic field is stepped increase as

shown in Fig. 2-17. In the alternating magnetic field, the magnetic domain walls rendering the magnetic domains will repeatedly move, generating many magnetic Barkhausen noise (MBN) signals [108].

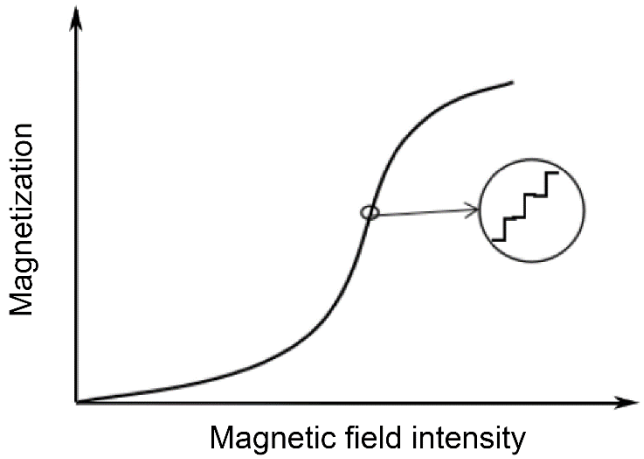

Fig. 2-17. Schematic of magnetization curve of a ferromagnetic material indicating the region of Barkhausen noise.

The MBN signal is very closely related to the microstructure and internal stress conditions of the material. By analyzing the signal, it can reflect the early mechanical degradation of materials, e.g., changes in microstructure, the state of stress, and micro-damage of the material. Some applications of the MBN technique are given as follows:

- Material stress detection: e.g., Amiri et al. [109] pointed out that stress anisotropy and crystal anisotropy play a decisive role in the magnetization of materials. In the direction of the easy magnetization axis of ferromagnetic materials, the influence of stress on the MBN signal is greater than in other directions. It is verified by the magnetostriction and magnetization curves.

- Material hardness testing: e.g., Moorthy et al. [110] heated En36 steel to different temperatures (19~900 ℃) and got this characterized through an MBN detection test. The results showed that the MBN signal of En36 steel is very sensitive to a change in temperature. The higher the material temperature, the smaller the surface hardness, and the bigger the measured MBN signal amplitude.

- Material surface-treatment process evaluation: e.g., Altpeter et al. [111] used MBN to detect the residual stress of different heat-treated alloys. Work was focused on comparing the difference between the MBN signal when the residual stress at room

temperature (20 °C) and Curie temperature (230 °C) tends to be saturated.

- Fatigue status detection: e.g., Moorthy et al. [112] studied En36 steel under cyclic loading of overstressing with the characterization of MBN and pointed out, that the cyclic load under high stress will increase the dislocation density of the material when compared to the uniaxial load, and which reduced the value of MBN signal peak.

3. Materials and Methods

3.1 Materials

Within the framework of this dissertation, the primary model material investigated here is the normalized SAE1045 steel (Germany designation: C45E), an unalloyed medium steel that is widely used for engineering applications. According to the material manufacturer, the chemical composition is given in Table 3-1, which follows DIN EN 10083-1standard. The material consists of a mostly ferritic-pearlitic microstructure which is shown in Fig. 3-1. The mechanical and thermophysical properties are listed in Table 3-2.

Table 3-1

Chemical compositions of normalized SAE 1045.

(Wt.-%)		C	Si	Mn	P	S	Cr	Mo	Ni
DIN	min.	0.42	-	0.50	-	-	-	-	-
	max.	0.50	0.40	0.80	0.030	0.035	0.40	0.10	0.40
Customer's report		0.47	0.23	0.72	0.012	0.013	0.06	0.014	0.07

Table 3-2

Material properties of normalized SAE 1045.

Property	Unit	Value	Property	Unit	Value
Ultimate strength	MPa	710	Mass density	kg m^{-3}	7821
Yield strength	MPa	413	Specific heat capacity	J kg^{-1} K^{-1}	474
Poisson's ratio	—	0.3	Heat conduction coefficient	W m^{-1} K^{-1}	48
Young's modulus	GPa	214	Linear thermal expansion coefficient	10^{-6} K^{-1}	11
Brinell hardness	HB	210			

Thermophysical parameters taken from the Ref [113].

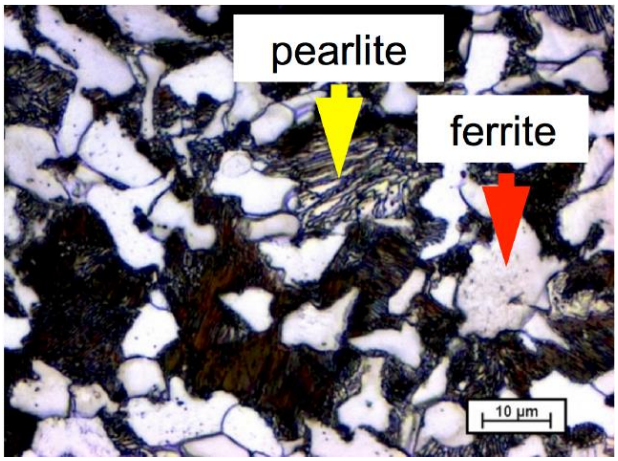

Fig. 3-1. Microstructure of normalized SAE1045 (C45E) steel.

For quasistatic tensile testing, an ultrafine-grained medium (UFG) Mn TRIP steel with a chemical composition of Fe-7Mn-0.14C-0.2Si (in wt.%) was tested as a case study. The steel was cold-rolled and followed by an annealing procedure, in which the material was heated at a rate of 5 °C/s until 620±15 °C was reached and kept for 24 h in a nitrogen atmosphere protection. After that, the steel was cooled in air to room temperature, leading to two dominant phase contents: ferrite and retained austenite. The grain size of the annealed material is ~360 nm, and the overall γ-austenite has ~34.7% volume fraction. The inverse pole figure map and the phase map of the material have been observed by EBSD, where the results are shown in Fig. 3-2. The mechanical properties of this material are listed in Table 3-3.

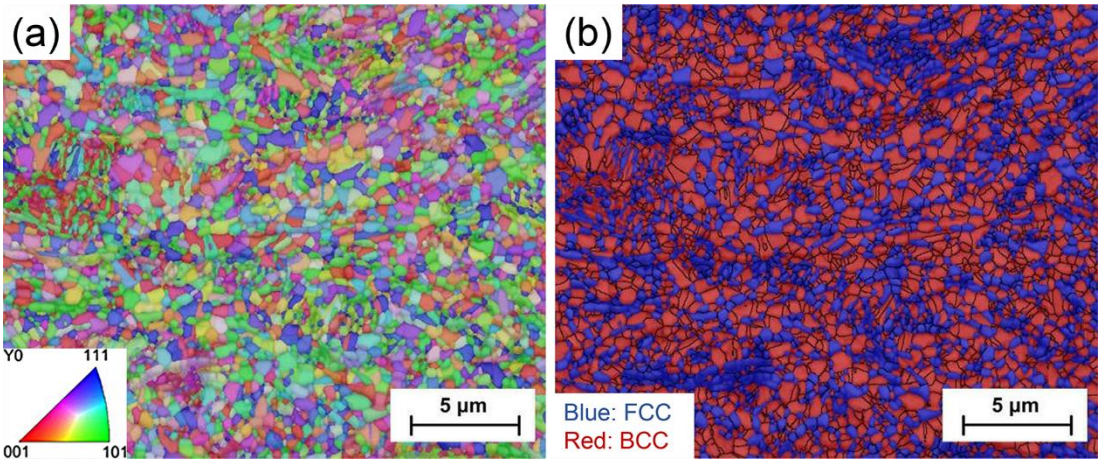

Fig. 3-2. Crystallographic characteristics of the medium Mn TRIP steel: (a) EBSD inverse pole figure map; (b) EBSD phase map (blue: ferrite; red: austenite).

Table 3-2

Material properties of the investigated medium Mn steel.

Upper yield strength (MPa)	Lower yield strength (MPa)	Ultimate strength (MPa)	Elongation
1060	985	1020	28%

3.2 Mechanical testing

3.2.1 Fatigue testing

The fatigue tests, including load increase tests (LITs) and constant amplitude tests (CATs) as shown in Fig. 3-3, were carried out on a Shimadzu type RHF-L servo-hydraulic testing machine with a 21 kN cyclic load capacity for the SAE1045 steel. The schematic diagram of the experimental set-up is shown in Fig. 3-4. The fatigue system was set up to a maximum number of 2×10^6 cycles or stopped when the specimen failed. The fatigue tests were run under load control mode with a stress ratio of R = -1 and a load frequency of 5 Hz.

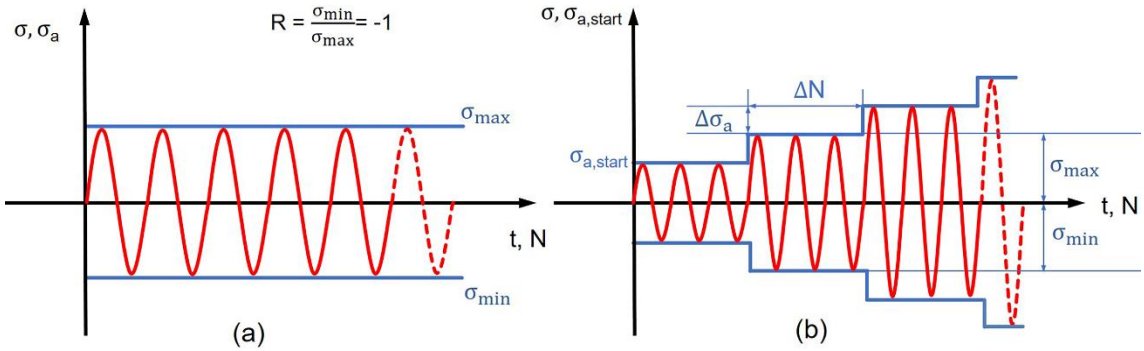

Fig. 3-3. Schematic diagram of (a) CAT and (b) LIT procedure.

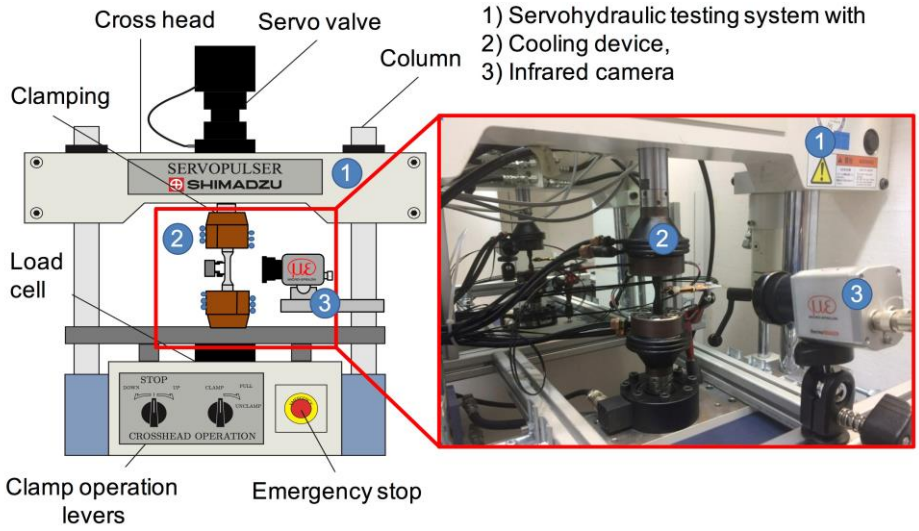

Fig. 3-4. Experimental setup of servohydraulic fatigue testing machine.

3.2.2 Quasistatic tensile testing

In this investigation, a standard dog-bone-shaped specimen with a gauge dimension of 35×6×1.4 mm^3 was designed and machined along the rolling direction from the as-received medium Mn TRIP steel plate. The whole specimens' surfaces were polished to a mirror-like finish before uniaxial tensile tests were performed. The tests were carried out with a universal tester (SHIMADZU AGS-X, 10 kN) and performed at a cross-head constant speed of 1 mm/min at room temperature.

3.3 NDT-methods

3.3.1 Temperature measurement

For temperature measurements, an infrared camera (Micro-Epsilon ThermoIMAGER type TIM450 with a spectral range between 7.5 and 13 µm, an optical resolution of 382×288 pixels, and thermal sensitivity of 0.04 K), was used during the fatigue tests. The surface temperature was recorded as a result of the average temperature of a defined area (10×10 pixels) in the middle part of the gauge length of the surface of the specimen.

3.3.2 Magnetic Barkhausen noise

The magnetic Barkhausen noise (MBN) measurements were carried out by using a µmagnetic measurement system of QASS. The sinusoidal magnetic signal was excited

at a frequency of 10 Hz with a coil voltage amplitude of 955 mV. Each excitation lasted 500 ms (5 cycles). The applied sensor was positioned with a minimal lift-off of ~0.3 mm perpendicularly to the surface of the specimen. The raw signal was processed by selecting a region of interest within the frequency of 120 Hz -500 Hz, while denoising of the signal was made in both frequency and time domain. To avoid phase shift, only envelope curves were extracted rather than using a smoothing algorithm. The MBN signal peaks (unitless) and their positions (in mV regarding the coil voltage) were determined and used to characterize the microstructural changes on the specimens. The peak positions are considered to be correlated with coercivity.

3.3.3 Digital image correlation

The surface of the specimen was speckled patterned with white and black paints to obtain a better contrast for the DIC measurement. To evaluate the strain distribution, optical photos of such prepared sample surface were taken at a framerate of 1 fps during the test. The kinematic strain field measurement was performed by a Canon 6D Mark II camera with an EF 100 mm f/2.8L IS USM lens.

4. Main Results

4.1 Fatigue testing

- Temperature measurement

Figs. 4-1 and 4-2 show the change in temperature θ of the LITs (different step heights in Fig. 4-1a and different step lengths in Fig. 4-1b), and CATs, respectively, of the normalized C45E (SAE1045) steel. These figures show the influence of the load path on the amount of the dissipated energy and extropy, which is also a relation between the cumulated number of cycles at the stress amplitudes applied. The evolution of the change in temperature in a CAT is in accordance with the three-stage behavior shown in Fig. 2-1. For the characterized temperature of LITs, this three-stage behavior is also applicable. For the lower steps (predominantly elastic) the mean value of the change in temperature is close to zero. For stress amplitudes above 300 MPa (elastic-plastic), the appearance of the first two stages can be observed. In contrast, the third stage indicates the specimen fracture and is through this limited to the last load level of the LIT (predominantly plastic).

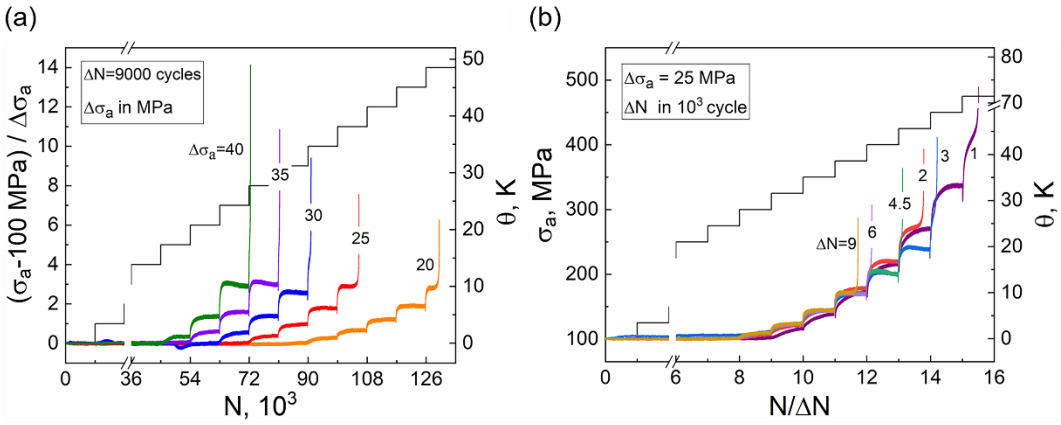

Fig. 4-1. Change in temperature vs. the number of cycles in load increase tests for (a) constant step lengths and varying step heights; (b) constant step heights and varying step lengths.

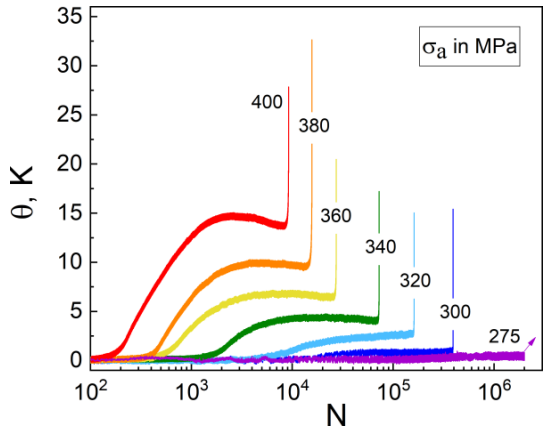

Fig. 4-2. Change in temperature vs. the number of cycles in constant amplitudes tests.

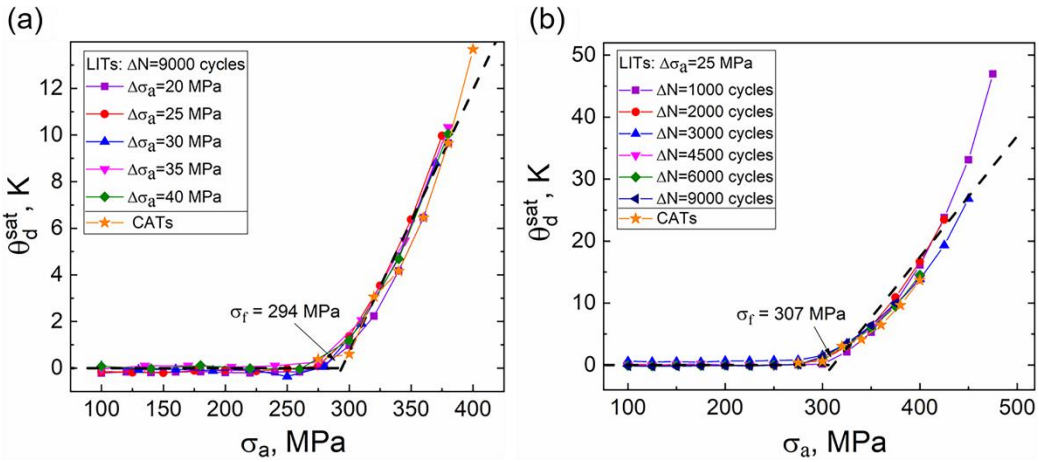

Fig. 4-3. Change in temperature in the saturated state vs. the stress amplitude in load increase tests for (a) constant step lengths ($\Delta N = 9000$ cycles) and varying step heights; (b) constant step heights ($\Delta\sigma_a = 25$ MPa) and varying step lengths.

It is noted that from Figure 4-1 the change in temperature θ in the saturated state θ_d^{sat} of each LIT load level can be considered near to constant. Fig. 4-3 provides the relation of θ_d^{sta} vs. stress amplitude. The values of θ_d^{sta} were extracted at a half number of cycles of a LIT or a CAT load level. It is indicated that when the stress amplitudes are below the fatigue limit, there occurs damage being negligible when compared stress levels above this limit. On the contrary, when stress amplitudes are above the fatigue limit, zones of localized micro-plastic deformations do appear, and dislocation reactions occur. Those processes lead to irreversible microstructural evolution processes and consequently to a rise of dissipated energy.

4.2 Quasistatic tensile testing

- Digital image correlation

The corresponding evolution of the 2D distribution of the strain rate during the quasistatic tensile test at selected points in time calculated based on the DIC results is illustrated in Fig. 4-4. Fig. 4-4b highlights the details of the Lüders band nucleation from a strain of 0.9% up to 1.65% for the medium TRIP steel in correspondence to Fig. 4-4a. The Lüders band nucleates first at the upper-right shoulder of the sample, then develops across the gauge of the sample, showing a +60° angle to the tensile direction. After the band thoroughly penetrates the width of the sample, a second band is initiated-

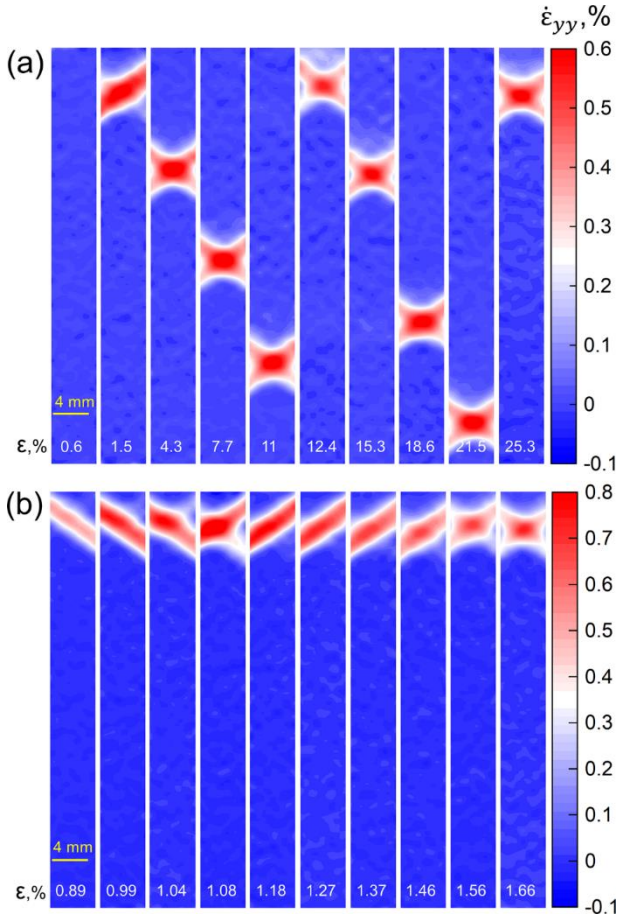

Fig. 4-4. (a) Ten strain-rate contour maps at the selected moments during a tensile test; (b) a succession of strain-rate contour maps at the selected moments during the Lüders band nucleation.

and develops through the first band, being inclined under -60° to the tensile direction. Hence, both overlapped bands form in a localized region an X-shaped strain field,

which propagates continuously downwards and eventually stops at a point. When continuing to apply tensile deformation, such bands further nucleate, almost at the same former position, and then propagated similarly from the upper to the lower end of the gauge section and are finally stopped at a characteristic strain level. After that, the X-shaped strain pattern shows up once again at the original position and stays saturated with necking until the final fracture. Such observation suggests that the deformation-induced γ→α′-martensite transformation promotes strength and ductility enhancement through the TRIP effect.

- Magnetic Barkhausen noise

Fig. 4-5 shows the variation in the curves of MBN signal intensity recorded versus coil voltage applied throughout the gauging zone. The measurement was undertaken with a cyclic magnetization along the same direction in the sample as the tension stress was applied. It can be noticed that the MBN intensity is highest in the unloaded condition, where no deformation has occurred. With increasing tensile deformation, the MBN signal intensity decreases as an overall trend. The variation of the MBN signal peak intensity and its peak position, where the peak position can be correlated to the material's coercivity, were plotted together against the strain applied along with the whole test procedure, as seen in Fig. 4-5b.

The MBN signal intensity in the elastic regime decreases nearly linearly. This is attributed to the stress-sensitive feature of MBN, which results in reduced peak height. In the plastic regime, as the deformation increases, the reduction continues, followed by a plateau until the end of the test. In the plastic instable stage until the first Lüders band initiation occurs, the change in MBN signal intensity is of particular interest. From the upper-yield point to the valley of the stress-strain curve at a strain of ~4%, the MBN peak value undergoes an irregular evolution, which may be caused by the stress relaxation of the compressive residual stress in the steel resulting from the cold rolling process [114]. After that, the MBN peak value decreases continuously until a strain of 7.5% and then fluctuates around ~9.5×10^3. The fluctuation of the MBN signal intensity is likely to be related to the plastic flow during the tensile deformation, and the macroscopic phenomenon of the plastic flow observed can be correlated to the Lüders band propagation. The signal intensity of the MBN drops to a negligible value (not

shown) at the point where the specimen reaches the final fracture, since the local magnetization is interrupted.

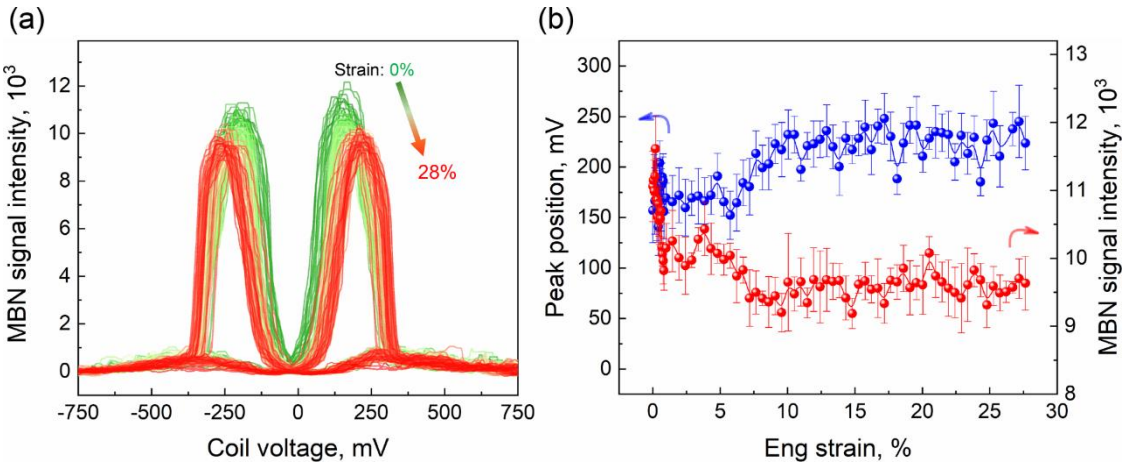

Fig. 4-5. (a) The MBN profiles measured at selected strains during the tensile test; (b) The MBN signal intensity and peak position versus the tensile strain.

5. Conclusions and Outlooks

To sum up, the present dissertation work realized the fatigue life evaluation, damage, characterization on the material of SAE 1045 steel regarding cyclic loading, especially based on the NDT method of thermography. The NDT characterization and analysis of mechanical degradation of a medium Mn TRIP steel regarding quasistatic tensile loading are also presented. Some major conclusions can be drawn as follows:

- Short-term evaluation procedures allow complete S-N data to be determined with three fatigue tests only or even less. The change in temperature has provided a wide range of possibilities to monitor the fatigue-related mechanical degradation behavior in a metallic material, such as fatigue properties and damage evolution.

- Temperature is correlated to the plastic strain, and such strain results from inhomogeneities between grains and hence strain concentrations at the microscopic scale. Those strains are considered as microplasticity strains in the HCF regime of metals and can be measured as the material’s intrinsic behavior by thermography provided the resulting temperature-inducing effects can be clearly separated from other thermal effects generated through the environment.

- Thermodynamic entropy generation can be used as an effective strategy for monitoring fatigue damage's evolution, which has been verified through various load paths. Unlike Palmgren-Miner’s rule, the proposed approach takes the temperature or the fracture fatigue entropy as an index of degradation, and a non-linear equation can be used to characterize the relationship between the mechanical degradation provided by damage and entropy generation.

- The mechanical and magnetic behavior of medium Mn TRIP steel regarding quasistatic tensile loading can be investigated through DIC, MBN, TEM, etc. The Lüders band-governed elongation can be correlated to the plastic instability, including strain-softening, strain hardening, and strain transfer. Deformation-induced martensitic transformation, behavior affects the MBN signal intensity

and coercivity of the material. This non-destructive technique opens a wide range of possibilities to characterize and understand the deformation process in ferromagnetic materials.

The above mentioned realized work have aroused the interest of some researchers, and have been cited in their related publications. What is more, the candidate wishes the SETPs can be used in the industrial application for monitoring the remaining fatigue lifetime or the damage state of the components or even the structures someday. However, some further interesting work could not be realized in the frame of this dissertation and the outlooks and suggestions are given as follows:

- It is necessary to develop and improve the theory of intrinsic dissipation, perform the related finite element simulation, and use it in the new energy analysis of the research on material fatigue and damage mechanism. Besides, the temperature measurement should be performed by different materials, e.g., metals, polymers, and composite materials.

- The fatigue life evaluation method proposed in this work should combine the mathematical statistics analysis and make it applicable for the actual engineering application. Thus, it is also essential to improve and unify relevant experimental operation procedures and criteria of the fatigue design.

- The plastic instability of the medium Mn TRIP steel can release heat, and which can be captured by an infrared camera. Thus, the full-filed heat source measurement can be utilized to investigate in-situ propagative Lüders band, including band orientation, propagation velocity. The martensitic transformation in the Lüders band can also be investigated from an energy method.

- The mechanical degradation regarding the cyclic loading of the medium Mn TRIP steel will be performed in the future, such as the evolution of the phase transformation, hardness, dislocation density. The related magnetic properties, e.g., domain wall motion, coercivity change, and others, are also interesting to investigate.

6. Summary of Papers

This chapter is a short summary of the papers that have been published by the candidate within the Ph.D. period. Full texts of those papers are attached as the second part of the dissertation.

Paper 1: Thermography in high cycle fatigue short term evaluation procedures applied to a medium carbon steel

Zhenjie Teng, Haoran Wu, Christian Boller, Peter Starke, *Fatigue Fract Eng Mater Struct*., 2020; 43(3): 515-526.

Abstract: This paper focuses on the fatigue life calculation for an unalloyed medium carbon steel SAE1045 (German DIN-standard: C45E), by applying an energy dissipation-based approach quantified through thermographic measurements. The purpose of this approach is to establish an intrinsic dissipation model and to predict characteristics derived from the cyclic deformation behavior of stress-controlled fatigue tests, e.g., the fatigue limit and the S-N data by using simplified (zero-dimensional, 0D) thermodynamic equations. In order to investigate the possibilities for a rapid evaluation while simultaneously reducing the experimental effort, one load increase test (LIT) and two constant amplitude tests (CATs) were carried out. The S-N data evaluated on such a basis is competitive to conventionally determined S-N data as will be shown.

Keywords: Thermography; medium carbon steel; intrinsic dissipation; fatigue life evaluation

Paper 2: A unified fatigue life calculation based on intrinsic thermal dissipation and microplasticity evolution

Zhenjie Teng, Haoran Wu, Christian Boller, Peter Starke, *Int J Fatigue*, 2020;131:105370.

Abstract: This paper advances a unified approach by evaluating the evolution of the intrinsic thermal dissipation and the microplasticity strain amplitude of SAE1045 steel. The intrinsic dissipation is utilized to understand the fatigue behavior and to link the materials' microstructure evolution directly. The microplasticity strain amplitude is related to a fatigue process and correlated to fatigue life that can be deducted from the change in temperature. With only one load increase test and one constant amplitude test in the present case, an S-N curve can be evaluated being in very good agreement with experimentally determined data obtained the traditional way.

Keywords: Thermography; high-cycle fatigue; intrinsic dissipation; microplasticity; fatigue life evaluation

Paper 3: Thermodynamic entropy as a marker of high-cycle fatigue damage accumulation: Example for normalized SAE 1045 steel

Zhenjie Teng, Haoran Wu, Christian Boller, Peter Starke, *Fatigue Fract Eng Mater Struct*., 2020; 43:2854-2866.

Abstract: A non-destructive thermographic methodology is utilized to determine the fracture fatigue entropy for evaluating the fatigue damage in metals within the high cycle fatigue regime. Thermodynamic entropy is shown to play an important role in the fatigue process to trace the fatigue damage as an irreversible degradation of a metallic material being subjected to cyclic elastic-plastic loading. This paper presents a method to evaluate fatigue damage in the normalized SAE 1045 steel being based on the concept of thermodynamic entropy and its non-linearities. The procedure looks to be applicable to constant and load increase tests proven by experiments.

Keywords: Thermodynamic entropy; High cycle fatigue; Fatigue damage; Damage accumulation

Paper 4: Characterization of the fatigue behavior for SAE 1045 steel without and with load-free sequences based on non-destructive, X-ray diffraction and transmission

electron microscopic investigations

H. Wu*, T. Bill, **Z.J. Teng**, S. Pramanik, K.-P. Hoyer, M. Schaper, P. Starke., *Mater Sci Eng A*. 2020; 794:139597.

Abstract: The change of mechanical stress-strain-hysteresis and different physical parameters during fatigue tests have been measured to demonstrate the fatigue behavior and damage evolution processes of metallic materials. The electrical resistance, e.g., can provide important information regarding the microstructural alteration by indicating the development of dislocation density. The states of such parameters of a fatigue specimen in a load-free sequence can represent the state of a component with a defined cyclic loading history. Therefore, conventional techniques measuring these parameters of common fatigue tests or even of service load tests with additional load-free sequences should have the application potential of remaining service life estimation and must be experimentally validated. In the scope of this paper, characteristic cycle-dependent changes of diverse physical parameters of fatigue specimens made from normalized SAE 1045 steel were determined and correlated with the residual stress state and dislocation density quantified by X-ray diffraction (XRD) and transmission electron microscopy (TEM), respectively.

Keywords: Fatigue behavior; Load-free sequence; Thermography; Electrical resistance measurement; TEM; XRD

Paper 5: Characterization and analysis of plastic instability in an ultrafine-grained medium Mn TRIP steel

Z.J. Teng*, H. Wu, S. Pramanik, K.-P. Hoyer, M. Schaper, H.L. Zhang, C. Boller, P. Starke. *In manuscript.*

Abstract: This paper is focused on the mechanical and magnetic behavior of an ultrafine-grained (UFG) medium manganese (Mn) transformation-induced plasticity (TRIP) steel in its plastic instability. The in-situ methods of digital image correlation (DIC) and magnetic Barkhausen noise (MBN) are used to macroscopically characterize the propagation of the Lüders band (stretcher-strain marks) and the evolution of MBN

activities during quasistatic tensile deformation. The evolution of microstructure during the plastic instability is ex-situ investigated using X-ray diffraction (XRD) and transmission electron microscopy (TEM) for selected plastic strain states. The results show that the plastic instability of this steel is associated with an increase of hardness and enrichment of dislocation density. It can also amplify the MBN signal, while the derived coercivity behaves reversely on an overall trend due to work hardening. The different stress response of the medium Mn steel is closely related to the kinetic martensite microstructure, which in turn modifies the domain-structure response. Thus, the MBN can be used as a potential means for the non-destructive evaluation (NDE) for the strengthening of the UFG medium Mn TRIP steel.

Keywords: Medium manganese steel; Plastic instability; Magnetic Barkhausen noise; X-ray diffraction; Transmission electron microscopy.

7. Contribution to Science

This chapter presents the contribution of the dissertation to science, and it will elaborate on the following five aspects:

- Based on the STEPs works the groups of LZfPQ at Saarland University and WWHK at Hochschule Kaiserslautern have done before, the dissertation proposes a new STEP for the fatigue life evaluation on the idea of the intrinsic dissipation model by performing LITs and CATs in fatigue. It makes a new beginning of the fatigue life evaluation in the chair. This new STEP allows to determine the complete S-N data with three fatigue tests only (which was not proposed before), one LIT and two CTAs, compared to the conventional fatigue test and which needed 20 to 30 specimens. The fatigue tests can be done within five days or even less.

- Since the intrinsic thermal dissipation is closely related to the materials' microstructure and thus it can be used to understand the fatigue behavior. Based on the work of intrinsic dissipation and the microplasticity have done before by other researchers, this dissertation combines Morrow, Manson-Coffin, and Basquin equations together and proposes a new fatigue life evaluation method from a microscopic angle in further, only two fatigue tests, one LIT and one CAT, are needed to determine an S-N curve. This method can help people better understand the mechanism of the intrinsic dissipation from the inhomogeneities between grains and hence strain concentrations at the microscopic scale. The accuracy and feasibility of the STEP for the calculated fatigue life are validated by different LITs. This new STEP for fatigue life evaluation can be done in a short time that within two days.

- The fracture fatigue entropy (FFE) model is modified in this dissertation, and it can gain further insight into the nature of FFE from the perspective of materials science. The concept and theory of FFE were firstly proposed by Prof. Michael Khonsari, Louisiana State University. The theory appears to hold very well among the materials tested so far by his group and others. However, there still exists a margin

about the evolution of the entropy rate during the fatigue testing for people to modify, e.g., the entropy generation rate for the beginning stage of the fatigue test for a metallic material cannot be higher than that of the stabilized stage and the final fracture stage. Based on the former work, this dissertation proposes a method for evaluating the plastic energy based on the intrinsic dissipation to circumvent this disadvantage and modify the energy calculation. This work has been validated from one stress level up to ~15 stress levels and which was not done before. This modified model can help the researchers better understand the entropy being the damage index in the high cycle fatigue regime. Moreover, the entropy parameter can also be an index for the rapid evaluation of fatigue life, which will be done in the future.

- Except for the temperature measurement, the dissertation comprises an additional work of the fatigue behaviors of the SAE 1045 steel with more NDTs characterization, e.g., strain, electrical resistance. XRD and TEM measurements also help to quantify the residual stress state and dislocation density during the fatigue tests. The potential of LIT, conventional CAT and CAT with load-free sequences are introduced. It is the first time to use those measurements simultaneously to investigate the fatigue behavior of this material, and such results can provide evidence for the more sensitive reliability on microscopic change of the electrical resistance measurement. The electrical resistance is well suited to characterize fatigue-induced deformation and damage processes. Thus, the implementation of electrical resistance measurement in structural integrity inspection can be expected. This dissertation can help researchers have a deeper understanding of the fatigue mechanism of the SAE 1045 steel.

- As one of the third generation of advanced high strength steels, the medium Mn TRIP steel emerges a great potential to be a strong candidate due to its excellent strength, ductility, and toughness performance. The in-situ and ex-situ measurements are performed in this material, e.g., DIC and TEM. The MBN measurement is the first time be performed and be used to evaluate the plastic instability of the medium Mn TRIP steel. The Lüders band-governed elongation is correlated to this material's plastic instability and can be observed by means of DIC. Deformation-induced martensitic transformation (DIMT) in the plastic instability

affects the material's MBN signal intensity and coercivity. Thus, the non-destructive technique of MBN used in this dissertation can open a wide range of possibilities to characterize and understand the deformation process in ferromagnetic materials.

Reference

[1] Lavenstein S, Gu Y, Madisetti D, El-Awady JA. The heterogeneity of persistent slip band nucleation and evolution in metals at the micrometer scale. Science 2020; 370:6513.

[2] ASTM 1979 American National Standard. ANSI/ASTM, E206-72.

[3] Google Image.

[4] Pu XX. Thermomechanical study of the gigacycle fatigue behavior of pure iron and carbon-manganese steels. PhD thesis 2019.

[5] Wöhler, A. Uber trebseile am Haz. Archive für Mineralogie. Geognoise, Bergbau und Hüttenkunde, Geognoise, Bergbau und Hüttenkunde 1838, 10: 215-34.

[6] Hartmann EC, Howell FM. Metal Fatigue. McGraw-Hill, New York, 1959.

[7] Fan JL. Research on rapid assessment method of fatigue parameters and fracture mechanisms of metallic materials. PhD thesis 2014.

[8] Lampman SR. Fatigue and Fracture. ASM International, Novelty 1996.

[9] Zhao SB. Anti-fatigue design. Machinery Industry Press, Beijing 1994.

[10] He C. Very high cycle fatigue behaviors and failure mechanisms of aluminum alloy welded joints. PhD thesis 2015.

[11] Conrad H. Effect of stress on the Lüders band velocity in low carbon steels. J Mech Phys Solids 1963; 11:437-440.

[12] Sharpejr WN. The Portevin-Le Chatelier effect in aluminium single crystals and polycrystals. J Mech Phys Solids 1966; 14:187-198

[13] Chang R. Phase transformation, twinning and anelastic phenomenon associated with zirconium dihydride. J Nucl Mater 1960; 2:335-340.

[14] Sato K, Ichinose M, Hirotsu Y, Inoue Y. Effects of deformation induced phase transformation and twinning on the mechanical properties of austenitic Fe–Mn–Al alloys 1989; 29:868-877.

[15] Huang ZY. Endommagement des aciers au C-Mn en fatigue oligocyclique et

gigacyclique. PhD thesis 2010.

[16] Cottrell AH, Bilby BA. Dislocation theory of yielding and strain ageing of iron. Proc Phys Soc 1949; 62(1):49-62.

[17] Wang XG, Wang L, Huang MX. Kinematic and thermal characteristics of Lüders and Portevin-Le Châtelier bands in a medium Mn transformation-induced plasticity steel. Acta Mater 2017; 124:17-29.

[18] Qiu H, Inoue T, Ueji R. Experimental measurement of the variables of Lüders deformation in hot-rolled steel via digital image correlation. Mater Sci Eng A 2020; 790:139756.

[19] Zhang M, Li L, Ding J, Wu Q, Wang YD, Almer J, Guo F, Ren Y. Temperature-dependent micromechanical behavior of medium-Mn transformation-induced-plasticity steel studied by in situ synchrotron X-ray diffraction. Acta Mater 2017; 141:294-303.

[20] Yan S, Li T, Liang, T, Chen J, Zhao, Y, Liu, X. By controlling recrystallization degree: a plain medium Mn steel overcoming Lüders deformation and low yield-to-tensile ratio simultaneously. Mater Sci Eng A 2019; 758:79-85.

[21] Wang JJ, Hui WJ, Xie ZQ. Zhang YJ, Zhao XL. Influence of pre-strain on microstructural characteristics and tensile deformation behaviour of a cold-rolled Al-containing medium Mn steel. J Mater Sci 2020;55: 5296-5310.

[22] De Cooman BC, Gibbs P, Lee S, Matlock DK, Transmission Electron Microscopy Analysis of Yielding in Ultrafine-Grained Medium Mn Transformation-Induced Plasticity Steel. Metall Mater Trans A 2013; 44:2563-2572.

[23] Liu R, Zhang ZJ, Zhang P, Zhang ZF. Extremely-low-cycle fatigue behaviors of Cu and Cu-Al alloys: damage mechanisms and life prediction. Acta Mater 2015; 83:341-356.

[24] Bathias C, Paris PC. Gigacycle fatigue in mechanical practice. New York: CRC press 2005

[25] Critieria of the ASME Boiler and Pressure Vessel Code for Design by Analysis in Sections III and VIII, Division 2. The American Society of Mechanical Engineers, New York 1969.

[26] Coffin LF. A study of the effects of cyclic thermal stresses on a ductile metal. Trans ASME 1954; 76:931-50.

[27] Manson SS. Behavior of materials under conditions of thermal stresses. NACA Rep 1954; 1170:317-50.

[28] Schijve J. Fatigue of Structures and Materials. Dordrecht, Boston: Kluwer Academic Publ 2001.

[29] Zhang Q, Zhu Y, Gao X, Wu Y, Hutchinson C. Training high-strength aluminum alloys to withstand fatigue. Nat Commun 2020; 11:5198.

[30] Zhou J, Huang HZ, Barnhart MV, Huang G, Li YF. A novel non-linear cumulative fatigue damage model based on the degradation of material memory. Int J Damage Mech 2019; 29: 610-625.

[31] Tanaka K, Mura T. A dislocation model for fatigue crack initiation. J Appl Mech 1981; 48:97-103.

[32] Lin MR, Fine ME, Mura T. Fatigue crack initiation on slip bands: theory and experiment. Acta Metal 1986; 34:619-628.

[33] Paris PC, Tada H, Donald JK, Service load fatigue damage - a historical perspective, Int J Fatigue 1999;21:35-46.

[34] Lematre J, Dufailly J. Damage measurements. Eng Fract Mech 1987;28(5-6):643-661.

[35] Zhu SP, Hao YZ, De Oliveira Correi JAF, Lesiuk G, De Jesus AMP. Nonlinear fatigue damage accumulation and life rediction of metals: a comparative study. Fatigue Fract Eng Mater Struct 2019;42(6):1271-1281.

[36] Rotem A. Residual strength after fatigue loading. Int J Fatigue 1988;10(1):27-31.

[37] Ye DY, Wang ZL. An approach to investigate pre-nucleation fatigue of cyclically loaded metals using Vickers microhardness tests. Int J Fatigue 2001; 23:85-91.

[38] Ye DY, Wang ZL. A new approach to low-cycle fatigue damage based on exhaustion of static toughness and dissipation of cyclic plastic strain energy during fatigue. Int J Fatigue 2001; 23:679-687.

[39] Jiang J, Ni F, Qiao D, Zhao Y, Kai X. Fatigue damage model of stone matrix

asphalt with polymer modified binder based on tensile strain evolution and residual strength degradation using digital image correlation methods. Measurement 2018; 123:30-38.

[40] Kocanda S. Fatigue Failure of Metals. Amsterdam: Elsevier 1986.

[41] Khonsari MM, Amiri M. Introduction to thermodynamics of mechanical fatigue. Tylor & Francis Group, CRC Press 2013.

[42] Govindaraju MR, Strom A, Jiles DC, Biner SB. Evaluation of low-cycle fatigue damage in steel structural components by a magnetic measurement technique. Springer US 1993.

[43] Miner MA. Cumulative Damage in Fatigue. J Appl Mech. Trans. ASME 1945; 67:159-164.

[44] Palmgren A. Die Lebensdauer von Kugellagern, Verfahrrenstechinik, Berlin 1924; 58:339-341.

[45] Zhu SP, Liao D, Liu Q, Correia J, Jesus A. Nonlinear fatigue damage accumulation: isodamage curve-based model and life prediction aspects. Int J Fatigue 2019; 128:105185.

[46] Mehdizadeh M, Khonsari MM. On the application of fracture fatigue entropy to variable frequency and loading amplitude. Theor Appl Fract Mech 2018; 98:30-37.

[47] Kachanov LM. Time of the rupture process under creep conditions, TVZ Akad Nauk S.S.R. Otd Tech. Nauk 1958.

[48] Rabotnov YN. Creep problems in structural members, North Holland Publishing Comp. 1969.

[49] Lemaitre J. How to use damage mechanics. Nucl Eng Des 1984; 80:233-245.

[50] Chaboche JL. Continuum damage mechanics: present state and future trends. Nucl Eng Des 1987; 105:19-33.

[51] Lemaitre J, Chaboche JL. Mechanics of Solid Materials. Cambridge University Press, Cambridge 1990.

[52] X Ma, Su S, Wang W, Yang, Y. Experimental and theoretical analysis of the correlation between cumulative plastic damage and SMFL of structural steel under

low cycle fatigue. J Magn Magn Mater 2021; 585:168292.

[53] Dyrwal A, Meo M, Ciampa F. (2018). Nonlinear air-coupled thermosonics for fatigue micro-damage detection and localisation. NDT&E Int 2018; 97:59-67.

[54] Wang XG, Crupi V, Jiang C, Guglielmino E. Quantitative thermographic methodology for fatigue life assessment in a multiscale energy dissipation framework. Int J Fatigue 2015; 81:249-256.

[55] Eifler D, Piotrowski A. Bewertung zyklischer Verformungsvorgange metallischer Werkstoffe mit Hilfe mechanischer, thermometrischer und elektrischer Messverfahren. Mat-Wiss U Werkstofftech 1995; 26:121-127.

[56] Weber W. Über die specifische Warme fester Korper insbesondere der Metalle. Ann Physik Chemie 1830; 96:177-213.

[57] Thomson W. On the Dynamical Theory of Heat, with numerical results deduced from Mr Joule's equivalent of a Thermal Unit, and M. Regnault's Observations on Steam. T. R. Soc. Edinb. 1853; 20:261-288.

[58] Stromeyer CE. The determination of fatigue limits under alternating stress conditions. Proc R Soc Lond A 1914; 90:411-425.

[60] Belgen MH. Infrared Radiometric Stress Instrumentation Application Range Study. NASA Report CR-1067 1967.

[61] MOUNTAIN, D.S. and WEBBER, J.M.B., "Stress Pattern Analysis by Thermal Emission (SPATE)", Proc Sac Photo-Opt Inst Engrs 1978; 164:189-196.

[62] Luong MP. Fatigue limit evaluation of metals using an infrared thermographic technique. Mech Mater 1998; 28:155-163.

[63] Rosa GL, Risitano A. Thermographic methodology for rapid determination of the fatigue limit of materials and mechanical components. Int J Fatigue 2000; 22:65-73.

[64] Fargione G, Geraci A, Rosa GL, Risitano A. Rapid determination of the fatigue curve by the thermographic method. Int J Fatigue 2002; 24:11-19.

[65] Plekhov O, Palin-Luc T, Saintier N, Uvarov S, Naimark O. Fatigue crack initiation and growth in a 35CrMo4 steel investigated by infrared thermography. Fatigue

Fract Eng M 2005; 28:69-178.

[66] Pastor ML, Balandraud X, Grediac M, Robert JL. Applying infrared thermography to study the heating of 2024-T3 aluminium specimens under fatigue loading. Infrared Phys Tech 2008; 51:505-515.

[67] Morabito AE, Chrysochoos A, Dattoma V, Galietti U. Analysis of heat sources accompanying the fatigue of 2024 T3 aluminium alloys. Int J Fatigue 2007; 29:977-984.

[68] Ummenhofer T, Medgenberg J. On the use of infrared thermography for the analysis of fatigue damage processes in welded joints. Int J Fatigue 2009; 31:130-137.

[69] Guo Q. Research on high-cycle fatigue property evaluation and thermal-mechanical response analysis: based on intrinsic dissipation. PhD thesis 2019.

[70] Chrysochoos A, Maisonneuve O, Martin G, Caumon H, Chezeaux JC. Plastic and dissipated work and stored energy. Nucl Eng Des 1989; 114:323-333.

[71] Doudard C, Calloch S, Cugy P, Galtier A, Hild F. A probabilistic two-scale model for high-cycle fatigue life predictions. Fatigue Fract Eng Mater Struct 2005; 28:279–288.

[72] Munier R, Doudard C, Calloch S, Weber B. Determination of high cycle fatigue properties of a wide range of steel sheet grades from self-heating measurements. Int J Fatigue 2014; 63:46-61.

[73] Amiri M, Khonsari MM. On the role of entropy generation in processes involving fatigue. Entropy 2012; 14: 24-31.

[74] Liakat M, Khonsari MM. Entropic characterization of metal fatigue with stress concentration. Int J Fatigue 2015; 70:223-234.

[75] Maquin F, Pierron F. Heat dissipation measurements in low stress cyclic loading of metallic materials: From internal friction to micro-plasticity. Mech Mater 2009; 41:928-942.

[76] Wang XG, Wang L, Huang MX. Kinematic and thermal characteristics of Lüders and Portevin-Le Châtelier bands in a medium Mn transformation-induced plasticity steel. Acta Mater 2017; 124:17-29.

[77] Mareau C, Favier V, Weber B, Galtier A, Berveiller M. Micromechanical modeling if the interactions between the microstructure and the dissipative deformation mechanisms in steels under cyclic loading. Int J Plasticity 2009; 25:106-120.

[78] Doudard C, Calloch S, Cugy P, Galtier A, Hild F. A probabilistic two-scale model for high-cycle fatigue life predictions. Fatigue Fract Eng M 2010; 28:279-288.

[79] Huang ZY, Wang QY, Wagner D, Bathias C. A very high cycle fatigue thermal dissipation investigation for titanium alloy TC4. Mater Sci and Eng A 2014; 600:153-158.

[80] Huang ZY, Liu HQ, Wang C, Wang QY. Fatigue life dispersion and thermal dissipation investigations for titanium alloy TC17 in very high cycle regime Fatigue Fract Eng M 2015; 38:1285-1293.

[81] Wang XG, Crupi V, Guo, XL, Zhao YG. Quantitative thermographic methodology for fatigue assessment and stress measurement. Int J Fatigue 2010; 32:1970-1976.

[82] Yang W, Guo X, Guo Q, Fan J. Rapid evaluation for high-cycle fatigue reliability of metallic materials through quantitative thermography methodology. Int J Fatigue 2019; 124:461-472.

[83] Curti G, La Rosa G, Orlando M, Risitano A. Analisi tramite infrarosso termico della temperatura limite in prove di fatica. In: Proceedings of the 14th Conference on the Italian Society for Stress Analysis, Catania 1986; 211-220.

[84] Rosa GL, Risitano A. Thermographic methodology for rapid determination of the fatigue limit of materials and mechanical components. Int J Fatigue, 2000; 22:65-73.

[85] Luong MP. Infrared thermographic scanning of fatigue in metals. Nucl Eng Des 1995; 158:363-376.

[86] Huang J, Pastor ML, Garnier C, Gong X. Rapid evaluation of fatigue limit on thermographic data analysis. Int J Fatigue 2017; 104:293-301.

[87] Amiri M, Khonsari MM. Life prediction of metals undergoing fatigue load based on temperature evolution. Mater Sci Eng A 2010; 527:1555-1559.

[88] Jiang L, Wang H, Liaw PK, Brooks CR, Klarstrom DL. Characterization of the

temperature evolution during high-cycle fatigue of the ULTIMET superalloy: experiment and theoretical modeling. Metall Mater Trans A 2001; 32:2279-2296.

[89] Huang Y, Li SX, Lin SE, Shih CH. Using the method of infrared sensing for monitoring fatigue process of metals. Mater Eval 1984; 42:1020-1024.

[90] Boulanger T, Chrysochoos A, Mabru C, Galtier A. Calorimetric analysis of dissipative and thermoelastic effects associated with the fatigue behavior of steels. Int J Fatigue 2004; 26:221-229.

[91] Crupi V. A unifying approach to assess the structural strength. Int J Fatigue 2008; 30:1150-1159.

[92] Wang XG, Crupi V, Jiang C, Feng ES, Guglielmino E, Wang CS. Energy-based approach for fatigue life prediction of pure copper. Int J Fatigue 2017; 104:243-250.

[93] Zhang HX, Guo SF, Yan ZF, Liu XQ, Wu GH, Pei FF, Wang WX, Wang K. Rapid determination for fatigue parameters of AZ31B magnesium alloy based on evolution of temperature under high cyclic fatigue. Mater Sci Tech 2014; 30:1820-1825.

[94] Zhang HX, Wu GH, Yan ZF, Guo SF, Chen PD, Wang WX. An experimental analysis of fatigue behavior of AZ31B magnesium alloy welded joint based on infrared thermography. Mater Design 2014; 55(6):785-791.

[95] Feng ES, Wang XG, Jiang C. A new multiaxial fatigue model for life prediction based on energy dissipation evaluation. Int J Fatigue 2019; 122:1-8.

[96] Meneghetti G. Analysis of the fatigue strength of a stainless steel based on the energy dissipation. Int J Fatigue 2007; 29:81-94.

[97] Starke P. StressLife$_{tc}$ - NDT-related assessment of the fatigue life of metallic materials. Mater Test 2019; 61:297-303.

[98] Morrow JD. Cyclic plastic strain energy and fatigue of metals. Internal friction, damping, and cyclic plasticity. ASTM STP 1965; 378:45-87.

[99] Basquin OH. The exponential law of endurance tests. Am Soc Test Mater Proc 1910; 10:625-630.

[100] Ramberg W, Osgood WR. Description of stress–strain curves by three parameters, Technical Note No. 902, National Advisory Committee for Aeronautics, Washington DC 1943.

[101] Li J, Zhang Z, Li C. An improved method for estimation of Ramberg-Osgood curves of steels from monotonic tensile properties. Fatigue Fract Eng M 2016; 39:412-426.

[102] R. Acosta, C. Boller, P. Starke, M. Jamrozy, M. Knyazeva, F. Walther, K. Heckmann, J. Sievers, T. Schopf, S. Weihe, Non-destructive testing derived parameters for microstructure-based residual service life assessment of aging metallic materials in nuclear engineering. MP Materials Testing 61, 2019; 11: 1029-1038.

[103] Starke P. Fatigue life calculation for cyclically loaded materials by using non-destructive testing methods. Habilitation thesis 2020.

[104] Starke P, Wu H, Use of non-destructive testing methods in a new one-specimen test strategy for the estimation of fatigue data. Int J Fatigue 2018; 111:177-185.

[105] Wu H, Baumchen A, Engel A, Acosta R, Boller C, Starke P, SteBLife-a new short-time procedure for the evaluation of fatigue data, Int J Fatigue 2019; 124:82-88.

[106] Acosta R, Wu H, Venkat RS, Weber F, Starke P. SteBLife, a new approach for the accelerated generation of metallic materials' fatigue data. Metals 2020; 10:1-17.

[107] Barkhausen H. Two phenomena revealed with the help of new amplifiers. Phys1919; 20:1-3.

[108] Shen GT, Zheng Y, Jiang ZP, Tian JD. The development status of magnetic Barkhausen noise technique. Nondestruct Test 2016; 38:66-74.

[109] Amiri MS, Thielen M, Rabung M, Marx M, Szielasko K, Boller C. On the role of crystal and stress anisotropy in magnetic Barkhausen noise. J Magn Magn Mater 2014; 372:16-22.

[110] Moorthy V, Shaw BA, Evans JT. Evaluation of tempering induced changes in

the hardness profile of case-carburised En36 steel using magnetic Barkhausen noise analysis. NDT&E Int 2003; 36:43-49.

[111] Altpeter I, Dobmann G, Kroening M, Rabung M, Szielasko S. Micro-magnetic evaluation of micro residual stresses of the IInd and IIIrd order. NDT&E Int 2009; 42:283-290.

[112] Moorthy V, Shaw BA, Hopkins P. Magnetic Barkhausen emission technique for detecting the overstressing during bending fatigue in case-carburised En36 steel. NDT&E Int 2005; 38:159-166.

[113] Spittel M, Spittel T. Metal Forming data of ferrous alloys-deformation behavior. Steel symbol/number: C45/1.0503. In H. Warlimont (Ed.). Springer-Verlag Berlin Heidelberg 2009; 210-215.

[114] Mohapatra JN, Akela AK. Magnetic evaluation of tensile deformation behaviour of trip assisted steels. J Nondestruct Eval 2019; 38:22.

PART II

PAPER 1

Thermography in high cycle fatigue short term evaluation procedures applied to a medium carbon steel

Zhenjie Teng*, Haoran Wu, Christian Boller, Peter Starke

Fatigue Fract Eng Mater Struct, 2020; 43: 515-526. DOI: 10.1111/ffe.13136

Copyright:

The following is reproduced with the permission from Copyright (2019) Wiley Publishing Ltd. John Wiley and Sons. This work is licensed under a number of 5184131447554.

Thermography in high cycle fatigue short term evaluation procedures applied to a medium carbon steel

Zhenjie Teng [a, b, *], Haoran Wu [a, b], Christian Boller [a], Peter Starke [a, b]

[a] *Chair of Non-Destructive Testing and Quality Assurance, Saarland University, Germany*

[b] *Department of Materials Sciences and Materials Testing, University of Applied Sciences Kaiserslautern, Germany*

Abstract

This paper focuses on the fatigue life calculation for an unalloyed medium carbon steel SAE1045 (German DIN-standard: C45E), by applying an energy dissipation-based approach quantified through thermographic measurements. The purpose of this approach is to establish an intrinsic dissipation model and to predict characteristics derived from the cyclic deformation behavior of stress-controlled fatigue tests, e.g., the fatigue limit and the S-N data by using simplified (zero-dimensional, 0D) thermodynamic equations. In order to investigate the possibilities for a rapid evaluation while simultaneously reducing the experimental effort, one load increase test (LIT) and two constant amplitude tests (CATs) were carried out. The S-N data evaluated on such a basis is competitive to conventionally determined S-N data as will be shown.

Keywords: Thermography; medium carbon steel; intrinsic dissipation; fatigue life evaluation

Nomenclature

C	specific heat capacity (J kg^{-1} K^{-1})	α	internal variables
d_1	intrinsic dissipation term (J m^{-3} s^{-1})	λ	linear expansion coefficient (K^{-1})
E	Young's modulus (MPa)	ρ	mass density (kg m^{-3})
E_c	dissipated energy (J m^{-3})	$\boldsymbol{\varepsilon}$	strain tensor
f	loading frequency (s^{-1})	$\varepsilon_{a,p}$	plastic strain amplitude
k	thermal conduction coefficient (W m^{-1} K^{-1})	$\boldsymbol{\sigma}$	Cauchy stress tensor (MPa)
N	number of cycles	σ_a	stress amplitude (MPa)
N_f	fatigue life	σ_f	fatigue limit (MPa)
$N_{f,c}$	calculated fatigue life	θ	change in temperature (K)
r_{ext}	external heat source (W m^{-3})	$\theta_{a.the}$	Thermoelastic relation (K)
R	stress ratio	θ_d^{sta}	saturated change in temperature (K)
s	overall heat source (W m^{-3})	Δ	Laplace operator
s_{ic}	internal coupling source (W m^{-3})	$\Delta\sigma_a$	load increase step (MPa)
s_{the}	thermoelastic source term (W m^{-3})	ΔN	load step length
t, τ	time (s)	$\Delta\theta_{the}$	thermoelastic range (K)
T	absolute temperature (K)	τ_{eq}	time constant (s)
T_0	equilibrium temperature field (K)	ψ	Helmholtz free energy (J m^{-3})
W_h	equivalent heat (J m^{-3})	$\emptyset$	energy related parameter (K cycle)

1. Introduction

The conventional way to determine an S-N dataset for a certain material in the high-cycle-fatigue (HCF) regime can require about 20-30 specimens and take about two months to get the data obtained under cyclic loading at a given load frequency such as 5 Hz. This is very time-, specimen- and consequently cost-consuming and seeks for more efficient methods in the end. Fatigue is an irreversible process accompanied by localized as well as permanent microstructure evolutions finally leading to failure of specimens, components, or whole structures. Repeated elastic-plastic deformations result from a thermodynamical point of view in a microstructure-related heat dissipation within a specimen's volume, where the resulting characteristics can be derived from the temperature and/or its change. The area of the stress-strain hysteresis loop describes the energy that must be applied to plastically deform the specimen during fatigue loading. Since energy cannot simply be extinguished, it is transformed into the internal energy and heat energy [1]. The internal energy enables microstructural changes such as dislocation reactions, micro- and macro-cracking as well as their propagation processes. The predominant proportion of 90-95% of the deformation energy dissipates as heat, which is why the temperature change can be correlated directly with the plastic deformation or the cumulative damage [2,3]. Through the very good heat conductivity of metallic materials, the change in temperature, which is related to the dissipated heat energy can be measured on the specimens' surface. Over the past decades, thermographic measurements have already been widely used along fatigue tests as a non-destructive testing (NDT) method mainly in view of determining fatigue properties.

Risitano et al. [4,5] applied thermography to evaluate the damage accumulation of unalloyed C40 medium carbon steel and to estimate the fatigue limit by using the One Curve Method. Luong [6,7] considered the temperature below the fatigue limit and developed a Two Curve Method. Based on the pioneering work of Morrow and Basquin, Starke et al. [8,9] developed the Physically Based Fatigue Life calculation (PHYBAL) method as a Short-Term Evaluation Procedure (STEP) based on conventional (strain) and non-destructive (temperature and electrical resistance) methods, with which only three fatigue tests are required to determine the complete dataset of a trend S-N curve. Results obtained have shown that the S-N dataset determined is in full agreement with conventionally determined S-N curves. In order to achieve a further reduction of the

experimental efforts, the new SteBLife approach has been recently developed [10,11], where the S-N data can even be determined from a small number or at last one single fatigue test using a specially step-shaped specimen. Guo et al. [12] investigated the relationship between temperature and stress distribution of an hourglass specimen and showed a satisfying way to determine the fatigue limit of a magnesium alloy when compared to the state-of-the-art.

However, the thermal-variations shown by specimens during fatigue processes are not only an intrinsic manifestation of the microstructural evolution during the fatigue loading process, but can also be influenced by heat conduction, convection, and radiation generated through the environment. Chrysochoos et al. [13,14] separated the thermoelastic source and dissipative source of the heat generated during fatigue processes of steel with calorimetric analysis through an infrared camera. Based on this approach, Mareau et al. [15,16] examined the interactions between the free surface, the mean stress, and the heat dissipation of steel specimens during fatigue processes. Subsequently, they proposed a micromechanical model to describe the relationship between microstructure and dissipative deformation mechanisms in a ferritic steel. This mechanism takes the dislocation oscillations (anelastic) and plastic slip (inelastic) at the scale of the slip system into account by using a crystal plasticity framework. Connesson et al. [17,18] investigated the materials' microstructure evolution based to the cumulated plastic strain and the dissipated energy due to the internal friction and they proposed an improved model to describe the energy balance during the very first cycles at low stress levels. Wang et al. [19,20] proposed an effective method to evaluate an S-N curve by using a thermal parameter, which is determined from the dissipation rate as a characteristic measure of fatigue resistance. Guo et al. [21,22] introduced an intrinsic dissipated fatigue life prediction model for HCF based on the energy method as fatigue damage evolution is an energy dissipation process accompanied with temperature variation. Poncelet et al. [23] focused on probabilistic multiscale models and the parameters derived therefrom for the prediction of fatigue properties in the HCF regime. One of the models was relied on a yield surface and accounted for stress multiaxiality at the micro-scale. Another model was based on a probabilistic model of micro-plasticity at the slip-planes scale. Finally, thermal effects and fatigue limit predictions were in consistency with experimental results.

However, the work mentioned above has not taken the effect of the applied load-time-histories versus damage on the behavior of an intrinsic dissipation measured into account. Also, whether the values of the total dissipated energy of every single test are in a comparable range, independently from the load amplitude, load frequency, load-time function, load spectrum, etc. has not been discussed yet. Within the framework of the previous investigations, the work presented here, therefore, aims at investigating the fatigue effects on the thermal dissipation demonstrated on SAE1045 steel under increasing and constant amplitude loading, as it appears in a load increase test (LIT) and a constant amplitude test (CAT). A LIT has to be considered as a fatigue test where a specimen is loaded for a limited number of cycles (usually a few thousand cycles until the material stabilizes) at a load level under constant amplitude loading, consecutively followed by an increase to a next higher load level repeated until specimen fractures appear. A CAT is a classical fatigue test where the loading amplitude does not change. The structure of this paper is as follows: The first paragraph provides a brief review of the thermal dissipation theory, which is deduced from the literature and it is necessary to interpret the findings from the investigations (section 2). This is followed by the explanation of the test set-up and the specific experimental procedures developed (Section 3). After that, the experimental results are presented and discussed, a STEP for the fatigue life calculation can be given in a very rapid way based on the energy method (Section 4). Some conclusions are given in final.

2. Thermodynamic framework

Fatigue can be specified as a cyclic irreversible damage evolution process leading to microstructural changes resulting in energy dissipation. Most of the dissipated energy during the fatigue process is released in the form of thermal energy, causing changes in the temperature of the material's surface even in the case of metallic materials showing a good thermal conductivity. Numerous experiments have proven that three stages of temperature evolution of a specimen or a component can be observed if the load amplitude is above the fatigue limit where plasticity becomes a lifetime limiting factor [5,7,19-21,24-31]: an initial temperature increase stage (stage I), a predominant temperature stabilized stage (stage II), and a sudden temperature increase stage before fracture (stage III), which is schematically presented in Fig. 1. Among those three stages, stage II occupies about 90% of the fatigue life for many iron-carbon alloys [21]. Thus,

the temperature variation of stage II is widely used as an indicator for the evolution of a fatigue process and hence for the estimation of fatigue parameters.

In this paper, it is assumed that the measured surface temperature is very close to the bulk temperature caused through the fact that metallic materials have a high thermal conductivity rate and the specimen diameter is only 6 mm. This assumption can be proven for specimens with a cylindrical diameter on the basis of the Thomson equation by using temperature values from experiments in the thermoelastic range [32].

Considering there is no coupling effect between the microstructure describing variables and temperature, and neglecting the convective terms, a one-dimensional heat equation can be formulated by combining the first and second principles of thermodynamics as to the following [33]:

$$\rho C\dot{T} - \mathrm{div}(k\colon \mathrm{grad}T) = \left(\boldsymbol{\sigma} - \rho\psi_{,\varepsilon}\right)\colon \dot{\boldsymbol{\varepsilon}} - \rho\psi_{,\alpha}\colon \dot{\alpha} + \rho T\psi_{,T\varepsilon}\colon \dot{\boldsymbol{\varepsilon}} + \rho T\psi_{,T\alpha}\colon \dot{\alpha} + r_{ext} \quad (1)$$

where, ρ is the mass density, C the calorimetric heat, k the conduction coefficient, and $\boldsymbol{\sigma}$ the Cauchy stress tensor, T the absolute temperature, $\boldsymbol{\varepsilon}$ the strain tensor, ψ the Helmholtz free energy, α the internal variables that sum up the microstructural state of the material. On the right-hand side of the equation $d_1 = \left(\boldsymbol{\sigma} - \rho\psi_{,\varepsilon}\right)\colon \dot{\boldsymbol{\varepsilon}} - \rho\psi_{,\alpha}\colon \dot{\alpha}$ is the intrinsic dissipation term, $s_{the} = \rho T\psi_{,\varepsilon}\colon \dot{\boldsymbol{\varepsilon}}$ is the thermoelastic source term, $s_{ic} = \rho T\psi_{,T\alpha}\colon \dot{\alpha}$ is the internal coupling source and r_{ext} is the external heat source, respectively.

In order to quantify the heat source by infrared thermography processing, the following hypotheses are made:

- Mass density and specific heat are material constants independent of the thermodynamic state.
- The external heat supply r_{ext} is characterized by the heat exchange between specimen and environment. It can be influenced by heat conduction, convection, and radiation. These variables are very hard to be estimated as they strongly rely on the boundary conditions of the test set-up. Thus, r_{ext} is supposed to be time-independent and can be written as [27]:

$$r_{ext} = -k\Delta T_0 \tag{2}$$

where Δ is the Laplace operator and T_0 the equilibrium temperature field. Because the fatigue tests were performed in an air-conditioned environment with a constant temperature (± 2 K), the initial temperature of the specimen at the beginning of the test can be set to ambient temperature.

- The increase in temperature during the test has no influence on the microstructure if a certain temperature value is not exceeded. Normally this value is set to a maximum change in temperature of 40 K. The coupling source s_{ic} under the given boundary conditions can be neglected in Eq. (1) as the thermal processes due to fatigue are considered as pure dissipation mechanisms.

Under those hypotheses Eq. (1) can be rewritten in the following form [33]:

$$\rho C \frac{\partial \theta}{\partial t} - k\Delta\theta = s = s_{the} + d_1 \tag{3}$$

where $\theta = T - T_0$ indicates the change in temperature, s denotes the overall heat source due to the thermoelastic effect and the heat dissipation processes.

To further simplify Eq. (3) it is assumed that the heat source distribution is consistent at any time before a localization of temperature is set in the stress and strain fields being applied. A 0D model has been proposed by Boulanger et al. [13] to solve Eq. (3). For symmetric linear boundary conditions (i.e., upper and lower part of the specimen are geometrically the same) and initial conditions corresponding to a uniform temperature distribution, based on the heat loss due to heat conduction, convection and radiation, which is linear to the temperature variation θ, $-k\Delta\theta$ can be approximated using the following relationship [13]:

$$-k\Delta\theta = \rho C \frac{\theta}{\tau_{eq}} \tag{4}$$

where symbol τ_{eq} denotes a time constant characterizing the thermal exchange (e.g., thermal convection and thermal radiation) between the specimen and its environment. Hence, the heat diffusion can be rewritten as the following equation:

$$\rho C\left(\frac{d\theta}{dt}+\frac{\theta}{\tau_{eq}}\right)=s_{the}+d_1 \tag{5}$$

Eq. (5) can be used to separate the temperature sources. Therefore, the term expressing the temperature of thermoelasticity θ_{the} can be induced by s_{the}. It is assumed that the thermoelastic behavior is isotropic and linear, and the volume of the thermoelastic source can be approximated as [34]:

$$s_{the}\approx-\lambda T_0(\dot{\sigma}+\lambda E\dot{\theta}) \tag{6}$$

where $\dot{\sigma}$ is the stress rate within the loading function, E the Young's modulus, and λ the linear thermal expansion coefficient. The value of $T_0E\lambda^2/\rho C$ obtained by entering Eq. (6) into Eq. (5) can be set to 0 when taking the data in Table 2 into account. Even if the temperature is close to the thermal equilibrium $\theta \ll T_0$, d_1 can be neglected. If this is taken into consideration in Eq. (5) and Eq. (6) is used to express s_{the}, Eq. (7) can be derived:

$$\frac{d\theta}{dt}+\frac{\theta}{\tau_{eq}}=-\frac{\lambda T_0}{\rho C}\dot{\sigma} \tag{7}$$

For a sinusoidal cyclic loading, σ can be expressed as a time dependent function:

$$\sigma(t)=\sigma_a\sin(2\pi f t) \tag{8}$$

where f indicates the loading frequency and σ_a the stress amplitude.

Following that Eq. (7) can be written as [13]:

$$\theta_{the}(t)=-\frac{2T_0\lambda\sigma_a}{\rho C}\frac{\pi f}{\sqrt{\tau_{eq}^{-2}+4\pi^2 f^2}}\sin(2\pi f t+\varphi) \tag{9}$$

where $\varphi=\arctan(2\pi f\tau_{eq})$. From Eq. (9) one can get the thermoelastic range as follows:

$$\Delta\theta_{the}=\frac{2T_0\lambda\sigma_a}{\rho C}\frac{2\pi f}{\sqrt{\tau_{eq}^{-2}+4\pi^2 f^2}} \tag{10}$$

and the thermoelastic relation results in:

$$\theta_{a.the} = \frac{\Delta\theta_{the}}{2} = \frac{T_0 \lambda \sigma_a}{\rho C} \frac{2\pi f}{\sqrt{\tau_{eq}^{-2} + 4\pi^2 f^2}} \quad (11)$$

Here τ_{eq} =80 s is used as suggested in the literature which looks to be valid for common steels [13].

3. Experimental details

3.1. Material and specimen

The material investigated is the unalloyed medium carbon steel designated as SAE1045 (German DIN-standard: C45E) and being widely used for engineering components and structural parts. The material was delivered as round bars with a diameter of 20 mm and a length of 5 m with a scaly surface because of heat treatment. The microstructure consisted of a ferritic-pearlitic portion resulting in an ultimate strength of 710 MPa, a yield strength of 413 MPa, and a Brinell hardness of 210, respectively. The chemical composition and material properties are given in Tables 1 and 2.

All specimens tested were machined from the steel bars with the length direction being parallel to the rolling direction. The hourglass shaped specimen geometry and dimensions are given in Fig. 2. Since infrared thermography was applied during the fatigue tests, the specimens were painted with a thin mat black coating to increase their thermal emissivity (emission factor 0.97), avoiding reflections from the environment and enhancing the reliability of the temperature measurements.

3.2. Experimental setup

The experiments were performed on a Shimadzu type RHF-L servo-hydraulic testing machine with a 21/25 kN cyclic/quasi-static load capacity up to a maximum number of 2×10^6 cycles or specimen failure. Tests were run under load control mode at a stress ratio of $R = -1$ and a load frequency of 5 Hz. Further details regarding the fatigue testing setup can be found in the literature [10,11]. During fatigue tests, the temperature of the specimen surface was recorded as a result of the average temperature of a defined square measurement area (10×10 pixels) in the middle of the gauge length. The IR-camera used is a Micro-Epsilon ThermoIMAGER type TIM450, with a spectral range

between 7.5 and 13 μm, an optical resolution of 382×288 pixels and thermal sensitivity of 0.04 K, respectively.

To ensure the stability of temperature conditions and avoid heat conduction from the upper and lower grips being connected to the servohydraulic circuit, the grips were continuously thermally stabilized by a Peltier-element cooled water-circuit. The complete experimental set-up is shown in Fig. 3.

3.3. Fatigue test procedures

The combination of LITs and CATs allows fatigue parameters to be identified and heat dissipation mechanisms to be analyzed. A schematic load-time history of a LIT is shown in Fig. 4. The details for LITs and CATs used here have been set as follows:

- Test 1: LITs with block load-step length of ΔN =9000 cycles each. Five tests were started at $\sigma_{a,start}$ =100 MPa, with different load-increase steps of $\Delta\sigma_a$ =20, 25, 30, 35, 40 MPa analyzed;
- Test 2: LITs with a stepwise-load increase $\Delta\sigma_a$ kept at 25 MPa. Five tests were started at $\sigma_{a,start}$ =100 MPa, with varying step lengths of ΔN =1000, 2000, 3000, 4500, 6000 cycles, respectively;
- Test 3: Seven CATs at stress amplitudes σ_a =275, 300, 320, 340, 360, 380, 400 MPa, respectively.

In order to avoid too big data volumes, the infrared camera was set to a recording frequency of 100 Hz. Environmental noise effects were neglected by using software embedded filters.

4. Results and discussion

4.1. Results of thermal investigations

The evolution of the change in temperature θ in LITs and CATs are given in Fig. 5 and Fig. 6, respectively. In test 1 and test 2, the value of θ was set to 0 before the cyclic loading was applied. After starting the fatigue loading, the temperature evolution process in a CAT (shown in Fig. 6) is in accordance with the three-stage-behavior

shown in Fig. 1. Also, for the temperature-based characterization of the cyclic deformation behavior of LITs (shown in Fig. 5) this three-stage-behavior is applicable, whereby for the lower steps (predominantly elastic) the mean value of the change in temperature is close to zero. For stress amplitudes above σ_a =300 MPa (elastic-plastic) the appearance of the first two stages can be observed, whereas the third stage indicates the specimen fracture and is through this limited to the last load level of the LIT (predominantly plastic).

In order to estimate the fatigue limit, Luong [6,7] used the abscissa value, which corresponds to the intersection point of two straight lines of the LITs' describing the surface temperature of the specimen in the elastic and plastic range, and the schematic illustration is given in Figure 8. From the fitted lines (marked in black in Fig. 7), the intersection is seen to be an average value of σ_f = 300 MPa for the investigated SAE 1045 steel. This estimated value of the fatigue limit from the LITs is in good agreement with the conventionally determined fatigue limit when considering the CATs (test 3).

Following the approach by Eq. (11), the relationship between the thermoelastic relation $\theta_{a,the}$ and stress amplitude σ_a can be fitted to a straight line, even in the transition state when the material is slightly plastic deformed (Fig. 9, on the right from the dotted line). Fig. 9 presents the temperature amplitude due to the thermoelastic relation of LITs at each load level. The results derived from the approach (Eq. (11)) are in a good agreement with experimental ones, with a slight deviation for the results of the LIT with $\Delta\sigma_a$ =20 MPa and ΔN =9000 cycles. It is verified that 0D simplified thermodynamic equations (Eqs. (7) and (11)) can be used for the described applications. As previously expected, the higher the stress amplitude is, the higher the thermoelastic relation becomes.

4.2. Heat dissipation

In order to investigate the intensity of the thermoelastic and the dissipative heat source, a combined heat source $s(t)$ is estimated by using a finite difference approximation of the differential operator of Eq. (5) and which can be rewritten as:

$$s = \rho C(\dot{\theta} + \frac{\theta}{\tau_{eq}}) \tag{12}$$

When integrating the combined heat source in accordance to Eq. (12) the heat W_h is obtained, and can be expressed through Eq. (13)

$$W_h = \int_0^\tau s(t)dt \tag{13}$$

This heat can be defined as the equivalent dissipated energy caused by the fact, that the thermoelastic energy is vanishing at the end of each loading cycle.

The results of the accumulated dissipated energy are shown in Fig. 10. In the elastic regime, the cumulation of dissipated energy is lower and is not in full accordance with the theoretical background. This is possibly resulted from the low load frequency, which might provide the uncertainties values that it can be caused by the surrounding conditions and the fact that the change in temperature θ in the elastic regime is close to zero and there are small changes in the ambient temperature. It shows that W_h increases progressively from cycle to cycle in the micro-plastic regime and the dissipated energy data can be approximated by straight lines for each load level of the LIT through a least-squares fit. By computing slopes of those lines (shown in Fig. 10 a), one can get the equivalent intrinsic dissipation rate $d_1/\rho C$ under different load levels. The relationship between the equivalent intrinsic dissipation rate and the stress amplitudes is plotted in Fig. 11 showing an exponential growth. As can be seen from Fig. 11, the equivalent intrinsic dissipation rates of the CATs are meeting the trend of the LITs. It can, therefore, be assumed that the thermodynamic model used here looks to be independent of the load-time-history applied and the intrinsic dissipation rate reaches the same value for a given stress, independent of the load sequence having been applied before. Hence the damage condition, at least as an average per load level in the LIT. However, the intrinsic dissipation rate follows a non-linear relationship with the stress being applied, which makes it interesting to be considered for further damage accumulation assessments.

4.3. Thermography based STEP for S-N data determination

The total cumulated dissipated energy E_c for fatigue failure of a specimen can be calculated by accumulating the damage induced equivalent intrinsic dissipation rate $d_1/\rho C$ of the CATs, where E_c can be expressed as:

$$E_c = \int_0^{N_f} \frac{d_1}{f} dt \tag{14}$$

The resulting relationship is given in Fig. 12. The correlation between the total dissipated energy of each specimen and different stress amplitudes shows an exponential declining tendency.

Based on the theory that fatigue failure occurs once the total dissipated energy reaches a certain value, where it has been postulated that there is a threshold value of total dissipated energy which can be considered as a material constant being independent of the load-time history [21]. However, it is clearly shown that the energy dissipation of SAE 1045 steel decreases with the increase of the stress amplitude value. Another energy related parameter $\emptyset = \int_0^{N_f} \theta \, dN$, proposed by Risitano [5] for different load-time functions of the stress amplitude versus the fatigue limit being a constant cannot be confirmed by the findings described here when taking the data in Fig. 6 into account. The relationship between $\emptyset$ and the stress amplitude not explicitly shown here provides a behavior comparable to that shown in Fig. 12.

Mareau et al. [15] found as well that the dissipative mechanisms are totally different depending on the stress amplitude. For lower stress amplitudes the dissipation is dependent on an anelastic mechanism, where the strain is irreversible but can be recovered from a mechanical point of view. For higher stresses, the dissipative mechanism is inelastic, where strain is irreversible and unrecoverable. A more detailed explanation for the total dissipated energy for SAE1045 steel which is from the findings not constant for tests with hourglass shaped specimens in the HCF regime has to be given in the future and is an initial point for further research activities. The transition from an anelastic to an inelastic dissipation mechanism could be responsible for the different total dissipated energy of an SAE1045 steel for CATs with the critical threshold stress amplitude of 350 MPa taken from Fig. 12.

The calculated number of cycles to failure $N_{f.c}$ for different stress amplitudes can be given by using Eq. (15)

$$N_{f.c} = \frac{E_c}{d_1/f} \tag{15}$$

As the total dissipated energy in CATs follows an exponential decline, the micro-plastic range identified in a LIT can be divided into two stress amplitude regions. From an evolution of the change in temperature θ in the LIT curve, one can define the stress range of the HCF regime. Here E_c is described as an either linear or hyperbolic function determined by the experimental values obtained at stress amplitudes of 320 MPa and 380 MPa as shown in Fig. 12 and then divided by the intrinsic dissipation rate of each corresponding stress amplitude level in the LIT of the two regions respectively. Fig. 13 shows the comparison between the estimated fatigue lives based on the energy approach of the LITs and the S-N data evaluated in conventional CATs. The estimated S-N data based on loads and fatigue cycles are in very good agreement with the results obtained the conventional way, however, the latter requiring a much larger number of specimens.

In summary, the approach made that a material has an energy potential that can be dissipated as a result of the fatigue process may open a variety of new considerations on how energy could be analyzed in focus of describing damage accumulation along a randomized service load sequence and can determine the fatigue lives of a material independent of load load-time-history by calculating the intrinsic dissipation rate in the LIT and the total energy dissipation in the CATs. Significant advantages with respect to materials data generation can be expected.

5. Conclusions

Short term evaluation procedures allow complete S-N data to be determined with three fatigue tests only or even less. The evaluation is done based on the classical parameters such as stress and strain. However, there is a variety of other physical parameters mostly related to non-destructive evaluation methods that can be used to characterize a material's loading, fatigue behavior, and damage evolution. One of these quantities is the temperature or its change where thermography has provided a wide range of possibilities. Stress controlled load increase tests (LITs) and constant amplitude tests (CATs) with a load ratio of $R = -1$, performed at room temperature on hourglass specimens of unalloyed medium carbon steel SAE1045 have allowed to draw the following main conclusions:

(1) When the stress amplitude in LITs is above the first micro plastic deformations, the specimens' surface temperature increases with increasing stress amplitude. The

intersection of two straight lines, fitted from the stabilized temperature in the elastic and microplastic regime, can be regarded as the fatigue limit.

(2) The simplified intrinsic dissipation calculation model can be used for cylindrical specimens. The energy method applied uses the intrinsic dissipation of the material as an indicator for microstructural changes and damage evolution processes leading to characteristic values such as the fatigue limit.

(3) The intrinsic dissipation rate can be directly related to the stress amplitude independent of what sequence has been applied to the LIT. The energy method based on the intrinsic dissipation in the process of accumulation of fatigue damage can be used to predict the S-N data of a material with a fraction of effort when compared to conventional means.

(4) The short-term evaluation procedure requires three specimens in total, one load increase test (LIT) and two constant amplitude tests (CATs) when comparing to the traditional fatigue test which needed 20-30 specimens. Two CATs can give the total dissipated energy for high and low stress loads, and the satisfied S-N data can be calculated via the dissipated energy divided by the intrinsic dissipation rate of each stress level in LIT.

Acknowledgments

The authors would like to thank the financial support from the German Research Foundation (Deutsche Forschungsgemeinschaft DFG, STA 1133/6-1) and the China Scholarship Council.

References

[1] Meneghetti G, Ricotta M, Atzori B. A two-parameter, heat energy-based approach to analyse the mean stress influence on axial fatigue behaviour of plain steel specimens. Int J Fatigue. 2016; 82:60-70.

[2] Wang XG, Feng ES, Jiang C. A microplasticity evaluation method in very high cycle fatigue. Int J Fatigue. 2017; 94:6-15.

[3] Eifler D, Piotrowski A. Bewertung zyklischer Verformungsvorgange metallischer

Werkstoffe mit Hilfe mechanischer, thermometrischer und elektrischer Messverfahren. Mat-Wiss U Werkstofftech 1995; 26:121-127.

[4] Risitano A, Risitano G. Cumulative damage evaluation of steel using infrared thermography. Theor App Fract Mech. 2010; 54:82-90.

[5] Risitano A, Risitano G. Cumulative damage evaluation in multiple cycle fatigue tests taking into account energy parameters. Int J Fatigue. 2013; 48:214-222.

[6] Luong MP. Infrared thermographic scanning of fatigue in metals. Nucl Eng Des. 1995; 158:363-376.

[7] Luong MP. Fatigue limit evaluation of metals using an infrared thermographic technique. Mech Mater. 1998; 28:155-163.

[8] Starke P, Walther F, Eifler D. PHYBAL – A new method for lifetime prediction based on strain, temperature and electrical measurements. Int J Fatigue. 2006; 28:1028-1036.

[9] Starke P, Walther F, Eifler D. New fatigue life calculation method for quenched and tempered steel SAE 4140. Mater Sci Eng A. 2009; 523:246-252.

[10] Starke P, Bäumchen A, Wu HR. SteBLife – A new short-time procedure for the calculation of S-N curves and failure probabilities. Mater Test. 2018; 60:121-127.

[11] Starke P, Wu HR. Use of non-destructive testing methods in a new one-specimen test strategy for the estimation of fatigue data. Int J Fatigue. 2018; 111:177-185.

[12] Guo SF, Zhou YG, Zhang HX, Yan ZF, Wang WX, Sun K, Li YD. Thermographic analysis of the fatigue heating process for AZ31B magnesium alloy. Mater Design. 2014; 65:1172-1180.

[13] Boulanger T, Chrysochoos A, Mabru C, Galtier A. Calorimetric analysis of dissipative and thermoelastic effects associated with the fatigue behavior of steels. Int J Fatigue. 2004; 26:221-229.

[14] Berthel B, Chrysochoos A, Wattrisse B, Galtier A. Infrared image processing for the calorimetric analysis of fatigue phenomena. Exp Mech. 2008; 48:79-90.

[15] Mareau C, Favier V, Weber B, Galtier A. Influence of the free surface and the mean stress on the heat dissipation in steels under cyclic loading. Int J Fatigue.

2009; 31:1407-1412.

[16] Mareau C, Favier V, Weber B. Micromechanical modeling of the interactions between the microstructure and the dissipative deformation mechanisms in steels under cyclic loading. Int J Plast. 2009; 32:106-120.

[17] Connesson N, Maquin F, Pierron F. Dissipative energy as an indicator of material microstructural evolution. EPJ Web of Conferences 6. 2010; 38013.

[18] Connesson N, Maquin F, Pierron F. Experimental energy balance during the first cycles of cyclically loaded specimens under the conventional yield stress. Exp Mech. 2011; 51:23-44.

[19] Wang XG, Crupi V, Jiang C, Guglielmino E. Quantitative Thermographic Methodology for fatigue life assessment in a multiscale energy dissipation framework, Int J Fatigue. 2015; 81:249-256.

[20] Wang XG, Crupi V, Jiang C, Feng ES, Guglielmino E, Wang CS. Energy-based approach for fatigue life prediction of pure copper. Int J Fatigue. 2017; 104:243-250.

[21] Guo Q, Guo XL, Fan JL, Syed R, Wu CW. An energy method for rapid evaluation of high-cycle fatigue parameters based on intrinsic dissipation. Int J Fatigue. 2015; 80:136-144.

[22] Guo Q, Zaïri F, Guo XL. An intrinsic dissipation model for high-cycle fatigue life prediction, Int J Mech Sci. 2018; 140:163-171.

[23] Poncelet M, Doudard C, Calloch S, Weber B, Hild F. Probabilistic multiscale models and measurements of self-heating under multiaxial high cycle fatigue. J Mech Phys Solids. 2010; 58:578-593.

[24] Knobbe H, Starke P, Hereñú S, Christ HJ, Eifler D. Cyclic deformation behaviour, microstructural evolution and fatigue life of duplex steel AISI 329 LN. Int J Fatigue. 2015; 80:81-89.

[25] Audenino AL, Crupi V, Zanetti EM. Correlation between thermography and internal damping in metals. Int J Fatigue. 2003; 25:343-351.

[26] He C, Tian RH, Liu YJ, Li JK, Wang QY. Ultrasonic fatigue damage behavior of 304L austenitic stainless steel based on micro-plasticity and heat dissipation. J Iron

Steel Res Int. 2015; 22:638-644.

[27] Curà F, Gallinatti AE, Sesana R. Dissipative aspects in thermographic methods. Fatigue Fract Eng M. 2012; 35:1133-1147.

[28] Micone N, Waele W. On the application of infrared thermography and potential drop for the accelerated determination of an S-N curve. Exp Mech. 2017; 57:143-153.

[29] Liu HQ, Wang QY, Huang ZY, Teng ZJ. High-cycle fatigue and thermal dissipation investigations for low carbon steel Q345. Key Eng Mater. 2016; 664:305-313.

[30] He C, Liu YJ, Fang DH, Wang QY. Very high cycle fatigue behavior of bridge steel welded joint. Theor App Mech L. 2012; 2(3):031010.

[31] Huang ZY, Liu HQ, Wang C, Wang QY. Fatigue life dispersion and thermal dissipation investigations for titanium alloy TC17 in very high cycle regime. Fatigue Fract Eng M. 2015; 38:1285-1293.

[32] Thomson W. XV.-On the dynamical theory of, heat, with numerical results deduced from Mr. Joule's equivalent of a thermal unit, and M. Regnault's observations on steam. Transactions of the royal society of Edinburgh. 1853; 20:261-288.

[33] Morabito AE, Chrysochoos A, Dattoma V, Galietti U. Analysis of heat sources accompanying the fatigue of 2024 T3 aluminium alloys. Int J Fatigue. 2007; 29:977-984.

[34] Lemaitre J, Chaboche JL. Mechanics of solid materials. Cambridge University Press. 1994.

[35] Spittel M, Spittel T. Metal Forming data of ferrous alloys-deformation behavior. Steel symbol/number: C45/1.0503. In H. Warlimont (Ed.). Springer-Verlag Berlin Heidelberg. 2009; 210-215.

[36] Guo Q, Guo XL. Research on high-cycle fatigue behavior of FV520B stainless steel based on intrinsic dissipation. Mater Design. 2016; 90:248-255.

[37] Maquin F, Pierron F. Heat dissipation measurements in low stress cyclic loading of metallic materials: From internal friction to micro-plasticity. Mech Mater. 2009; 41:928-942.

Table 1

Chemical compositions of normalized SAE 1045.

(Wt.-%)		C	Si	Mn	P	S	Cr	Mo	Ni
DIN	min.	0.42	-	0.50	-	-	-	-	-
	max.	0.50	0.40	0.80	0.030	0.035	0.40	0.10	0.40
Customer's report		0.47	0.23	0.72	0.012	0.013	0.06	0.014	0.07

Table 2

Material properties of normalized SAE 1045.

Property	Unit	Value	Property	Unit	Value
Ultimate strength	MPa	710	Mass density	kg m^{-3}	7821
Yield strength	MPa	413	Specific heat capacity	J kg^{-1} K^{-1}	474
Poisson's ratio	—	0.3	Heat conduction coefficient	W m^{-1} K^{-1}	48
Young's modulus	GPa	214	Linear thermal expansion coefficient	10^{-6} K^{-1}	11
Brinell hardness	HB	210			

Thermophysical parameters taken from the Ref [31].

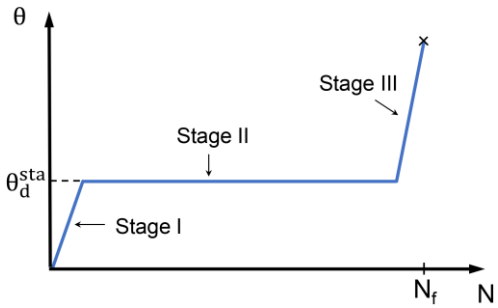

Fig. 1. Schematic representation of the temperature evolution process during a constant amplitude test.

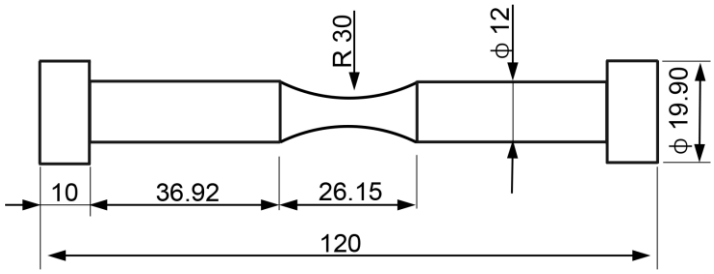

Fig. 2. Shape and dimension (in mm) of specimen.

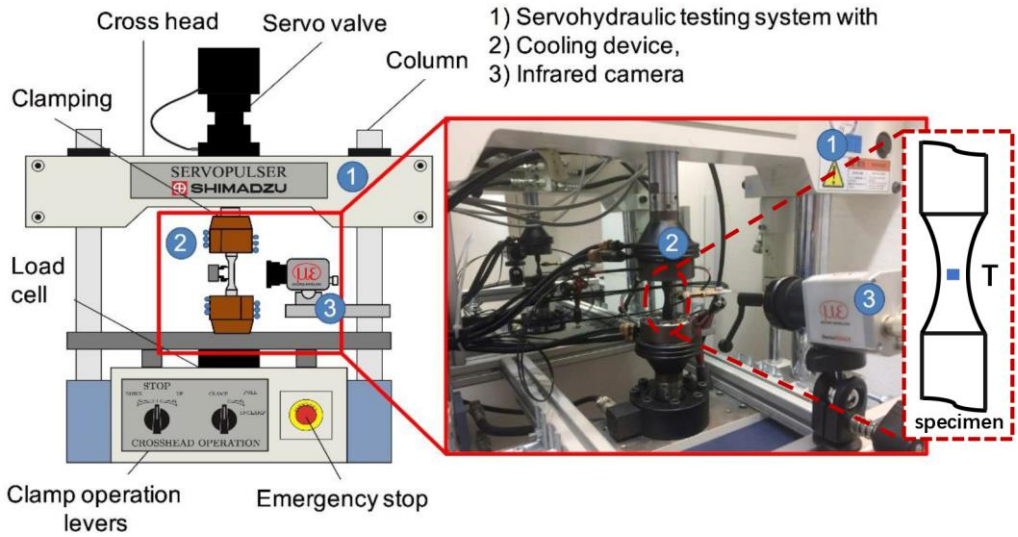

Fig. 3. Experimental setup.

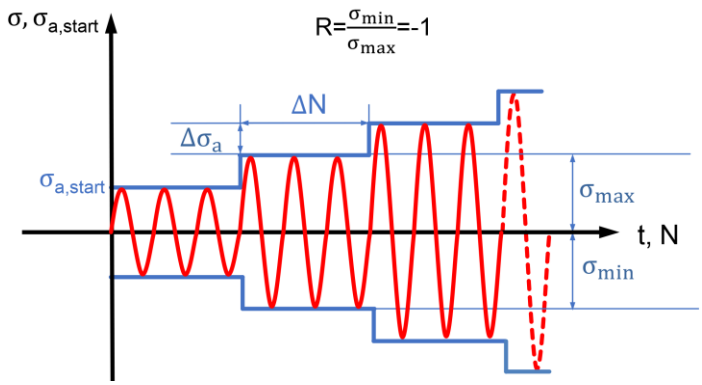

Fig. 4. Schematic diagram of LIT procedure.

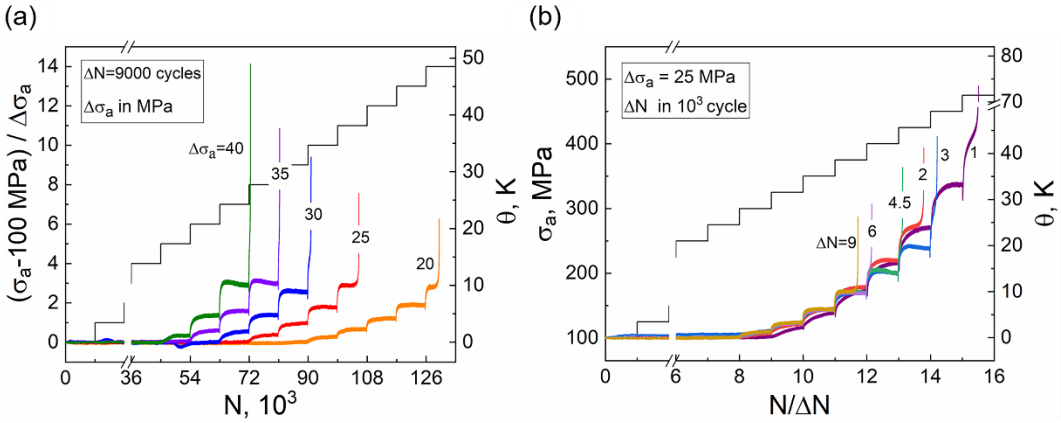

Fig. 5. Change in temperature vs. the number of cycles in load increase tests for (a) constant step lengths (ΔN =9000 cycles) and varying step heights; (b) constant step heights ($\Delta\sigma_a$ =25 MPa) and varying step lengths.

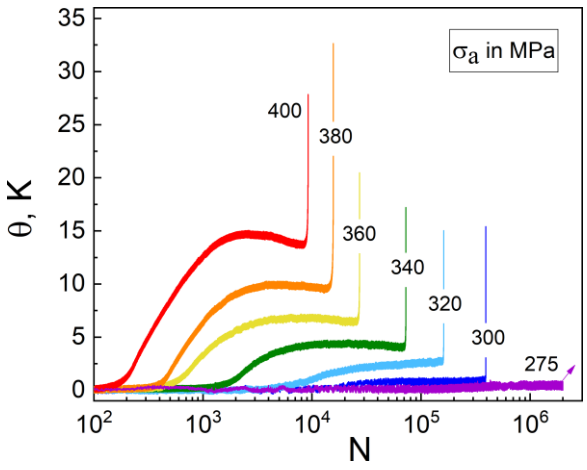

Fig. 6. Change in temperature vs. the number of cycles in constant amplitudes tests.

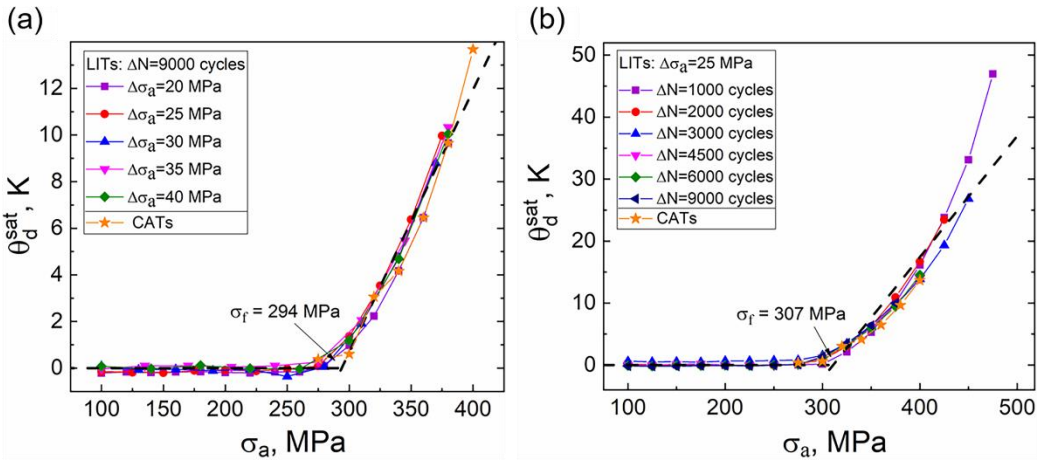

Fig. 7. Change in temperature in the saturated state vs. the stress amplitude in load increase tests for (a) constant step lengths (ΔN =9000 cycles) and varying step heights; (b) constant step heights ($\Delta\sigma_a$ =25 MPa) and varying step lengths.

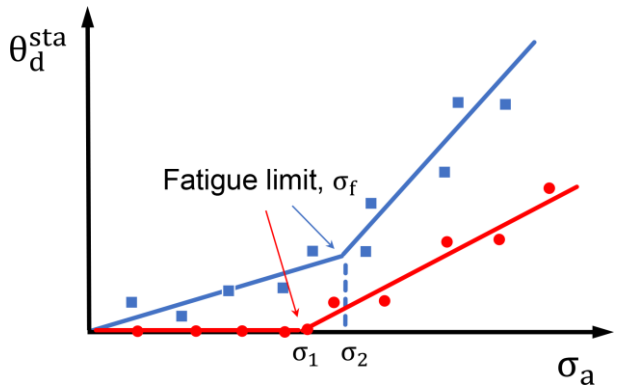

Fig. 8. Schematic illustration of the evaluation of fatigue limit proposed by Luong.

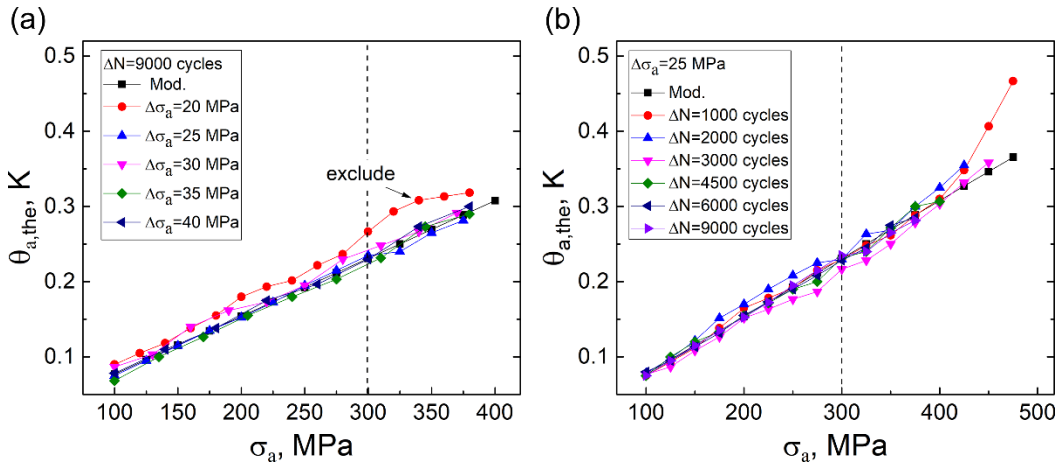

Fig. 9. Thermoelastic relation vs. stress amplitude in load increase tests for (a) constant step lengths (ΔN =9000 cycles) and varying step heights; (b) constant step heights ($\Delta\sigma_a$ =25 MPa) and varying step lengths.

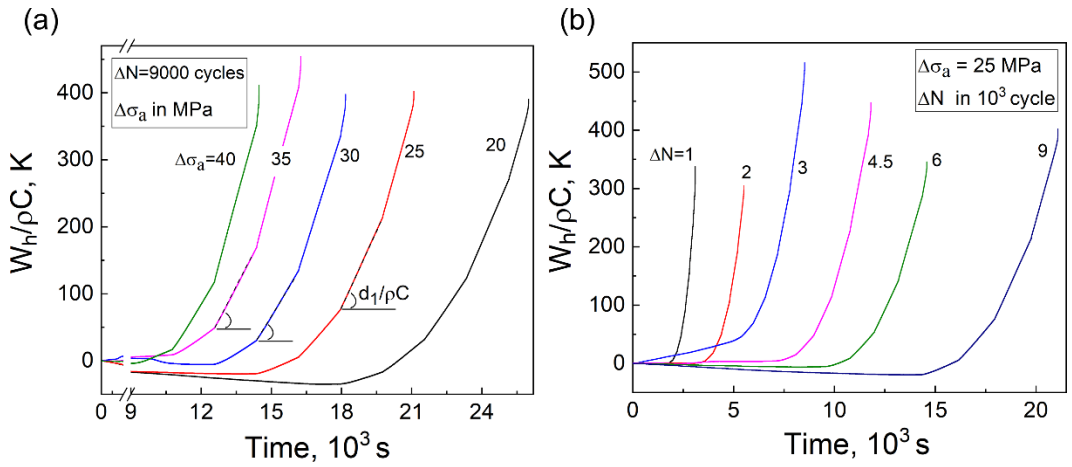

Fig. 10. Equivalent dissipated energy vs. time in load increase tests for (a) constant step lengths ($\Delta N = 9000$ cycles) and varying step heights; (b) constant step heights ($\Delta\sigma_a$ =25 MPa) and varying step lengths.

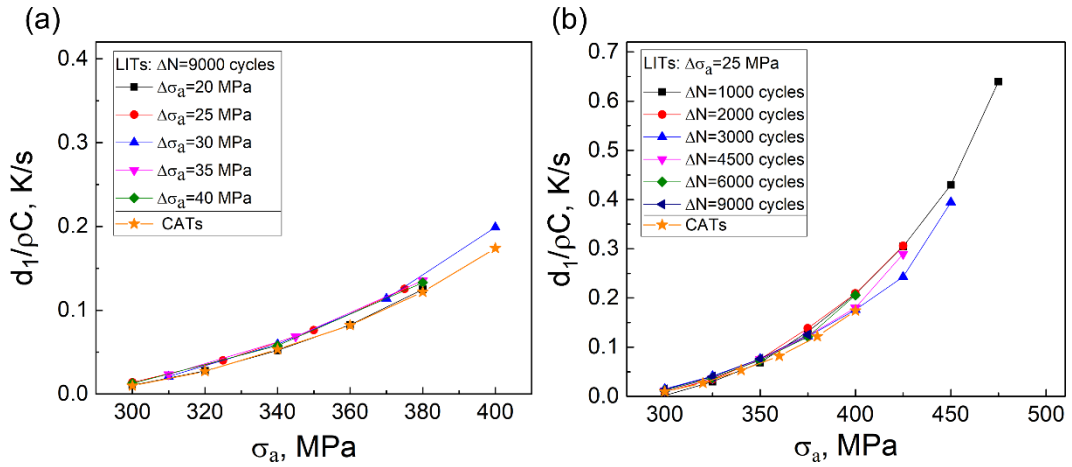

Fig. 11. Equivalent intrinsic dissipation rate vs. stress amplitude in load increase tests for (a) constant step lengths (ΔN =9000 cycles) and varying step heights; (b) constant step heights ($\Delta\sigma_a$ =25 MPa) and varying step lengths.

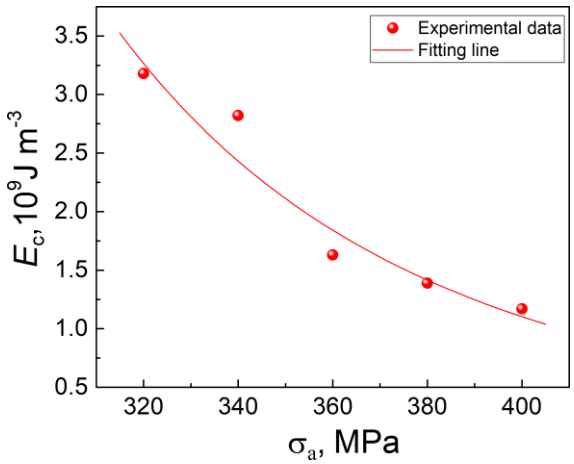

Fig. 12. Total dissipated energy vs. stress amplitude in constant amplitude tests (the total dissipated energy of 300 MPa is excluded as it runs out sometimes[10]).

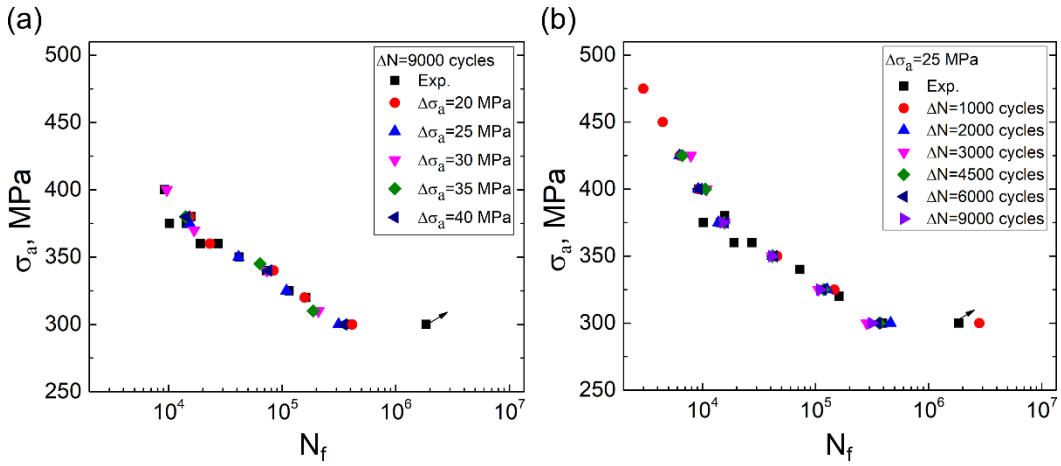

Fig. 13. S-N data obtained by the energy method and traditional fatigue tests (some experimental S-N points taken from literature [10]).

PAPER 2

A unified fatigue life calculation based on intrinsic thermal dissipation and microplasticity evolution

Zhenjie Teng*, Haoran Wu, Christian Boller, Peter Starke

Int J Fatigue, 2020; 131: 105370. DOI: 10.1016/j.ijfatigue.2019.105370

Copyright:

The following part is reproduced with permission from (2019) Elsevier Ltd.

A unified fatigue life calculation based on intrinsic thermal dissipation and microplasticity evolution

Zhenjie Teng [a, b, *], Haoran Wu [a, b], Christian Boller [a], Peter Starke [a, b]

[a] *Chair of Non-Destructive Testing and Quality Assurance, Saarland University, Saarbrücken 66125, Germany*

[b] *Department of Materials Sciences and Materials Testing, University of Applied Sciences Kaiserslautern, Kaiserslautern 67659, Germany*

Abstract

This paper advances a unified approach by evaluating the evolution of the intrinsic thermal dissipation and the microplasticity strain amplitude of SAE1045 steel. The intrinsic dissipation is utilized to understand the fatigue behavior and to link the materials' microstructure evolution directly. The microplasticity strain amplitude is related to a fatigue process and correlated to fatigue life that can be deducted from the change in temperature. With only one load increase test and one constant amplitude test in the present case, an S-N curve can be evaluated being in very good agreement with experimentally determined data obtained the traditional way.

Keywords: Thermography; high-cycle fatigue; intrinsic dissipation; microplasticity; fatigue life evaluation

Nomenclature

b	fatigue strength exponent	$\boldsymbol{\Sigma}$	macro stress tensor (MPa)
c	fatigue ductility exponent	Σ_a	macro stress amplitude (MPa)
C_p	specific heat capacity (J kg^{-1} K^{-1})	Σ_f	macro fatigue strength (MPa)
d_1	intrinsic dissipation term (J m^{-3} s^{-1})	$\Delta\Sigma_a$	stress amplitude increment (MPa)
E_d	dissipated energy (J m^{-3})	$\boldsymbol{\sigma}$	micro stress tensor (MPa)
E_s	stored energy (J m^{-3})	σ_a	micro stress amplitude (MPa)
f	loading frequency (s^{-1})	σ_f'	fatigue strength coefficient (MPa)
k	thermal conductivity (W m^{-1} K^{-1})	$\mathbf{E}$	macro strain tensor
K	Young's modulus (MPa)	$\boldsymbol{\varepsilon}$	micro strain tensor
K'	cyclic strain hardening coefficient (MPa)	$\varepsilon_{a,e}$	micro elastic strain amplitude
n'	cyclic strain hardening exponent	$\varepsilon_{a,p}$	microplastic strain amplitude
N	number of cycles	ε_f'	fatigue ductility coefficient
ΔN	loading step length	$\boldsymbol{\varepsilon_p}$	microplastic strain tensor
N_f	fatigue life	θ	change in temperature (K)
$N_{f,c}$	calculated fatigue life	τ	period of one loading cycle (s)
r_{ext}	external heat source term (J m^{-3})	τ_{eq}	time constant (s)
R	stress ratio	μ	shear modulus (MPa)
S_i	internal coupling source term (J m^{-3})	ρ	mass density (kg m^{-3})
S_{the}	thermoelastic source term (J m^{-3})	ξ	material constant
T	measured temperature (°C)	β	material constant
T_0	equilibrium temperature field (°C)	ν	Possion's ratio
W_p	plastic energy (J m^{-3})		

1. Introduction

From a microscopic point of view, fatigue is the process of progressive, localized, and non-recoverable microstructural developments that can lead to final failure of specimens or structures [1,2]. A typical feature of the microstructural changes during a fatigue process is that a part of the repeated elastic-plastic deformation is dissipated irreversibly as heat. It is widely recognized that loading of metals and resulting fatigue are a process that includes heat dissipation [3-6] and the self-heating regime within the material is closely related to the mechanisms of fatigue damage [7], including effects resulting from microplasticity. The continuous improvement in materials' performance and related structural design requires appropriate characterization where fatigue plays an essential role. Ageing infrastructure is just one example where an increasing number of fatigue related information is required ex post. To obtain such information the traditional way may require tens of tests to be performed. This can cost more than one month in time to get a single S-N curve determined in the case of high cycle fatigue (HCF) including the appropriate levels of data confidence [8]. Alternatives are therefore in need to reduce the experimental duration and effort, which have been developed based on material response to carry out the evaluation of fatigue properties.

A means to retrieve possibly a maximum of a material's response has been realized through the application of non-destructive evaluation techniques, where thermography and its related measurement is one of the techniques being very much sought. The thermal manifestation of materials due to fatigue can be measured by using infrared cameras or thermocouples, going back to the pioneering work of people such as Dengel [9], Chrysochoos [10], or Luong [11], in which the measured thermal parameters have been used to model or predict fatigue properties such as fatigue strength and fatigue life. Most of those approaches are based on the relationship between fatigue damage and the corresponding change in temperature in the macroscopic regime, e.g. One- [12], Two-Curve Method [13], Physically Based Fatigue Life- (PHYBAL) [14], SteBLife- [15], StressLife- [16], StrainLife- evaluation approach [17], and a temperature integral model [18].

The change in temperature due to fatigue loading is not only an intrinsic manifestation of changes in the materials' microstructure but is also influenced by the

heat conduction and convection with the environment. Hence, some new approaches have been developed that regard the dissipated energy as a fatigue damage indicator for a microstructural evolution resulting from plastic deformation at the microscopic scale at some well-oriented micro defects. Boulanger et al. [19] separated mathematically the thermoelastic and dissipative source of the heat generated during fatigue processes of steel with calorimetric analysis. Regarding the dissipation rate as a characteristic fatigue indication, Connesson et al. [20] proposed a data processing method to obtain the heat source generated and to reveal the rapid determination of fatigue strength based on physical response. It is verified that the change of intrinsic dissipation versus applied stress can give an indication of a material's fatigue strength. Guo et al. [21] and Wang et al. [22] established a rapid evaluation model of intrinsic dissipation and determined the S-N curves, respectively.

Considering the main deformation of the material to be the macroscopic elasticity shakedown, it is indicated that fatigue damage occurs at a microscopic scale caused by microplasticity. Doudard et al. [23,24] proposed a probabilistic two-scale model for high cycle fatigue (HCF) that accounts for the failure of specimens. Fan et al. [25] developed a unifying energy approach for rapid assessment of fatigue parameters in the HCF regime and this approach is applicable for the characterization at the macro and micro scale.

The main aim of the work described here is to present a short-term evaluation procedure (STEP) where S-N data has been generated for a SAE1045 steel based on a mathematical and materials' mechanical evaluation procedure considering the intrinsic thermal dissipation and microplasticity evolution, taking advantage of results obtained through non-destructive measurements performed under different loading conditions. The methodology used to bridge the gap of the fatigue behavior between the macroscopic and microscopic regime is introduced (section 2), applied and validated by experimental results (section 3) and finally assessed in the frame of some conclusions drawn (section 4).

2. Methodology

2.1. Intrinsic dissipation

Combining the first and second laws of thermodynamics and neglecting the coupling effect between the microstructure describing internal variables and temperature, Boulanger et al. [19] measured temperature fields of a specimens' surface during fatigue tests and deduced a specific form of heat diffusion to determine the heat source. It is expressed as:

$$\rho C_p \dot{\theta} - \mathrm{div}(k: \mathrm{grad}\theta) = S_{the} + S_i + d_1 + r_{ext} \quad (1)$$

where ρ, C_p and k are the material thermodynamic parameters corresponding to mass density, specific heat capacity, and thermal conductivity. $\theta = T - T_0$ is the change in temperature, where T is the measured temperature and T_0 the equilibrium temperature. S_{the} is the thermoelastic source term, S_i the internal coupling source term, d_1 the intrinsic dissipation term dependent on the microplasticity at the grain scale, and r_{ext} the external heat source term, respectively.

In adiabatic conditions, the dissipated energy rate equals the internal energy accumulation rate, while the internal coupling source term S_i and the external heat source term r_{ext} can be neglected [26]. Subsequently, the local heat diffusion equation can be rewritten as:

$$\rho C_p \left(\frac{\partial \theta}{\partial t} + \frac{\theta}{\tau_{eq}} \right) = d_1 + S_{the} \quad (2)$$

where τ_{eq} denotes a time constant characterizing the heat exchanges between the specimen's surface and the environment, e.g. heat convection and heat radiation. During a HCF test, the thermoelastic source S_{the} vanishes after each loading cycle due to the cyclic load mode, and the temperature variation tends to be asymptotic with $\frac{\partial \theta}{\partial t} = 0$, such that the dissipated energy within an unit time can be simplified as:

$$d_1 = \rho C_p \frac{\theta}{\tau_{eq}} \quad (3)$$

2.2. Microplasticity strain assessment

For HCF tests, the applied cyclic load level can be still less than the macroscopic yield strength and the main deformation of the material is dedicated to macroscopic

elasticity shakedown [25]. However, at the microplastic scale, the inconsistent grain boundaries, localized dislocations and inhomogeneous grain size in the material can incite a high stress concentration, then microplasticity at some isolated grains can therefore already be activated and microstructures permanently be changed with the most intuitive form being heat dissipation.

Lemaitre et al. [27] firstly proposed a two-scale model to study the local damage accumulation at a microscopic scale in a deterministic way. The schematic diagram of the activation scenario of sites is demonstrated in Fig. 1, $\mathbf{\Sigma}$ and $\mathbf{E}$ are the macroscopic stress and strain tensors, $\boldsymbol{\sigma}$ and $\boldsymbol{\varepsilon}$ the microscopic stress and strain tensors, respectively.

Undoubtedly, the higher the stress level is, the larger number of activated sites can be expected, which consequently results in a higher level of dissipated energy. The local fatigue damage accumulation is supposed to be on the microscopic scale and its dimensions are smaller than the volume element associated with a mesoscopic scale. Then the representative volume element can be divided into two phases: A matrix of generally elastically loaded grains, among which the volume accounting for the grains, where local plasticity already occurs is included. It is assumed they have the same elastic behavior and the yield stress of the elasto-plastic inclusion is less than the matrix that still remains in an elastic state.

The relationship between the macroscopic stress tensor to the microscopic stress tensor and plastic strain tensor is deduced by the law of localization and homogenization [23,29]:

$$\boldsymbol{\sigma} = \mathbf{\Sigma} - 2\mu(1-\beta)\boldsymbol{\varepsilon}_{\mathbf{p}} \tag{4}$$

where $\boldsymbol{\sigma}$ is the microscopic stress tensor, $\mathbf{\Sigma}$ the macroscopic stress tensor, $\boldsymbol{\varepsilon}_{\mathbf{p}}$ the microplastic strain tensor, μ the shear modulus, and $\beta = \frac{2(4-5\nu)}{15(1-\nu)}$ a parameter given by Eshelby's analysis of an ellipsoidal inclusion in an elastic strain field [30], where ν denotes Possion's ratio.

2.3. A unified energy approach

Resorting to the energy balance law, it is necessary to establish a relationship between the plastic energy and the dissipated energy. As being well known, the dissipated energy takes the majority of the plastic energy but not the entire. During the loading process of the plastic work, a part of the mechanical energy is stored in the material participating in the microstructure evolution process, being named the stored energy E_s and resulting from micro defects, crystal lattice or dislocation structures. The fraction of plastic energy W_p converting to dissipated energy E_d can be expressed by a factor ξ as follows:

$$\xi = \frac{E_d}{W_p} = \frac{W_p - E_s}{W_p} \tag{5}$$

The energy balance between the plastic work and the dissipated energy can be mathematical described by the Eq. (5).

The hysteresis loop for the stress-strain can be simplified according to [31] in an elliptical form and the plastic work in a load cycle can be estimated as:

$$W_p \approx \pi \sigma_a \varepsilon_{a,p} \tag{6}$$

where σ_a is the microscopic stress amplitude and $\varepsilon_{a,p}$ the microplastic strain amplitude, respectively.

Based on the estimated heat source assessment in the thermal equilibrium stage, the dissipated energy during a loading cycle can be computed through the integration of the intrinsic dissipation d_1:

$$E_d = \int_t^{t+\tau} d_1 \, dt \tag{7}$$

where $\tau = 1/f$ indicates the period of one loading cycle.

Studies have shown that for many metallic materials, the proportion of 80-100% of the plastic work dissipates into the surroundings as heat, leading to an increase in the specimen's temperature [25,32-34], it is commonly assumed ξ as an independent material constant. It is then reasonable to adapt the intermediate value $\xi = 0.9$ simply for the material considered here.

By introducing Eqs. (6) and (7) into Eq. (4), a relationship between the microplasticity strain amplitude $\varepsilon_{a,p}$ and the intrinsic dissipation rate d_1 is derived as:

$$\frac{d_1}{f} = \xi\pi\sigma_a\varepsilon_{a,p} = \xi\pi\left[\Sigma_a - 2\mu(1-\beta)\varepsilon_{a,p}\right]\varepsilon_{a,p} \tag{8}$$

Solving Eq. (8), the microplasticity strain amplitude can be obtained:

$$\varepsilon_{a,p} = \frac{\Sigma_a}{4\mu(1-\beta)} - \sqrt{\left[\frac{\Sigma_a}{4\mu(1-\beta)}\right]^2 - \frac{d_1}{2\mu f\xi\pi(1-\beta)}} \tag{9}$$

By using the intrinsic thermal dissipation methodology, Eq. (9) presents a meaningful method to evaluate the macro- and micro fatigue behavior of a material and improve the theoretical background of fatigue in terms of thermographic measurements in view of fatigue life evaluation which is discussed in the following sections.

3. Experimental details

3.1. Material

The material studied here is an unalloyed medium carbon steel, SAE1045 (German DIN-standard: C45E) which is widely used in mechanical engineering and whose chemical composition analysis is compared to the DIN EN 10083-1 standard in Table 1. The material consists of a mostly ferritic-pearlitic microstructure with an ultimate strength of 710 MPa and a yield strength of 413 MPa. The main mechanical and thermophysical properties are summarized in Table 2.

3.2. Experimental setup

The experimental setup included a servo-hydraulic fatigue test system (Shimadzu EHF-L) with a 20/25 kN cyclic/quasi-static load capacity and an infrared imaging system (Micro-Epsilon thermoIMAGER TIM 450), as shown in Fig. 2. The fatigue tests were run at a stress ratio of R = -1 and a loading frequency of 5 Hz. Temperature measurement areas (10×10 pixels) defined on the specimens' surface were recorded by using the IR camera with a resolution of 382×288 pixels in the full window mode and a thermal sensitivity of 0.04 K at room temperature. In order to have a stable temperature condition and avoid heat conduction from the upper and lower clamps of

the servo-hydraulic circuit, a Peltier-element cooled water-circuit was used to continuously stabilize the temperature of the clamps, i.e. both ends of the mounted specimen.

To ensure a high and uniform thermal emissivity, the surface of the specimens were painted by a thin layer of matt black paint (emission factor 0.97). The geometric details of the test specimen are shown in Fig. 3. The specimens were manufactured from round bar steel with a diameter of 20 mm and machined to a scaly surface because of heat treatment.

3.3. Fatigue tests

The uniaxial fatigue tests were carried out at room temperature in a load control mode with a sinusoidal waveform. The applied stress as a result of the 5 Hz loading frequency can be expressed as $\Sigma(t) = \Sigma_a \sin(10\pi t)$. Two kinds of fatigue tests were performed, a load increase test (LIT) and a constant stress amplitude test (CAT) with details of the loading block sequences being as follows:

Test I: LITs were conducted to identify the intrinsic dissipation model parameters. All the tests started with a constant stress amplitude of $\Sigma_{a,start} =$ 100 MPa. Each time when a fixed loading step length of ΔN cycles was reached, the stress amplitude has been increased by an increment $\Delta\Sigma_a$. Such load increase has been repeated until specimen failure. Several LITs were conducted in this paper with two variations as shown in Fig. 4: (i) ΔN has been kept constant at 9000 cycles, but $\Delta\Sigma_a$ has been varied (20, 25, 30, 35, 40 MPa) from test to test. (ii) $\Delta\Sigma_a$ has been kept constant at 25 MPa but ΔN has been varied (1000, 2000, 3000, 4500, 6000 cycles).

Test II: Conventional stress-controlled constant amplitude tests were carried out at $\Sigma_a =$ 360 MPa to determine the fatigue ductility coefficient ε_f'.

Eleven specimens were used for the tests in total and each test only conducted with an unloaded specimen from the origin state. To get enough data points for avoiding aliasing but not to overflow the measurement PC system by a too high data rate, the recording frequency of the infrared camera was set to 100 Hz. Environmental noise

effects were minimized by using an averaging function within the same temperature measurement area during recording and further smoothing of the data.

4. Results and discussion

4.1. Results of the macro fatigue parameters

Fig. 4 graphically shows the evolution of the change in temperature θ of Test I with the LITs under the different load increase parameters considered. As for the temperature-based characterization of the cyclic deformation behavior of the LITs, predominantly in the elastic region, the mean value of the change in temperature only oscillates around 0 K in the first loading steps. This is due to the thermoelastic effect, causing nearly no increase in the $\theta - N$ curve. However, above a certain stress amplitude value, predominantly within the elastic-plastic deformation region, the θ value increases constantly at each loading step level. Carefully observing this development within a single loading step allows two different phases to be distinguished: an initial temperature increase phase and a subsequent temperature stabilization phase. In the last step of each test, a sudden temperature increase phase occurs shortly before the specimen reaches the final fracture.

Fig. 5 presents the evolution of the intrinsic dissipation rate on the subsequent macroscopic stress amplitude levels of the same LIT with $\Delta\Sigma_a = 25$ MPa and $\Delta N = 2000$ cycles. Generally speaking, under a non-adiabatic test condition, at different stress amplitudes the intrinsic dissipation rate d_1 is not staying constant. Instead, the higher the stress amplitude, the higher the intrinsic dissipation rate becomes. From Figs. 4 and 5 it becomes obvious that both the change in temperature and the dissipated energy rate show a similar equilibrium behavior, whereas a relatively constant value can be obtained when the heat generation rate inside the material is supposed to be equal to the heat exchange with the surroundings.

Fig. 6 shows the variations of dissipated energy rate for each sucessive stress amplitude level and the loading parameters of the different LITs, where the values of d_1 were extracted at half of the number of cycles ΔN of each load step. The higher stress amplitudes yield a higher intrinsic dissipation rate. With the increasing stress level, the dissipated energy increases continually being caused by the progressive

evolution of the microstructure, e.g. sliding, tangling, multiplication and pile-up of the dislocations, creation of (persistent) slip bands, and even the predominant deformation of the specimen with a macro-elastic shakedown.

A clear transition from a constant to an increasing behaviour can be seen from Figs. 4 and 6 where both ΔT and d_1 start to increase significantly from a constant value around zero while the stress amplitude keeps rising. This inflection point, which represents the onset of microplasticity, connects the so-called fatigue strength with the finite fatigue life regime. Thus, the fatigue strength of a material could be evaluated at the corresponding stress amplitude level Σ_a being around 300 MPa in the present case, representing also the yield stress at microscopic level of an elasto-plastic inclusion. In general, when the macroscopic stress is lower than such a value being called here Σ_f, it can be supposed that there is not enough fatigue damage which can lead to a failure in the material. Since the energy dissipation takes place in some isolated grains at the microscopic scale and results in the consecutive fatigue damage accumulation [36,37], there should be also no energy dissipation below the fatigue strength, which explains the extremely low value of d_1 below 300 MPa for the SAE1045 material used here.

In order to investigate the underlying physical mechanisms of the macro fatigue strength, Granato-Lucke dislocation model [38] and Frank-Read dislocation multiplication theory [39] will be introduced to revel to the macroscopic phenomenon of energy dissipation due to the material microstructure motion [21]. It is assumed that within the material, there are lots of micro defects, e.g., dislocation lines, inclusions, and vacancies, etc. Normally, the motions of the micro defects are fixed by pinning points in the crystal lattice when the material subjected to a certain stress amplitude. If this applied stress amplitude is below the fatigue strength, the motions of the micro defects are reversible due to the strong pinning effect makes an important influence in the adjacent crystals [11,25,40,41]. This motion is regarded as non-plastic effect accompanied with very few energy dissipation, like internal damping and anelasticity [42]. There is no fatigue damage accumulation in the reversible micro mechanism during this period. For the stress amplitude above the fatigue strength, the micro defects will break through the strong pins, and then generate new micro defects, such as dislocation sources [21]. The dislocations multiplication accompanies with permanent dislocation motion and rearrangement in some isolated crystals, this irreversible

microstructure motion will lead to permanent strain, namely, microplastic deformation [43], and this irreversible process will have continuous release of energy dissipation. As stated above, the energy dissipation of the reversible micro mechanism is negligible, while the irreversible part is strongly related to microplastic deformation. Thus, the macroscopic fatigue strength can be regarded as the yield stress of micro defects. From the perspective of physics, the variations of change in temperature are acceptable to evaluate the macro manifestation of energy dissipation.

4.2. Results of microplasticity

Morrow [44] proposed a formulation of a power law to express the stress-strain correlation at the macroscopic scale. Herein, we assume that it is also applicable in the microscopic scale and is expressed as:

$$\sigma_a = K' {\varepsilon_{a,p}}^{n'} \tag{10}$$

where K' is the cyclic strain hardening coefficient, n' the cyclic strain hardening exponent, σ_a the stress amplitude and $\varepsilon_{a,p}$ the plastic strain. In general, this relationship being based on a calorimetric method can be used for any kind of metallic material and can provide a potential value of the plastic strain response of materials, especially in the case of micro-strain [34]. Fig. 7a provides the relationship between $\varepsilon_{a,p}$ and σ_a for the LITs at each loading step level. As the $\varepsilon_{a,p}$ fits very consistent with σ_a of each LIT, drawing a Morrow line through these results being plotted in a logarithmic scale leads to the result shown in Fig. 7b and the parameters being K' =1104.5 MPa and n' =0.1174.

The Manson-Coffin law is expressed according to Eq. (11) where in the case here the microplasticity stain amplitude $\varepsilon_{a,p}$ and the fatigue life N_f are related as:

$$\varepsilon_{a,p} = \varepsilon_f' (2N_f)^c \tag{11}$$

and ε_f' is the fatigue ductility coefficient and c the fatigue ductility exponent, respectively.

Another formula being widely used to describe the relationship between stress amplitude and fatigue life is the Basquin equation expressed as:

$$\sigma_a = \sigma_f'(2N_f)^b \tag{12}$$

where σ_f' is fatigue strength coefficient and b is the fatigue strength exponent.

Using exponent n' in the Morrow formulation the exponents of the Manson-Coffin and Basquin equations can be calculated as follows [44]:

$$c = \frac{-1}{5n'+1} \tag{13}$$

$$b = \frac{-n'}{5n'+1} \tag{14}$$

with c = -0.63, b = -0.074 being the numbers determined in the present case. Herein, the parameter c is used for fatigue life calculation and b is for validating this relationship.

4.3. Results of constant amplitude fatigue life evaluation

Based on the above work, the microplasticity strain amplitude $\varepsilon_{a,p}$ can be evaluated by Eq. (9) and the fatigue ductility exponent c by Eq. (13) with the unknown fatigue ductility coefficient ε_f' in the Manson-Coffin law mainly to be obtained through the respective fatigue life and plastic strain amplitude measured from the CAT. Since the plastic strain can be related to the dissipated thermal energy, which has been specifically expressed by Eq. (9), observations can be further related to temperature measurements. Fig. 8 shows the evolution of change in temperature for a CAT with a macro-stress amplitude of Σ_a = 360 MPa. The number of cycles to failure for the specimen is N_f = 2.7×10^4 cycles. The temperature evolution process is in accordance with a typical three-stage-behavior including an initial temperature increase stage, a temperature stabilization stage, and a stage of a sharp temperature increase before fracture. The thermographs present the temperature evolution corresponding to the initial measuring sequence.

The microplasticity strain amplitude $\varepsilon_{a,p}$ of the constant stress amplitude Σ_a = 360 MPa in the stabilized stage was determined with the same method as for the LITs by using Eq. (9). As the three parameters, $\varepsilon_{a,p}$, N_f, and c, have already been known the fatigue ductility coefficient of this SAE1045 steel determined through Eq. (11) turned out to be ε_f' = 0.0586. When taking the other CATs performed into consideration [45], ε_f' shows a similar value when compared to that of 360 MPa, being 0.0581 for 380

MPa and 0.0591 for 400 MPa, respectively.

It is generally acknowledged that the plasticity at microscopic scale associated with the irreversible cyclic slip and the microplasticity strain amplitude at this scale is regarded as a more intrinsic fatigue indicator than the stress amplitude and it is preferred to be related with the fatigue life. The Manson-Coffin law is usually used to express the relationship between this stress and strain, which is formulated through Eq. (11). This law is conventionally used in the low cycle fatigue (LCF) regime, but its applicability has also been extended into the HCF regime [34], which is a justification that this also holds at microscopic scales. The constant amplitude fatigue life of the SAE1045 steel considered here can be evaluated considering the microplasticity strain amplitude determined through Eq. (11) and evaluating the respective fatigue life as follows:

$$N_{f,c} = \frac{1}{2}\left(\frac{\varepsilon_{a,p}}{\varepsilon_f'}\right)^{c^{-1}} \tag{15}$$

where $N_{f,c}$ is the number of applicable load cycles.

The results of the evaluated constant amplitude fatigue lives based on the intrinsic thermal dissipation are shown in Fig. 9. Those are compared to experimental results obtained the conventional way (red dots) where data have been taken from [46]. A good agreement between the evaluated and the validated data can be observed.

The whole microplasticity strain amplitudes taken from the LITs are in coincidence with the curve which is given in Fig. 7b, and here it is assumed that this mathematical formula can even be used for each one LIT in short. With this an S-N curve determined on the basis of the STEP proposed here with temperature being the parameter to be monitored and considered as a basis, only two fatigue experiments are required, one for the LIT and the other for the CAT. This is a huge enhancement in determining a material's S-N curve in terms of time and cost required when compared to the traditional way of S-N curve determination where a reduction factor of 15 in time and cost looks to be realistic.

4.4. Validation of the STEP approach

In the HCF regime the predominant behavior in a material is an elastic shakedown,

but at a microscopic scale the microplasticity strain is an essential indicator for the primary mechanism of the HCF damage accumulation [25,37]. Fig. 10 shows the linear relationship between the microplasticity strain amplitude $\varepsilon_{a,p}$ and the constant amplitude fatigue life $N_{f,c}$ evaluated plotted in a bi-logarithmic scale. The regression for the function based on Eq. (11) has been determined by the method of least squares.

It can be assumed that the elastic behavior at the microscopic scale follows Hooke's law in the HCF regime, hence an equivalent micro-elasticity strain amplitude is determined as:

$$\varepsilon_{a,e} = \frac{\sigma_a}{K} \tag{16}$$

where K is Young's modulus and σ_a the stress amplitude applied. The Basquin equation (Eq. 12) can then be rewritten as:

$$\varepsilon_{a,e} = \frac{\sigma'_f}{K}\left(2N_{f,c}\right)^b \tag{17}$$

Finally, the relationship between micro-elasticity strain amplitude $\varepsilon_{a,e}$ and the evaluated constant amplitude fatigue life is shown in Fig. 11 in a bi-logarithmic scale. The regression line has again been determined by the method of least squares. The value of fatigue strength exponent b has been fitted to -0.071 being very close to the value of -0.074 determined from Eq. (14). As a result, the accuracy and feasibility of the STEP for the calculated fatigue life are illustrated.

5. Conclusions

Temperature is a parameter that can be used to monitor the fatigue related damaging behavior in a metallic material. It can be correlated to the plastic strain. This plastic strain does not need to be apparent at macroscopic scale but can rather be observed at microscopic level resulting from inhomogeneities between grains and hence strain concentrations at microscopic scale. Those strains having been considered here as microplasticity strains can be considered in the HCF regime of metals as the incubators of fatigue damage and can be clearly measured as the material's intrinsic behavior by thermography provided the resulting temperature inducing effects can be clearly separated from other thermal effects generated through environment.

Short term evaluation procedures (STEP) are an elegant way to determine S-N curves at 5 to 10% of an effort when compared to the traditional way. This is specifically true when considering temperature as the parameter to be monitored and the various constitutive relationships provided by people such as Morrow, Manson-Coffin or Basquin. Just two experiments on un-notched specimens, a LIT and a CAT, are required to determine a complete S-N curve including the LCF and the HCF regime as well as the so-called fatigue limit.

An interesting observation has been made that the input parameters of the LIT being the step size of load increase $\Delta\sigma_a$ or the number of cycles ΔN at each load level is rather insensitive in terms of the parameters describing the constitutive behavior of the material considered, would it be the stress-strain relationship or the fatigue life behavior respectively. An important criterion in that regard is certainly that the material's fatigue behavior at each load level, that must have stabilized on the one hand and a sufficient number of representative load levels that must have to be examined on the other.

The approach presented here has been demonstrated for the very popular carbon steel SAE1045 for which plasticity is clearly measurable at various scales. However, validation on other types of steels may be useful to demonstrate the generality of the approach in the longer term.

Acknowledgments

The work has been financially supported by the German Research Foundation (Deutsche Forschungsgemeinschaft DFG under contract STA 1133/6-1) and the China Scholarship Council.

References

[1] Wang XG, Crupi V, Jiang C, Guglielmino E. Quantitative thermographic methodology for fatigue life assessment in a multiscale energy dissipation framework. Int J Fatigue. 2015; 81:249-256.

[2] Liu HQ, Wang HM, Zhang Z, Liu YJ, Huang ZY, Wang QY, Chen Q. Tensile and fatigue behavior of electron beam welded TC17 titanium alloy joint. Int J Fatigue. 2019; 128:105210.

[3] Torabian N, Favier V, Ziaeirad S, Dirrenberger J, Adamski F. Thermal response of DP600 dual-phase steel under ultrasonic fatigue loading. Mater Sci Eng A. 2016; 677:97-105.

[4] Meneghetti G, Ricotta M, Pitarresi G. Infrared thermography-based evaluation of the elastic-plastic J-integral to correlate fatigue crack growth data of a stainless steel. Int J Fatigue. 2019; 125:149-160.

[5] Liu HQ, Wang QY, Huang ZY, Teng ZJ. High-cycle fatigue and thermal dissipation investigations for low carbon steel Q345. Key Eng Mater. 2016; 664:305-313.

[6] He C, Liu YJ, Fang DH, Wang QY. Very high cycle fatigue behavior of bridge steel welded joint. Theor App Mech L. 2012; 2(3):031010.

[7] Mareau C, Favier V, Weber B, Galtier A. Influence of the free surface and the mean stress on the heat dissipation in steels under cyclic loading. Int J Fatigue. 2009; 31(8):1407-1412.

[8] Poncelet M, Doudard C, Calloch S, Hild F. Probabilistic multiscale models and measurements of self-heating under multiaxial high cycle fatigue. J Mech Phys Solids. 2010; 58(4):578-593.

[9] Dengel D. Harig H. Estimation of the fatigue limit by progressively-increasing load tests. Fatigue Eng Mater Struct. 1980; 3:113-128.

[10] Chrysochoos A, Maisonneuve O, Martin G, Caumon H, Chezeaux JC. Plastic and dissipated work and stored energy. Nucl Eng Des. 1989; 114(3):323-333.

[11] Luong MP. Infrared thermovision of damage processes in concrete and rock. Eng Fract Mech. 1990; 35(1-3):127-135.

[12] La Rosa G, Risitano A. Thermographic methodology for rapid determination of the fatigue limit of materials and mechanical components. Int J Fatigue. 2000; 22:65-73.

[13] Luong MP. Fatigue limit evaluation of metals using an infrared thermographic technique. Mech Mater. 1998; 28:155-163.

[14] Starke P, Walther F, Eifler D. PHYBAL – A new method for lifetime prediction based on strain, temperature and electrical measurements. Int J Fatigue. 2006;

28(9):1028-1036.

[15] Wu HR, Bäumchen A, Engel A, Acosta R, Boller C, Starke P. SteBLife – A new short-time procedure for the evaluation of fatigue data. Int J Fatigue. 2019; 124:82-88.

[16] Starke P. StressLifetc – NDT-related assessment of the fatigue life of metallic materials. Mater Test. 2019; 61(4):297-303.

[17] Heckmann K, Sievers J, Schopf T, Schuler X, Acosta R, Starke P, Boller C, Jamrozy M, Knyazeve, Walther F. StrainLife: Efficient fatigue life data generation for an enhanced ageing assessment of metallic components. ASME 2018 Pressure Vessels and Piping Conference, V06BT06A073.

[18] Fargione G, Geraci A, Rosa GL, Risitano A. Rapid determination of the fatigue curve by the thermographic method. Int J Fatigue. 2002; 24(1):11-19.

[19] Boulanger T, Chrysochoos A, Mabru C, Galtier A. Calorimetric analysis of dissipative and thermoelastic effects associated with the fatigue behavior of steels. Int J Fatigue. 2004; 26(3):221-229.

[20] Connesson N, Maquin F, Pierron F. Dissipated energy measurements as a marker of microstructural evolution: 316L and DP600. Acta Mater. 2011; 59(10):4100-4115.

[21] Guo Q, Guo XL, Fan JL, Syed R, Wu CW. An energy method for rapid evaluation of high-cycle fatigue parameters based on intrinsic dissipation. Int J Fatigue. 2015; 80:136-144.

[22] Wang XG, Crupi V, Jiang C, Feng ES, Guglielmino E, Wang CS. Energy-based approach for fatigue life prediction of pure copper. Int J Fatigue. 2017; 104:243-250.

[23] Doudard C, Calloch S, Cugy P, Galtier A, Hild F. A probabilistic two-scale model for high-cycle fatigue life predictions. Fatigue Fract Eng Mater Struct. 2005; 28:279-288.

[24] Ezanno A, Doudard C, Calloch S, Heuzé JL. A new approach to characterizing and modeling the high cycle fatigue properties of cast materials based on self-heating measurements under cyclic loadings. Int J Fatigue. 2013; 47:232-243.

[25] Fan JL, Zhao YG, Guo XL. A unifying energy approach for high cycle fatigue behavior evaluation. Mech Mater. 2018; 120:15-25.

[26] Crupi V. A unifying approach to assess the structural strength. Int J Fatigue. 2008; 30(7):1150-1159.

[27] Lemaitre J, Sermage JP, Desmorat R. A two scale damage concept applied to fatigue. Int J Fract. 1999; 97:67-81.

[28] Munier R, Doudard C, Calloch S, Weber B. Determination of high cycle fatigue properties of a wide range of steel sheet grades from self-heating measurements. Int J Fatigue. 2004; 63:46-61.

[29] Berveiller M, Zaoui A. An extension of the self-consistent scheme to plastically flowing polycrystals. J Mech Phys Solids. 1978; 26(5-6):325-344.

[30] Eshelby JD. The Determination of the Elastic Field of an Ellipsoidal Inclusion, and Related Problems. Proc Roy Soc London A. 1957; 241(1226):376-396.

[31] Papakyriacou M, Mayer H, Plenk Jr H, Stanzl-Tschegg S. Cyclic plastic deformation of tantalum and niobium at very high numbers of cycles. Mater Sci Eng A. 2002; 325(1-2):520-524.

[32] Rosakis P, Rosakis AJ, Ravichandran G, et al. A thermodynamic internal variable model for the partition of plastic work into heat and stored energy in metals. J Mech Phys Solids. 2000; 48(3):581-607.

[33] Eifler D, Piotrowski A. Bewertung zyklischer Verformungsvorgange metallischer Werkstoffe mit Hilfe mechanischer, thermometrischer und elektrischer Messverfahren. Mat-Wiss U Werkstofftech. 1995; 26:121–127.

[34] Wang XG, Feng ES, Jiang C. A microplasticity evaluation method in very high cycle fatigue. Int J Fatigue. 2017; 94:6-15.

[35] Spittel M, Spittel T. Metal Forming data of ferrous alloys-deformation behavior. Steel symbol/number: C45/1.0503. In H. Warlimont (Ed.). Springer-Verlag Berlin Heidelberg. 2009; 210-215.

[36] Curà F, Gallinatti AE, Sesana R. Dissipative aspects in thermographic methods. Fatigue Fract Eng Mater Struct. 2012; 3:1133-1147.

[37] Fan JL, Guo XL, Zhao YG. An energetic method to evaluate the macro and micro high-cycle fatigue behavior of the aluminum alloy. J Mech Eng Sci. 2017; 232(8):1456-1469.

[38] Granato A, Lucke K. Application of dislocation theory to internal friction phenomena at high frequencies. J Appl Phys. 1956; 27:789-805.

[39] Frank F, Read W. Multiplication processes for slow moving dislocations. Phys Rev. 1950; 79:722-723.

[40] Crupi V, Epasto G, Guglielmino E, Risitano E. Analysis of temperature and fracture surface of AISI4140 steel in very high cycle fatigue regime. Theor Appl Fract Mech. 2015; 80:22-30.

[41] Fan JL, Guo XL, Wu CW. A new application of the infrared thermography for fatigue evaluation and damage assessment. Int J Fatigue. 2012; 44:1-7.

[42] Audenino A, Crupi V, Zanetti EM. Correlation between thermography and internal damping in metals. Int J Fatigue. 2003; 25:343-351.

[43] Fan GD, Zheng MY, Hu XS, Xu C, Wu K, Golovin IS. Improved mechanical property and internal friction of pure Mg processed by ECAP. Mater Sci Eng A. 2012; 556:588-594.

[44] Morrow JD. Cyclic plastic strain energy and fatigue of metals. In: Internal friction, damping, and cyclic plasticity. ASTM STP. 378 1965; 45-87.

[45] Teng ZJ, Wu HR, Boller C, Starke P. Thermography in high cycle fatigue short-term evaluation procedures applied to a medium carbon steel. Fatigue Fract Eng Mater Struct. 2019; 43:515-526.

[46] Starke P, Bäumchen A, Wu H. SteBLife – A new short-time procedure for the calculation of S-N curves and failure probabilities. Mater test. 2018; 60(2):121-127.

Table 1

Chemical compositions of normalized SAE 1045 [45].

(Wt.-%)		C	Si	Mn	P	S	Cr	Mo	Ni
DIN	min.	0.42	-	0.50	-	-	-	-	-
	max.	0.50	0.40	0.80	0.030	0.035	0.40	0.10	0.40
Customer's report		0.47	0.23	0.72	0.012	0.013	0.06	0.014	0.07

Table 2

Material properties of normalized SAE 1045 [45].

Property	Unit	Value	Property	Unit	Value
Ultimate strength	MPa	710	Mass density	kg m^{-3}	7821
Yield strength	MPa	413	Specific heat capacity	J kg^{-1} K^{-1}	474
Poisson's ratio	—	0.3	Heat conduction coefficient	W m^{-1} K^{-1}	48
Young's modulus	GPa	214	Linear thermal expansion coefficient	10^{-6} K^{-1}	11
Brinell hardness	HB	210			

Thermophysical parameters taken from the Ref [31].

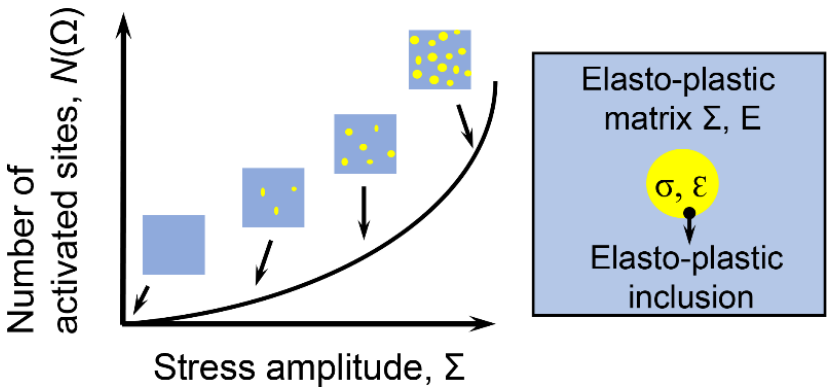

Fig. 1. Schematic representation of the activation scenario of microplastic sites within an elasto-plastic matrix [28].

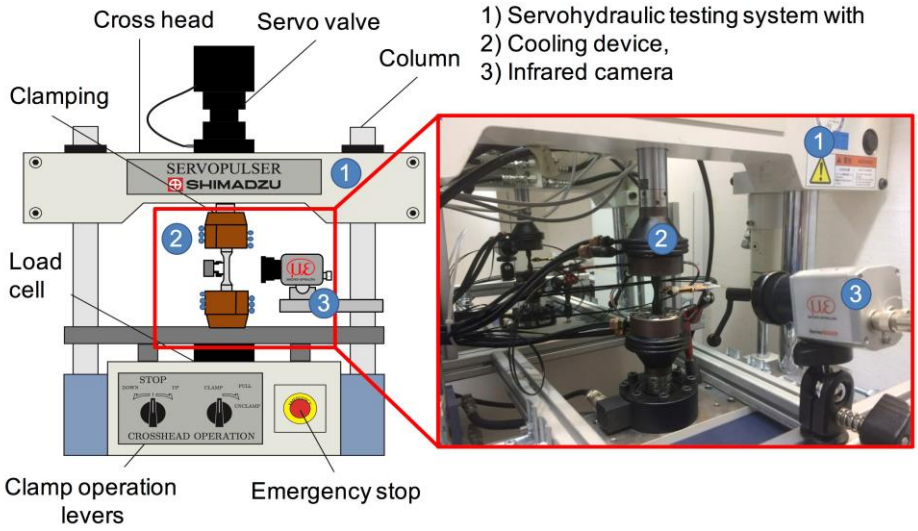

Fig. 2. Experimental setup of hydraulic servo fatigue test and thermographic measurement [45].

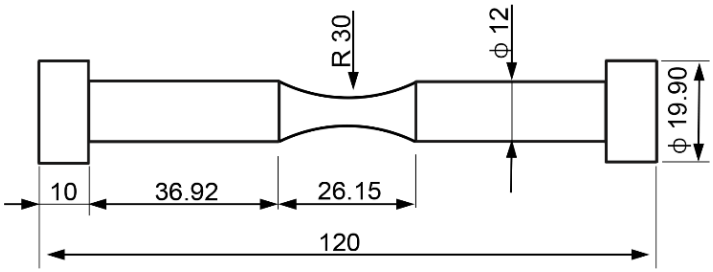

Fig. 3. Shape of fatigue specimen (dimensions in mm) [45].

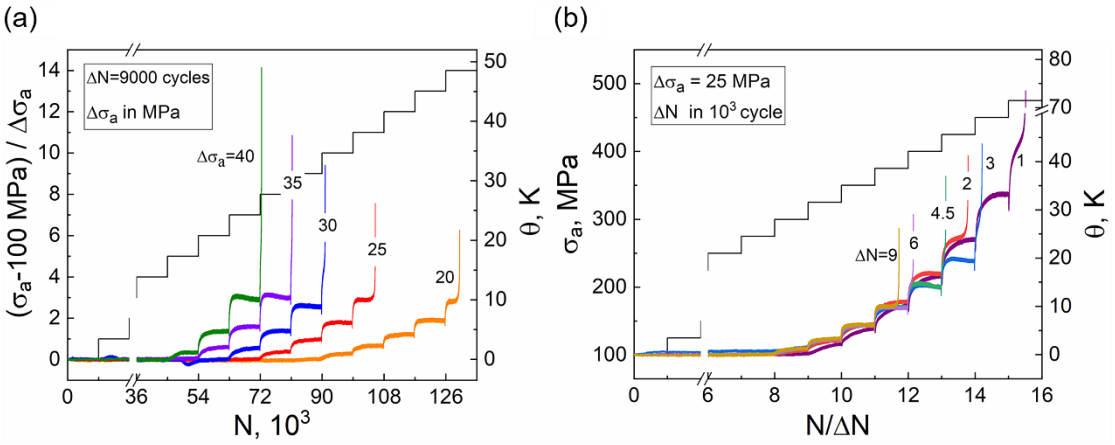

Fig. 4. Change in temperature θ and stress amplitude Σ_a versus number of cycles of different experiments from Test I: (a) LITs with different load increments at constant loading step length; (b) LITs with different step lengths but constant load increments.

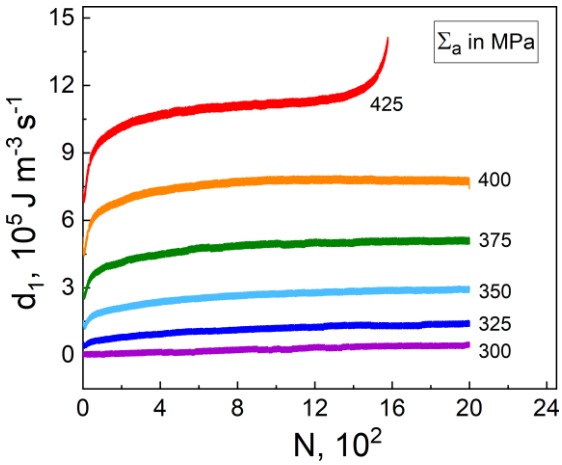

Fig. 5. An example of the evolution of the intrinsic energy dissipation rate at different macro-stress amplitude levels of the same LIT: $\Delta\Sigma_a = 25$ MPa and $\Delta N = 2000$ cycles in its plastic regime.

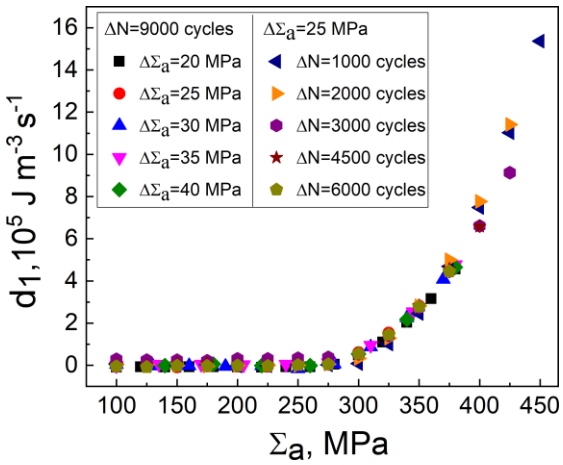

Fig. 6. The intrinsic dissipation rate d_1 at diffident macro-stress amplitudes $\Delta\Sigma_a$ of LITs.

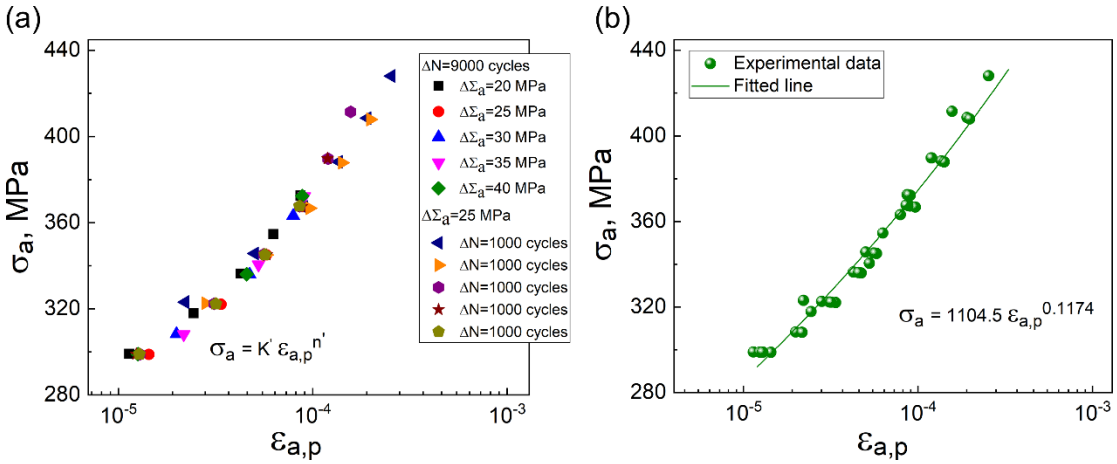

Fig. 7. (a) Plastic strain amplitude $\varepsilon_{a,p}$ versus stress amplitude σ_a at microscopic level; (b) Fitted line in accordance to Morrow formulation of data shown in (a).

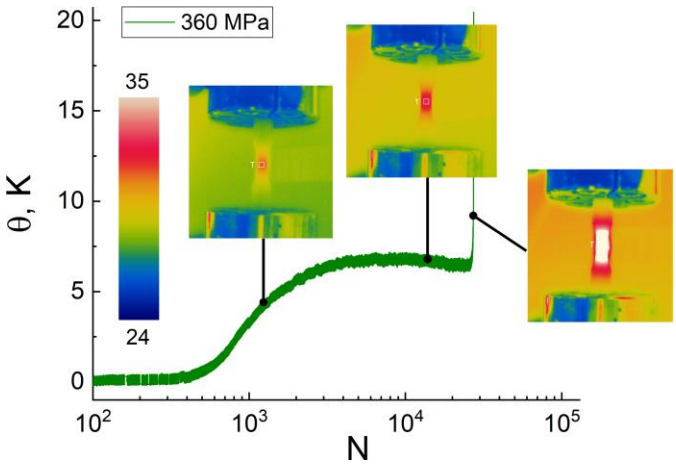

Fig. 8. Temperature evolution on the specimen's surface at stress amplitude $\Sigma_a = 360$ MPa and corresponding thermographs at 5, 50, and 100% of fatigue life.

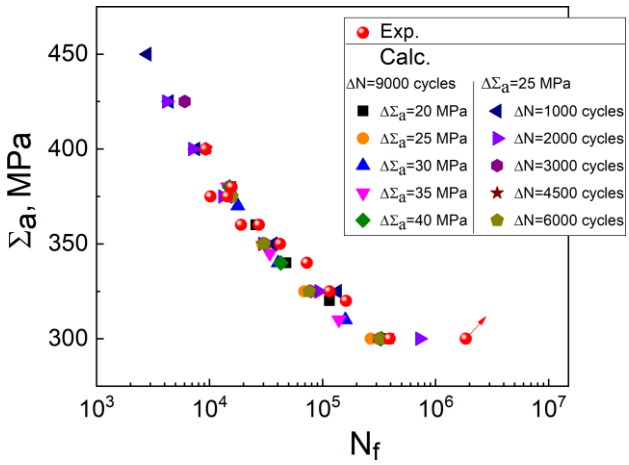

Fig. 9. Experimental and calculated S-N data.

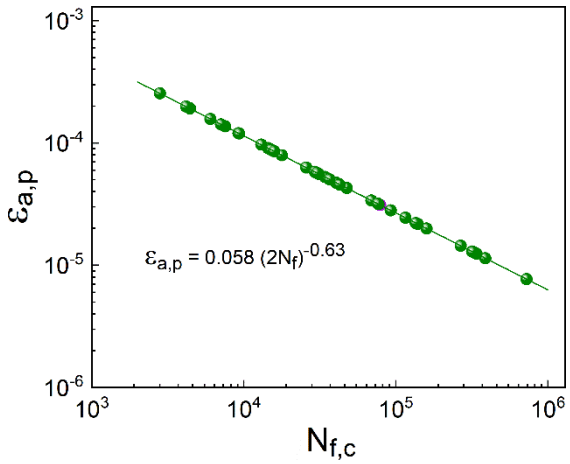

Fig. 10. Correlation between microplasticity strain amplitude and evaluated constant amplitude fatigue life.

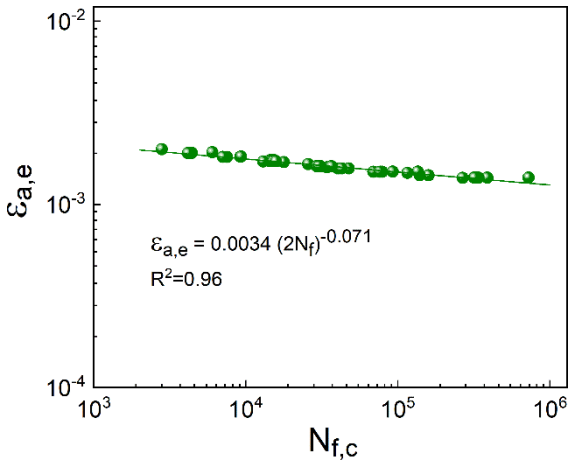

Fig. 11. Correlation between micro-elastic strain amplitude and the calculated fatigue.

PAPER 3

Thermodynamic entropy as a marker of high-cycle fatigue damage accumulation: Example for normalized SAE 1045 steel

Zhenjie Teng*, Haoran Wu, Christian Boller, Peter Starke

Fatigue Fract Eng Mater Struct, 2020; 43:2854-2866. DOI:10.1111/ffe.13303

Copyright:

This is an open access article distributed under the terms of the Creative Commons CC BY license, which permits unrestricted use, distribution, and reproduction in any medium, provided the original work is properly cited.

Thermodynamic entropy as a marker of high-cycle fatigue damage accumulation: Example for normalized SAE 1045 steel

Zhenjie Teng [a, b, *], Haoran Wu [a, b], Christian Boller [a], Peter Starke [a, b]

[a] *Chair of Non-Destructive Testing and Quality Assurance, Saarland University, Saarbrücken 66125, Germany*

[b] *Department of Materials Science and Materials Testing, University of Applied Sciences Kaiserslautern, Kaiserslautern 67659, Germany*

Abstract

A non-destructive thermographic methodology is utilized to determine the fracture fatigue entropy for evaluating the fatigue damage in metals within the high cycle fatigue regime. Thermodynamic entropy is shown to play an important role in the fatigue process to trace the fatigue damage as an irreversible degradation of a metallic material being subjected to cyclic elastic-plastic loading. This paper presents a method to evaluate fatigue damage in the normalized SAE 1045 steel being based on the concept of thermodynamic entropy and its non-linearities. The procedure looks to be applicable to constant and load increase tests proven by experiments.

Keywords: Thermodynamic entropy; High cycle fatigue; Fatigue damage; Damage accumulation

Nomenclature

A_k	Thermodynamic force	ε_f'	Fatigue ductility coefficient
D_0	Initial damage	ε_p	Plastic strain
D_c	Critical damage	σ_f	Fatigue strength
D_k	Damage parameter at k-th stage	σ_f'	Fatigue strength coefficient
D_{k-1}	Damage parameter at (k-1)-th stage	τ_{eq}	Time constant
E_d	Dissipated energy	$\Delta\sigma_a$	Load increase step
E_s	Stored energy	ΔN	Load step length
J_q	Heat flux vector	ΔU	Change in internal energy
N_f	Number of cycles to failure	T	Temperature
N_i	Number of cycles to failure at stress amplitude σ_a	A	Material parameter
N_k	Number of cycles at k-th stage	B	Material parameter
N_{k-1}	Number of cycles at (k-1)-th stage	D	Damage variable
T_0	Equilibrium temperature	Q	Heat dissipation
V_k	Internal state variables	R	Stress ratio
W_p	Plastic energy	W	Mechanical work
c_p	Heat capacity	b	Fatigue strength exponent
d_1	Intrinsic dissipation term	c	Fatigue ductility exponent
n_i	Number of cycles at a given stress amplitude σ_a	f	Frequency
r_{ext}	Heat exchange	k	Heat conductivity
$\dot{s}$	Entropy generation rate	t	Time
s_0	Initial entropy generation	u	Specific internal energy
s_c	Critical entropy generation	$\boldsymbol{\sigma}$	Cauchy stress tensor
s_f	Maximum entropy generation	β	Taylor-Quinney coefficient
s_i	Internal coupling source term	γ	Entropy per unit volume
s_{k-1}	Accumulated entropy at (k-1)-th stage	ε	Total strain
s_{the}	Thermoelastic source term	θ	Change in temperature
t_f	Time to failure	ρ	Mass density
$\dot{\boldsymbol{\varepsilon}}$	Eulerian strain rate tensor	τ	Time of one loading cycle
ε_e	Elastic strain	ψ	Helmholtz free energy

1. Introduction

Components in engineering are susceptible to fatigue and fracture if they are subjected to cyclic loads under operating conditions, which can lead to reduced usage or, in the worst case, to failure if threshold values are exceeded. In particular, the evaluation of the cumulative fatigue damage during the operation of those components and systems with regard to the prediction of fatigue life or for monitoring the integrity plays a decisive role [1]. Due to accumulation fatigue damage increases with an increasing number of load cycles and ultimately leads to failure, whereby the time between damage initiation and failure depends on the load level, the type of load, the environmental conditions, and possibly other factors. The fatigue damage of metals comprises four stages [2], including

- Formation of dislocations and persistent slip bands;
- Nucleation of dislocations with the transition to micro-cracks;
- Micro-cracks direction perpendicular and then towards the maximum shear stress,
- Formation of the macro-cracks resulting in the generation of high stress intensities at the crack tips.

Moreover, the final stage includes the propagation of macro-cracks and breaks the metal into two parts.

From the view of Continuum Damage Mechanics (CDM), fatigue damage is a process of accumulation that once reaches a critical state, the structural elements will have a failure and cannot be serviced. Being able to grasp this damage accumulation allows a structure's remaining life to be assessed and even as a warning of the imminent failure that could be considered in the context of structural health monitoring (SHM) [3]. In recent decades, many different models have been proposed for evaluating fatigue damage, whereby the following variables can be classified as:

- Change in dynamic response: i.e., stress, strain, etc. [4,5]
- Change in mechanical properties: i.e., elastic modulus, hardness, tensile strength, reduction area, etc. [4,6-8]

- Change in physical properties: i.e., thermal-, electric-, magnetic properties, etc. [4,9]

Those approaches are mostly derived from the theories of creep or plastic damage, there is always a margin for the improvement to make them more exquisite, and this is what should be discussed. The classic and most commonly used model is the Palmgren-Miner (P-M) rule [10], which is characterized by its simplicity and can be written as follows:

$$D = \sum_{i=1}^{k} \frac{n_i}{N_i} \tag{1}$$

where n_i and N_i are the number of cycles at a given stress amplitude and the lifetime at the same stress amplitude from the corresponding S-N curve, respectively. Damage D accumulates continuously starting from a pristine condition with $D = 0$ and reaches $D = 1$ when the component fails. The quality of the residual life assessment with this rule very much depends on the parameter describing the fatigue life curve. Traditionally this parameter has been stress or strain only. However, more complex combinations such as those proposed by Smith, Watson and Topper [11], Morrow [12] or Vormwald [13] are examples on how effects generating from notches, mean stresses, load sequence effects or others can be considered as well. Much of this can be found in textbooks such as Schijve [2], Haibach [14], Radaj/Vormwald [15]. Still the damage parameter D can vary by a factor of 2 or more being the result of a variety of other material intrinsic effects not covered so far by parameters nor possibly monitored by any sensing device. Much research work has been done in that regard including many non-linear stress-dependent cumulative damage theories such as to be found in Refs. [5,16-20] where the accumulated damage versus the stress amplitude applied follows an exponential growth. The results obtained by the classic P-M rule are often overestimated when compared with nonlinear models or experimentally obtained data.

In order to improve the prediction of damage accumulation processes, various physically based measurement methods can be used, which can also be assigned to the field of non-destructive testing (NDT). In this context temperature measurement in particular provides parameters that can be used to evaluate the fatigue-related damaging behavior of metallic materials. As the damage can be an energy dissipative process, it

must obey the laws of thermodynamics fundamentally related to an entropy approach [21]. In general, the fatigue mechanisms of a specimen or component are the result of irreversible thermodynamic processes taking place in the specimen or component during damage evolution. Degradation is a time dependent index with the increasing disorder [22]. Thus, a basic parameter of thermodynamics is entropy, which can be derived from temperature measurements and can describe the degradation of the material due to fatigue loading.

Classical and statistics-based methods derived from entropy have been proposed to evaluate the fatigue damage as well as the remaining lifetime of materials and structures [23-26]. The accumulation of entropy generated during a fatigue test is calculated and regarded as a material property named the Fatigue Fracture Entropy (FFE), where this parameter stays constant for a certain material until failure. This parameter is moreover independent of loading sequences, frequency, and amplitudes, etc. [27] and affects the fatigue such as damage evaluation [28], temperature response [29], and reliability [30] of the material. However, those FFE calculation models have not taken the evolution of temperature variation entropy before final facture into account, which should be much higher than in the initial phase.

In the work presented here, the FFE approach has been modified and used as an index of degradation to monitor fatigue damage for the normalized SAE 1045 steel. The approach is based on temperature measurements carried out during constant amplitude and variable amplitude loading tests in the high cycle fatigue regime. The experimental procedure is presented below followed by a methodology being related to damage accumulation based on the concept of the thermodynamic entropy. The results obtained are discussed with regard to the concept of entropy under plastic deformation and conclusions are finally drawn.

2. Experimental procedure

2.1. Material

The material used in this study is the unalloyed medium carbon steel SAE1045 (German-standard: C45E), which is in accordance to DIN EN 10083-1. The requested and manufacturer determined chemical compositions and the material properties are

listed in Tables 1 and 2, respectively.

2.2. Fatigue testing

Tension-compression fatigue tests were performed using a servo-hydraulic fatigue testing system (Shimadzu EHF-L) with a 20/25 kN cyclic/quasi-static load capacity as shown in Fig. 1 and run at a loading frequency of 5 Hz and a stress ratio of $R = -1$, respectively. Temperature measurement areas (10×10 pixels) defined on the specimens' surface were recorded by using an IR camera (Micro-Epsilon thermoIMAGER TIM 245) with a resolution of 382×288 pixels in the full window mode and at a thermal sensitivity of 0.04 K at room temperature and with a 100 Hz recording frequency in order to avoid too big data volumes. The cylindrical hourglass specimen was designed with an arc radius of 30 mm and a minimum diameter in the gauge length of 5.8 mm, and the surface of the specimens were coated with a thin layer of matt black paint for having a high and uniform thermal emissivity.

The fatigue tests were carried out in load control mode with a sinusoidal waveform and a stress function to be expressed as $\sigma(t) = \sigma_a \sin(10\pi t)$. In order to evaluate the processes of fatigue damage evolution, two types of fatigue tests were performed, the one being a constant amplitude and the other a load increase test, respectively. The details of the respective load types for the tests performed are summarized below:

- Constant amplitude tests: 5 tests at stress amplitudes between 320 and 400 MPa, with each test differing in 20 MPa of stress amplitude.

- Load increase tests: All tests starting from a stress amplitude level of $\sigma_{a,start} = 100$ MPa, being below the fatigue strength, $\sigma_f = 300$ MPa [32], of the SAE 1045 steel investigated at $R = -1$ and being loaded for a defined number of cycles ΔN before increasing the stress amplitude by an increment $\Delta\sigma_a$ to a next stress amplitude level while cycling again the specimen with a number ΔN of cycles and this to be continued so forth until the specimen failed. A distinction has been made between tests in which (a) ΔN was retained constant at 9000 cycles and $\Delta\sigma_a$ increased in steps of 5 MPa from 20 to 40 MPa as well as in tests where (b) $\Delta\sigma_a$ was kept at 25 MPa and ΔN was varied to step lengths of 1000, 2000, 3000, 4500, and 6000 cycles, respectively.

3. Methodology

3.1. First law of thermodynamics

The first law of thermodynamics describes the energy balance status, which can be applied to every thermomechanical process. For a defined volume of material under load such as the volume of a fatigue specimen in its minimum cross-section this can be formulated as:

$$\Delta U = Q + W \tag{2}$$

where ΔU indicates the change of the internal energy, Q is the thermal energy dissipated as heat and W is the work applied to deform the material under elastic-plastic conditions. For a given quantity term Eq. (2) can be formulated as:

$$\rho \dot{u} = \boldsymbol{\sigma} : \dot{\boldsymbol{\varepsilon}} - \mathrm{div} J_q \tag{3}$$

where u denotes the specific internal energy, $\boldsymbol{\sigma}$ the Cauchy stress tensor, $\dot{\boldsymbol{\varepsilon}}$ the Eulerian strain rate tensor and J_q the heat flux vector. The term $\boldsymbol{\sigma} : \dot{\boldsymbol{\varepsilon}}$ is the stress power for uniaxial cyclic loading expressed as $\boldsymbol{\sigma} : \dot{\boldsymbol{\varepsilon}} = \sigma : (\dot{\varepsilon}_e + \dot{\varepsilon}_p)$ where ε_e and ε_p are the elastic and plastic strain portions respectively.

The heat flux, internal energy, entropy, and Cauchy stress are the state functions in thermodynamics. For an ideal thermoelastic state, those parameters are a function of the deformation and the temperature state variables [33]. However, if the deformation is in the inelastic state, the situation is more complex and the internal state variables, such as mechanical, thermal, electrical, etc. in the history of deformation sequence need to be considered.

Furthermore, those variables can be associated with defects in a material such as dislocations or voids in the materials' microstructure [34].

The Helmholtz free energy is defined as a part of the internal energy of a system and can be expressed as:

$$\psi = u - T\gamma \tag{4}$$

where T is the temperature and γ the entropy per unit volume. The Helmholtz free energy ψ is considered as a function of temperature and multiple internal state variables [35], and can be stated as:

$$\psi = \psi\left(\varepsilon_e, T, V_k\right) \tag{5}$$

where V_k is introduced as a set of internal state variables. Following this the rate of free energy can be developed as:

$$\dot{\psi} = \frac{\partial \psi}{\partial \varepsilon_e} : \dot{\varepsilon}_e + \frac{\partial \psi}{\partial T} : \dot{T} + \frac{\partial \psi}{\partial V_k} : \dot{V}_k \tag{6}$$

By using the thermoelastic relationships valid for small strains, where $\sigma = \frac{\partial \psi}{\partial \varepsilon_e}$ and $\gamma = -\frac{\partial \psi}{\partial T}$, and further substituting Eqs. (4) and (6) in (3), the thermodynamic energy balance equation can be written as follows:

$$\rho c_p \dot{T} = \sigma : \dot{\varepsilon}_p - \mathrm{div} J_q + T \frac{\partial \sigma}{\partial T} : \dot{\varepsilon}_e + \left(A_k - T \frac{\partial A_k}{\partial T}\right) \dot{V}_k \tag{7}$$

where $c_p = \frac{T}{\rho} \frac{\partial \gamma}{\partial T}$ represents the heat capacity, $A_k = -\frac{\partial \psi}{\partial V_k}$, where A_k is the thermodynamic force associated with the internal variables and k the heat conductivity, ρ the materials' density. $\rho c_p \dot{T}$ is the rate of the change in internal energy. $\sigma : \dot{\varepsilon}_p$ is the heat generation due to the plastic deformation and symbolized as w_p, $\mathrm{div} J_q$ is the heat transfer by conduction, $T \frac{\partial \sigma}{\partial T} : \dot{\varepsilon}_e$ is the thermoelastic coupling, and $\left(A_k - T \frac{\partial A_k}{\partial T}\right) \dot{V}_k$ is related to the internal state variables. Thus, the mean temperature rise within the specimen's gauge length section is related to the plastic strain energy term and the thermoelastic effect to the thermoelastic coupling term, whereby tension results in a decrease and compression in an increase in the temperature respectively [33].

3.2. Second law of thermodynamics

The second law of thermodynamics (Clausius-Duhem inequality), which is applied to a specimen subjected to fatigue, is generally written as follows:

$$\dot{s} = \mathrm{div}\left(\frac{J_q}{T}\right) + \rho \dot{\gamma} \tag{8}$$

and can be further developed as:

$$\dot{s} = \rho\dot{\gamma} + \frac{J_q}{T} - \left(\frac{J_q}{T^2} \cdot \nabla T\right) \geq 0 \tag{9}$$

where $\dot{s}$ is the entropy generation rate resulting from the irreversibility of thermodynamic transformation. The use of the first law of thermodynamics Eq. (3) and the Helmholtz free energy Eq. (4) applied to the second law of thermodynamics Eq. (8) leads to

$$\dot{s} = \frac{\sigma : \dot{\varepsilon}}{T} - \frac{\rho}{T}\left(\dot{\psi} + \gamma\dot{T}\right) - \left(\frac{J_q}{T^2} \cdot \nabla T\right) \geq 0 \tag{10}$$

Combining Eqs. (6) and (10) and using $\varepsilon_p = \varepsilon - \varepsilon_e$ as a simplification due to a small strain assumption in the case of high cycle fatigue, the specific entropy generation flow can be expressed as:

$$\dot{s} = \frac{\sigma : \dot{\varepsilon}_p}{T} - \frac{A_k \dot{V}_k}{T} - \left(\frac{J_q}{T^2} \cdot \nabla T\right) \geq 0 \tag{11}$$

Where [36]:

- $\frac{\sigma : \dot{\varepsilon}_p}{T}$ is the specific entropy generation derived from plastic deformation.
- $-\frac{A_k \dot{V}_k}{T}$ is the specific entropy generation caused by irreversible deformation, such as strain hardening, phase transformation, etc.
- $\frac{J_q}{T^2} \cdot \nabla T$ is the specific entropy generation provided through heat conduction.

Therefore, the entropy generation accumulation can be obtained by integrating Eq. (11):

$$s = \int_0^t \dot{s}\, dt \tag{12}$$

Thus, the fracture fatigue entropy, namely the maximum entropy generation at the onset of fracture generated by irreversibility during the fatigue process is $s_f = \int_0^{t_f} \dot{s}\, dt$, where t_f is the time to failure. In the case of materials with low hardening potential and at sufficiently high fatigue test frequencies, the second and the third term of Eq.

(11) can be neglected as it was proposed in [36]:

$$\left|\frac{A_k \dot{V}_k}{T}\right| \ll \left|\frac{\sigma:\dot{\varepsilon}_p}{T}\right|, \quad \left|\frac{J_q}{T^2}\cdot\nabla T\right| \ll \left|\frac{\sigma:\dot{\varepsilon}_p}{T}\right| \tag{13}$$

In this case, the generated entropy can be simplified as:

$$s_f = \int_0^{t_f} \frac{\sigma:\dot{\varepsilon}_p}{T}\, dt \tag{14}$$

The cyclic plastic strain energy generation per second, $W_p = \sigma:\dot{\varepsilon}_p$, can be expressed by an empirical relation, which was originally proposed by Morrow [37]:

$$W_p = 2^{2+b+c}\sigma_f'\varepsilon_f'\left(\frac{c-b}{c+b}\right)N_f^{b+c} \tag{15}$$

where b and c are the fatigue strength exponent and the fatigue ductility exponent respectively, σ_f' is the fatigue strength coefficient, ε_f' is the fatigue ductility coefficient, and N_f is the number of cycles to failure. The above-mentioned relation can be further used to evaluate the entropy generation rate [24,26,38]. The constant W_p is given as a default constant, since the above parameters are determined constantly for a fatigue test. However, numerous studies [39-48] have shown that the temperature evolution of a specimen or a component that had been exposed to a load amplitude higher than its fatigue limit appears in three stages, which is schematically represented in Fig. 2. This can be divided into an initial temperature increase (stage I), a predominant temperature stabilized stage (stage II), and a sudden temperature increase stage close before fracture (stage III). What needs to be addressed is that the entropy generation rate in the first stage cannot be higher than in the second stage and then in the third respectively. To circumvent this disadvantage and to modify the entropy calculation, a method for evaluating W_p based on intrinsic dissipation is presented in the following sections.

3.3. Intrinsic dissipation

Following the laws of thermodynamics, Boulanger et al [49] proposed a specific form of heat diffusion of a local heat by measuring the temperature fields of the surface of a specimen during fatigue tests which are formulated as:

$$\rho c_p \dot{\theta} - \mathrm{div}(k: \mathrm{grad}\theta) = s_{the} + s_i + d_1 + r_{ext} \tag{16}$$

where c_p is the heat capacity, $\theta = T - T_0$ the change in temperature with T_0 being the equilibrium temperature, and k the thermal conductivity. On the right-hand side of Eq. (16), s_{the} indicates the thermoelastic source term, s_i the internal coupling source term, d_1 the intrinsic dissipation term, and r_{ext} the heat exchange between the specimen and the surroundings, respectively.

For the fatigue tests were performed at room temperature, the external heat source r_{ext} denotes the heat loss into the environment and it can be influenced by conduction, convection, and radiation. Those elements are very hard to be accurately estimated as they strongly depend on the boundary conditions of the test setup. Normally, it is supposed to be a simple time-independent and linear-solution [50]:

$$r_{ext} = -\rho c_p \frac{\theta}{\tau_{eq}} \tag{17}$$

where τ_{eq} represents a time constant characterizing the heat loss. Here, it is assumed the change in temperature during the high cycle fatigue tests do not influence the microstructure, and then the internal coupling source s_i can be neglected under the given boundary condition because the thermal process due to fatigue is considered as a pure dissipation mechanism. Considering the 0D heat diffusion model is used in the present case, then Eq. 16 can be further simplified as:

$$\rho c_p \left(\frac{\partial \theta}{\partial t} + \frac{\theta}{\tau_{eq}} \right) = d_1 + s_{the} \tag{18}$$

In the fully reversed tension-compression fatigue test, the thermoelastic source s_{the} turns out to be zero after each loading cycle due to the cyclic load mode, and the temperature variation tends to be asymptotic with $\dot{\theta} = 0$. According to the above estimates, the dissipated energy within a time unit can be simplified as follows [49,51]:

$$d_1 = \rho c_p \frac{\theta}{\tau_{eq}} \tag{19}$$

3.4. A unified entropy approach

According to the energy balance principle, the dissipated energy takes up most of the

plastic energy generated during cyclic loading but not all. The remainder is stored within the material, stored energy, that takes part in the process of the microstructure evolution and results from micro defects, crystal lattice, or dislocation structures, as well as possibly others.

This energy is described as stored energy E_s and is comparable to the stored energy of cold work associated with plastic deformation. The Taylor-Quinney coefficient[52,53], β is used to bridge between the fraction of plastic energy W_p and the dissipated energy E_d:

$$\beta = \frac{W_p - E_s}{W_p} = \frac{E_d}{W_p} \tag{20}$$

For metallic materials studies have shown that approximately 80-100% of the plastic work dissipates as heat, leading to an increase in the specimen's temperature [50,51,54,55] and it is normally assumed β to be an independent material constant. For the material considered here the intermediate value is adapted to $\beta = 0.9$.

The dissipated energy during one loading cycle can be integrated as:

$$E_d = \int_t^{t+\tau} d_1 \, dt \tag{21}$$

where $\tau = 1/f$ indicates the period of one loading cycle. Substituting Eqs. (19), (20), (21) into Eq. (14), the entropy generation is obtained as:

$$s(t) = \frac{\rho c_p}{f\beta\tau_{eq}} \int_0^t \left(\frac{T - T_0}{T}\right) dt \tag{22}$$

3.5. Damage accumulation

Based on the theory of continuum damage mechanics (CDM), failure of the specimen occurs when the damage parameter reaches a critical value. Chaboche [16] defined this value as the breaking point of the continuum element, which is the point where fatigue damage results in the initiation of macro-cracks. Thus, the fatigue damage accumulation can be regarded as a degradation of the material. A relationship between degradation caused by damage and entropy generation was proposed by Naderi [38] using degradation entropy generation, which is:

$$D = A + B \cdot \ln(1 - s/s_f) \tag{23}$$

where D is a damage parameter, and A and B are material parameters respectively.

Damage is initiated by slipping and then followed by slip bands, intrusions and extrusions which result in micro-cracks, whereby different of the micro-cracks merge, leading to micro-cracks finally before a complete fracture occurs. Here, D_c is defined as the critical damage value which corresponds to the onset of the macro-crack initiation and s_c is the critical entropy generation value, which corresponds to the onset of the temperature rise at the beginning of the macro-crack initiation or before the complete failure. This critical condition is considered as an indication of an imminent fracture and could be used as a marker for the purposes of SHM. In addition, let s_0 be defined as the initial entropy generation value with respect to the initial damage of D_0 for a constant stress amplitude fatigue test, then Eq. (23) yields to:

$$\begin{cases} D_0 = A + B \cdot \ln(1 - s_0/s_f) \\ D_c = A + B \cdot \ln(1 - s_c/s_f) \end{cases} \tag{24}$$

Solving A and B and substituting into Eq. (23):

$$D = D_0 + \frac{D_c - D_0}{\ln\left[(1-s_c/s_f)/(1-s_0/s_f)\right]} \ln\left(\frac{1-s/s_f}{1-s_0/s_f}\right) \tag{25}$$

Eq. (24) provides a relationship between damage evolution and the history effect of entropy generation. For constant amplitude tests, the initial damage is zero ($D_0 = 0$) with no entropy generated. Eq. (25) can be simplified to:

$$D = \frac{D_c}{\ln(1-s_c/s_f)} \ln(1 - s/s_f) \tag{26}$$

In engineering applications, most components are subjected to variable amplitude loading and hence should have “entropy memory”. Then Eq. (25) can be further extended to an n-stage sequence:

$$D_k = D_{k-1} + \frac{D_c - D_{k-1}}{\ln\left[(1-s_c/s_f)/(1-s_{k-1}/s_f)\right]} \ln\left(\frac{1-s/s_f}{1-s_{k-1}/s_f}\right), \quad \text{for } k = 1, 2, \dots, n \tag{27}$$

where D_{k-1} and s_{k-1} are the damage parameter and the accumulated entropy for (k-1)-th stage, respectively.

The schematic principle for the fatigue damage evolution versus the number of cycles is shown in Fig. 3 for load increase tests, where N_f is the number of cycles to failure and $(N_k - N_{k-1})$ is the number of cycles of the corresponding loading stage. During the fatigue process, the degradation progresses with the existing micro-cracks and the nucleation and propagation of the new micro-cracks. Meanwhile, the entropy generates due to the progressed irreversibility at each stage of loading. The degradation grows and the entropy accumulates from the beginning to the onset of the second stage. Similarly, the accumulated damage at the end of one loading stage is the initial damage of the next stage and the transition point is named as the knee point. The number of micro-cracks increases and the entropy increases as well. Finally, in the last stage, as soon as the macro-cracks once occur, the entropy and hence damage propagates exponentially perpendicular to the stress amplitude level and up to the final failure.

4. Results and discussion

4.1. Evolutions of entropy generation rate

The evolutions of the entropy generation rate at constant amplitude and load increase tests are given in Figs. 4 and 5, respectively, for the SAE 1045 steel. For the constant amplitude tests, the progress of the rate development is similar to the three-stage behavior schematically shown in Fig. 2.

During the first few thousand cycles, the entropy generation rate increases and then reaches a more stationary state with the rate development starting at zero. For the different stress amplitudes, the average rate drifts upwards with an increasing number of cycles until a steady-state is achieved. With the exception of the stress amplitude of 400 MPa, the rate in stage II is somewhat lower may cause by cyclic hardening effects. There is no doubt that the stable mean entropy generation rate along the gauge of the specimen increases monotonically with increasing stress levels. Finally, the rate increases strongly due to the large plastic deformation caused by stress intensities at the crack tips.

For the load increase tests the entropy generation rate remained close to zero at the beginning of the loading sequence, indicating that for stress amplitudes below the fatigue limit fatigue damage due to the internal friction effect is not measurable [56],

shear stresses within the lattice structure are below a certain critical value, and dislocation reactions, such as dislocation movement, the formation of walls or sub-grains, are limited. When the stress amplitude is above the fatigue limit zones of localized microplastic deformation emerge and dislocation reactions such as increase or decrease in dislocation density or movement appear. Those processes lead to an irreversible microstructural change and consequently to an increase in dissipated energy, which is reflected in the macroscopic appearance of the temperature [51]. The development of the entropy generation rate obviously shows an accelerated increase corresponding to the stepwise increased stress amplitudes and the first two stages can be observed while stage III indicates the fracture of the specimen and is limited to the last loading sequence of the load increase test.

4.2. Damage evolution in constant amplitude tests

Fig. 6 shows the evolution of the damage parameter for the SAE1045 steel at different stress amplitudes of the constant amplitude loading tests. The specimens have a low defect density at the beginning, where $D_0 = 0$. It can be clearly seen that in the early stages of the fatigue life, the damage parameter can be approximated to increase monotonically with the slope increasing continuously in a non-linear way with an increasing number of cycles until final fracture. This development is different for the different stress amplitudes being applied as can be seen from the results shown in Fig. 6. This further proves that the linear accumulation postulated in the P-M rule does not hold.

Fig. 7 graphically presents the damage evolution versus normalized entropy generation (s/s_f) for different stress amplitudes. At the same normalized entropy level, the higher stress amplitudes result in higher values of the fatigue damage parameter. The discrepancy in the evolution of the damage parameter for the fatigue test with a stress amplitude of 400 MPa is due to cyclic hardening processes shown in Fig. 4 and has, therefore, to be considered separately.

According to Eq. (26) the result shows a good relationship between fatigue degradation and entropy generation. It is therefore pointed out that thermodynamic entropy as an index of fatigue degradation can be used to assess the fatigue damage in the cyclic loading process.

4.3. Damage evolution in load increase tests

A load increase test is an interesting experiment to study the entropy development at different stress levels within a single experiment. Using the fatigue damage equation and the entropy generation relationship, the evolution of the fatigue damage can be evaluated.

The damage evolution versus the fatigue life of the SAE1045 steel exposed to the load increase sequence as described before is shown in Fig. 8. In the unloaded state, the specimens show initially a low defect density, $D_0 = 0$, namely no micro-cracks or damage, and to be free from an entropy history expressed as $s_i = 0$. When the stress amplitudes are lower than the fatigue limit no measurable fatigue damage is observed from the entropy information. Measurable degradation starts with the typical fatigue characteristics resulting from intrusions and extrusions that can be observed on a specimens' surface. Thereafter micro-cracks start to nucleate and then move along the slip planes of maximum shear stress, which is in the case of uniaxial loading 45° related to the loading direction. The higher the stress amplitude is applied, the more sites of microplastic deformation are activated being a consequence of inconsistent grain boundaries, localized dislocations, and inhomogeneous grain size. When the stress is higher than the fatigue limit, plastic deformation becomes measurable and the entropy progressively increases from load level to load level. It can be observed from Fig. 5 that stage I and stage II can be described for each loading level and it is therefore logical to assume that what has been accumulated at the end of stage I corresponds to the initial value of stage II, and being continued so forth. Thus, the rate of the degradation changes with the amount of stress being applied which can be observed from the knee points indicated by arrows in Fig. 8a. As the number of cycles increases, micro-cracks are nucleated and connected to form a macro-crack, which can be referred to as the critical damage through measurement of a critical entropy formation. Near the final failure, the damage size increases dramatically and the fracture occurs after the formation of macro-cracks with the fatigue damage parameter reaching the value of 1.

As discussed above, the entropy generation during the fatigue process can be used as an index to evaluate the fatigue degradation. Simultaneously with the rise of the degradation, the entropy continuously increases as well towards the final fracture

fatigue entropy (FFE). Based on former work the FFE for a certain material is constant [36,38], regardless of the type of the mechanical fatigue load, such as tension-compression, bending or torsion, frequency, and geometry, and possibly others, which has been proven through the application of different models of FFE calculation [27,36]. Based on Eq. (21), the results of FFE calculations for fifteen specimens are given in Fig. 9. The spreading of final test data is a bit large, excluding the two too high points, the FFE for SAE 1045 steel is about 8.6 MJ/m^{3}K. For a more precise fatigue damage calculation, the above used FFE data came from its own test instead of the average value. Besides, more load-history tests will be performed in the future to quantify the dispersion of the FFE of SAE 1045 steel.

The evolution of fatigue damage versus the normalized entropy generation is depicted in Fig. 10. As the damage progresses towards the final fatigue failure, the accumulated entropy increases monotonically until FFE. The agreement is very good, which can prove that FFE is independent of the load sequence. It should also be noted that the cumulative entropy generation gives a unit value which can be used as a criterion for the onset of fatigue damage or can be used with regard to SHM activities for detecting damage before final fracture.

5. Conclusions

A modified approach based on thermodynamic entropy generation is an effective strategy for monitoring the development of fatigue damage, which has been verified through various constant amplitude and load increase tests. The evolution of the entropy generation rate during the fatigue testing can be well given based on this modified entropy calculation method. The tests were carried out at room temperature under stress-control and a stress ratio of $R = -1$. The material investigated was the unalloyed medium carbon steel SAE 1045, which is widely used for engineering components. Unlike the Palmgren-Miner's rule, the proposed method takes the temperature or the fracture fatigue entropy as an index of degradation, and a non-linear equation is used to characterize the relationship between the degradation provided by damage and entropy generation. It can be seen from the results that the fracture fatigue entropy is independent of the load-time history and can be calculated to a value of ~8.6 MJ/m^{3}K. As expected, there is an overestimation of the fatigue damage by using the linear

Palmgren-Miner's rule, which underlines the advantages of non-linear damage accumulation approaches.

Another thermodynamic parameter, exergy, can also be used to evaluate fatigue damage since it considers the influence of the environment on the irreversibility of the thermodynamic system and the calculation process is similar to the entropy, which will be discussed in the future. In addition, the proposed approach still has to be subjected to a comprehensive experimental validation, whereby in addition to different stress amplitudes also different load time histories have to be included in the verification, and even with different metals and alloys, or with heat-treatment procedures. Corresponding investigations are currently ongoing and will be continued within the framework of further research work.

Acknowledgments

This work was supported by the German Research Foundation (Deutsche Forschungsgemeinschaft DFG, STA 1133/6-1) and the China Scholarship Council.

References

[1] Schütz W. A history of fatigue. Eng Fract Mech. 1996. 54:263-300.

[2] Schijve J. Fatigue of structures and materials. Dordrecht, Boston: Kluwer Academic Publ. 2001.

[3] Boller C, Chang FK, Fujino Y. Encyclopedia of structural health monitoring. John Wiley & Sons. 2009.

[4] Lematre J, Dufailly J, Damage measurements. Eng Fract Mech. 1987; 28:643-61.

[5] Zhu SP, Hao YZ, De Oliveira Correi JAF, Lesiuk G., De Jesus AMP, Nonlinear fatigue damage accumulation and life prediction of metals: A comparative study. Fatigue Fract Eng Mater Struct. 2019; 42:1271-1281.

[6] Rotem A, Residual strength after fatigue loading. Int J Fatigue. 1988;10:27-31.

[7] Ye DY, Wang ZL. An approach to investigate pre-nucleation fatigue of cyclically loaded metals using Vickers microhardness tests. Int J Fatigue. 2001; 23:85-91.

[8] Ye DY, Wang ZL. A new approach to low-cycle fatigue damage based on

exhaustion of static toughness and dissipation of cyclic plastic strain energy during fatigue. Int J Fatigue. 2001; 23:679-687.

[9] Kocanda S. Fatigue failure of metals. Amsterdam: Elsevier. 1986.

[10] Miner MA. Cumulative damage in fatigue. J Appl Mech. 1945; 12:159-164.

[11] Smith KN, Watson P, Topper TH. A stress-strain function for the fatigue of materials. J Mater.1970; 5:767-778.

[12] Morrow J. Fatigue properties of metals, section 3.2. In: Fatigue Design Handbook, Pub. No. AE-4. SAE, Warrendale, PA. 1968.

[13] Vormwald M, Heuler P, Seeger T. A fracture mechanics based model for cumulative damage assessment as part of fatigue life prediction, in Advances in Fatigue Life Prediction Techniques (Edited by M.R. Mitchell and R.W. Landgraf). San Francisco American Society for Testing and Materials, Philadelphia, STP 1122, 1992.

[14] Haibach E, Betriebsfeste Bauteile. Ermittlung und Nachweis der Betriebsfestigkeit, konstruktive und unternehmerische Gesichtspunkte. Springer Verlag, Berlin. 1992.

[15] Radaj D. Vormwald M.: Ermüdungsfestigkeit. Springerverlag, Berlin, Heidelberg. 2007.

[16] Chaboche JL, Lesne PM. A non-linear continuous fatigue damage model. Fatigue Fract Eng Mater Struct. 1988; 11:1-17.

[17] Shang DG, Yao WX. A nonlinear damage cumulative model for uniaxial fatigue. Int J Fatigue. 1999; 21:187-194.

[18] Benkabouche S, Guechichi H, Amrouche A, Benkhettab M. A modified nonlinear fatigue damage accumulation model under multiaxial variable amplitude loading. Int J Mech Sci. 2015; 100:180-194.

[19] Rege K, Pavlou DG. A one-parameter nonlinear fatigue damage accumulation model. Int J Fatigue. 2017; 98:234-246.

[20] Zhu SP, Liao D, Liu Q, Correi JAFO, De Jesus AMP. Nonlinear fatigue damage accumulation: Isodamage curve-based model and life prediction aspects. Int J

Fatigue. 2019; 128:105185.

[21] Bhattacharya B, Ellingwood B. Continuum damage mechanics analysis of fatigue crack initiation. Int J Fatigue. 1998; 20:631-639.

[22] Bryant MD, Khonsari MM, Ling FF. On the thermodynamics of degradation. Proc R Soc A. 2008; 464:2001-2014.

[23] Basaran C, Nie S. An irreversible thermodynamics theory for damage mechanics of solids. Int J Damage Mech. 2004; 13:205-223.

[24] Naderi M, Khonsari MM. An experimental approach to low-cycle fatigue damage based on thermodynamic entropy. Int J Solids Struct. 2010; 47:875-880.

[25] Liakat M, Khonsari MM. An experimental approach to estimate damage and remaining life of metals under uniaxial fatigue loading. Mater Des. 2014; 57:289-297.

[26] Sun YJ, Hu LS. Assessment of low cycle fatigue life of steam turbine rotor based on a thermodynamic approach. J Eng Gas Turbines Power. 2012; 134:064504(1-4).

[27] Amiri M, Naderi M, Khonsari MM. An experimental approach to evaluate the critical damage. Int J Damage Mech. 2011; 20:89-112.

[28] Karimian SF, Bruck HA, Modarres M. Thermodynamic entropy to detect fatigue crack initiation using digital image correlation, and effect of overload spectrums. Int J Fatigue. 2019; 129:105256.

[29] Salimi H, Pourgol-Mohammad M, Yazdani M. Metal fatigue assessment based on temperature evolution and thermodynamic entropy generation. Int J Fatigue. 2019; 127:403-416.

[30] Ontiveros V, Amiri M, Kahirdeh A, Modarres M. Thermodynamic entropy generation in the course of the fatigue crack initiation. Fatigue Fract Eng Mater Struct. 2017; 40:423-434.

[31] Spittel M, Spittel T. Metal Forming data of ferrous alloys-deformation behavior. Steel symbol/number: C45/1.0503. In H. Warlimont (Ed.). Springer-Verlag Berlin Heidelberg. 2009; 210-215.

[32] Teng ZJ, Wu HR, Boller C, Starke P. Thermography in high cycle fatigue short-

term evaluation procedures applied to a medium carbon steel. Fatigue Fract. Eng. Mater. Struct. 2019; 43:515-526.

[33] Jang JY, Khonsari MM. On the evaluation of fracture fatigue entropy. Theor Appl Fract Mech. 2018; 96:351-361.

[34] Horstemeyer MF, Bammann DJ. Historical review of internal state variable theory for inelasticity. Int J Plasticity. 2010; 26:1310-1334.

[35] Lemaitre J, Chaboche JL. Mechanics of Solid Materials. First ed., Cambridge University Press, Cambridge, UK. 1990.

[36] Ribeiro P, Petit J, Gallimard L. Experimental determination of entropy and exergy in low cycle fatigue. Int J Fatigue. 2019;105333.

[37] Morrow JD. Cyclic plastic strain energy and fatigue of metals. In: Internal friction, damping, and cyclic plasticity. ASTM STP, 1965; 378:45-87.

[38] Naderi M, Khonsari MM. A thermodynamic approach to fatigue damage accumulation under variable loading. Mat Sci Eng A. 2010; 527:6133-6139.

[39] Audenino AL, Crupi V, Zanetti EM. Correlation between thermography and internal damping in metals. Int J Fatigue. 2003; 25:343-351.

[40] Curà F, Gallinatti AE, Sesana R. Dissipative aspects in thermographic methods. Fatigue Fract Eng Mater Struct. 2012; 35:1133-1147.

[41] Risitano A, Risitano G. Cumulative damage evaluation in multiple cycle fatigue tests taking into account energy parameters. Int J Fatigue. 2013; 48:214-222.

[42] Wang XG, Crupi V, Jiang C, Guglielmino E. Quantitative Thermographic Methodology for fatigue life assessment in a multiscale energy dissipation framework. Int J Fatigue. 2015; 81:249-256.

[43] Knobbe H, Starke P, Hereñú S, Christ HJ, Eifler D. Cyclic deformation behaviour, microstructural evolution and fatigue life of duplex steel AISI 329 LN. Int J Fatigue. 2015; 80:81-89.

[44] He C, Liu YJ, Fang DH, Wang QY. Very high cycle fatigue behavior of bridge steel welded joint. Theor App Mech L. 2012; 2(3):031010.

[45] He C, Tian RH, Liu YJ, Li JK, Wang QY. Ultrasonic fatigue damage behavior of

304L austenitic stainless steel based on micro-plasticity and heat dissipation. J Iron Steel Res Int. 2015; 22:638-644.

[46] Liu HQ, Wang QY, Huang ZY, Teng ZJ. High-cycle fatigue and thermal dissipation investigations for low carbon steel Q345. Key Eng Mater. 2016; 664:305-313.

[47] Micone N, Waele W. On the application of infrared thermography and potential drop for the accelerated determination of an S-N curve. Exp Mech. 2017; 57:143-153.

[48] Wu HR, Bäumchen A, Engel A, Acosta R, Boller C, Starke P. SteBLife – A new short-time procedure for the evaluation of fatigue data. Int J Fatigue. 2019; 124:82-88.

[49] Boulanger T, Chrysochoos A, Mabru C, Galtier A. Calorimetric analysis of dissipative and thermoelastic effects associated with the fatigue behavior of steels. Int J Fatigue. 2004; 26:221-229.

[50] Wang XG, Feng ES, Jiang C. A microplasticity evaluation method in very high cycle fatigue. Int J Fatigue. 2017; 94:6-15.

[51] Fan JL, Zhao YG, Guo XL. A unifying energy approach for high cycle fatigue behavior evaluation. Mech Mater. 2018; 120:15-25.

[52] Farren WS, Taylor GI. The heat developed during plastic extension of metals. Proc R Soc A. 1925; 107:422-451.

[53] Taylor GI, Quinney H. The latent energy remaining in a metal after cold working. Proc R Soc A. 1934; 143(849):307-326.

[54] Eifler D, Piotrowski A. Bewertung zyklischer Verformungsvorgange metallischer Werkstoffe mit Hilfe mechanischer, thermometrischer und elektrischer Messverfahren. Mat-Wiss U Werkstofftech. 1995; 26:121-127.

[55] Rosakis P, Rosakis AJ, Ravichandran G, Hodowany J. A thermodynamic internal variable model for the partition of plastic work into heat and stored energy in metals. J Mech Phys Solids. 2000; 48:581-607.

[56] Guo Q, Guo XL, Fan JL, Syed R, Wu CW. An energy method for rapid evaluation of high-cycle fatigue parameters based on intrinsic dissipation. Int J Fatigue. 2015;

80:136-144.

Table 1

Chemical compositions of normalized SAE 1045 [32].

(Wt.-%)		C	Si	Mn	P	S	Cr	Mo	Ni
DIN	min.	0.42	-	0.50	-	-	-	-	-
	max.	0.50	0.40	0.80	0.030	0.035	0.40	0.10	0.40
Customer's report		0.47	0.23	0.72	0.012	0.013	0.06	0.014	0.07

Table 2

Material properties of normalized SAE 1045 [32].

Property	Unit	Value	Property	Unit	Value
Ultimate strength	MPa	710	Mass density	kg m^{-3}	7821
Yield strength	MPa	413	Specific heat capacity	J kg^{-1} K^{-1}	474
Poisson's ratio	—	0.3	Heat conduction coefficient	W m^{-1} K^{-1}	48
Young's modulus	GPa	214	Linear thermal expansion coefficient	10^{-6} K^{-1}	11
Brinell hardness	HB	210			

Thermophysical parameters taken from the Ref.[31]

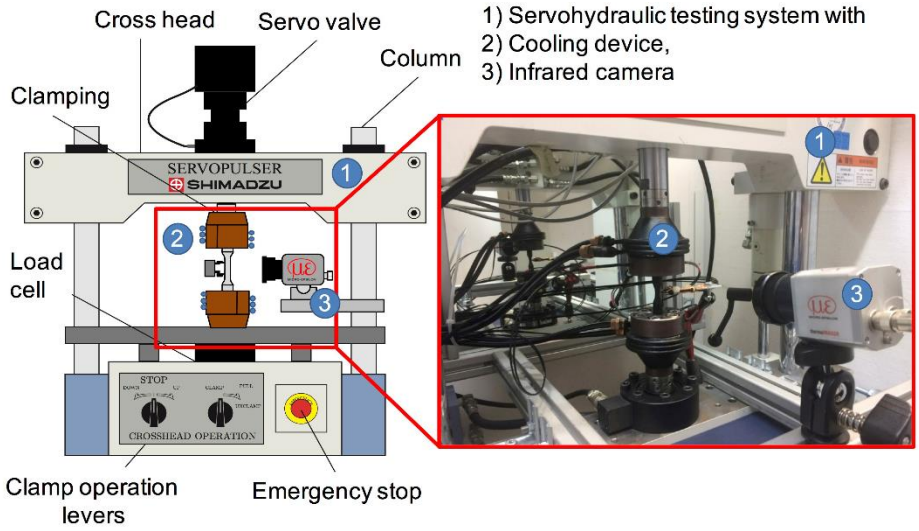

Fig. 1. Experimental setup with servo-hydraulic fatigue test system and thermographic measurement [32].

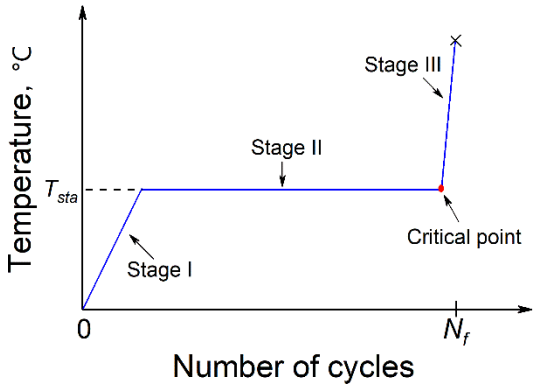

Fig. 2. Schematic representation of the temperature evolution process during a single loading stage.

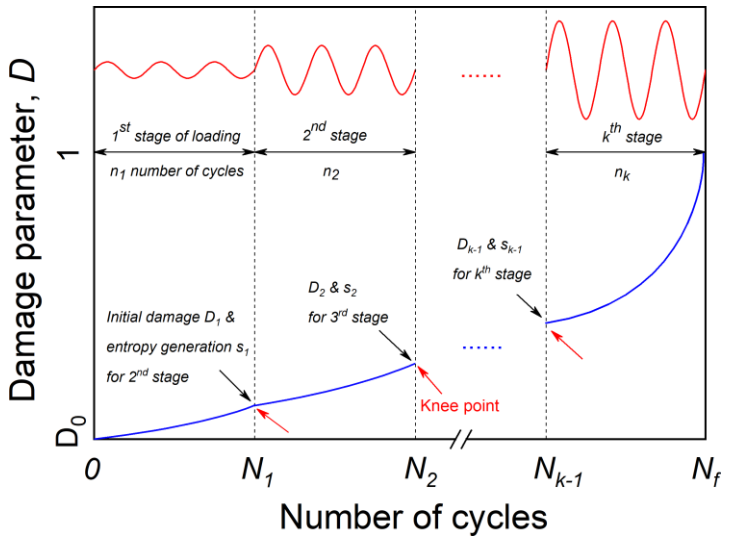

Fig. 3. Schematic of damage accumulation vs. number of cycles during load increase tests.

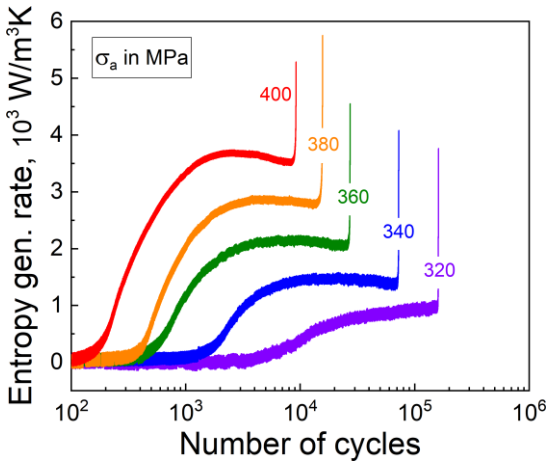

Fig. 4. Entropy generation rate vs. the number of cycles in the constant amplitude tests.

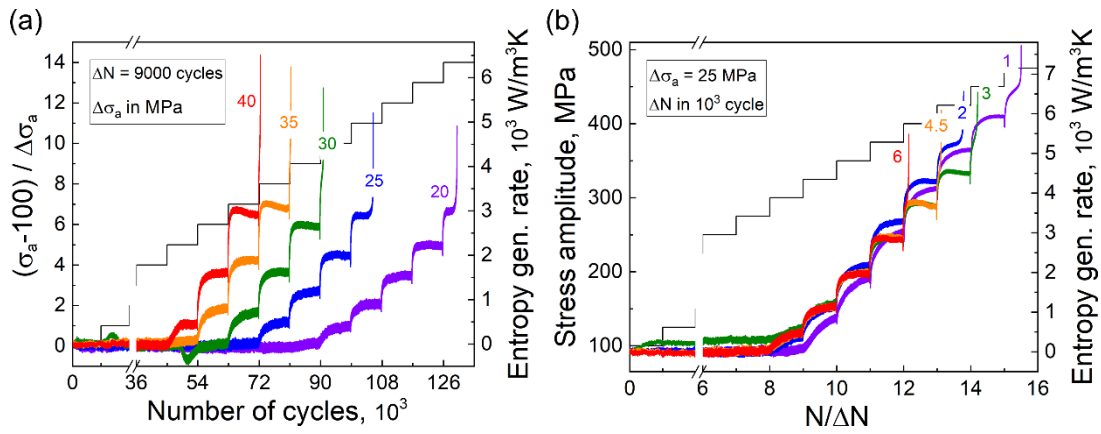

Fig. 5. Entropy generation rate and stress amplitude vs. the number of cycles of load increase tests: (a) in constant loading step length; (b) in constant load increments.

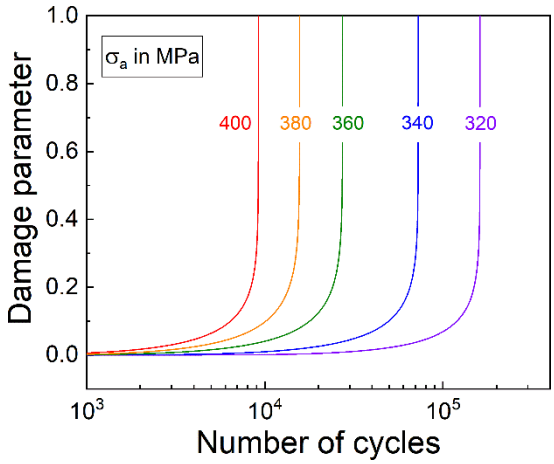

Fig. 6. Damage parameter vs. the number of cycles of constant amplitude tests.

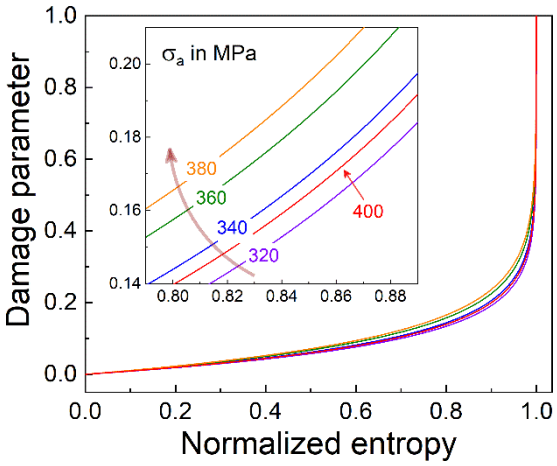

Fig. 7. Damage parameter vs. normalized entropy of constant amplitude tests.

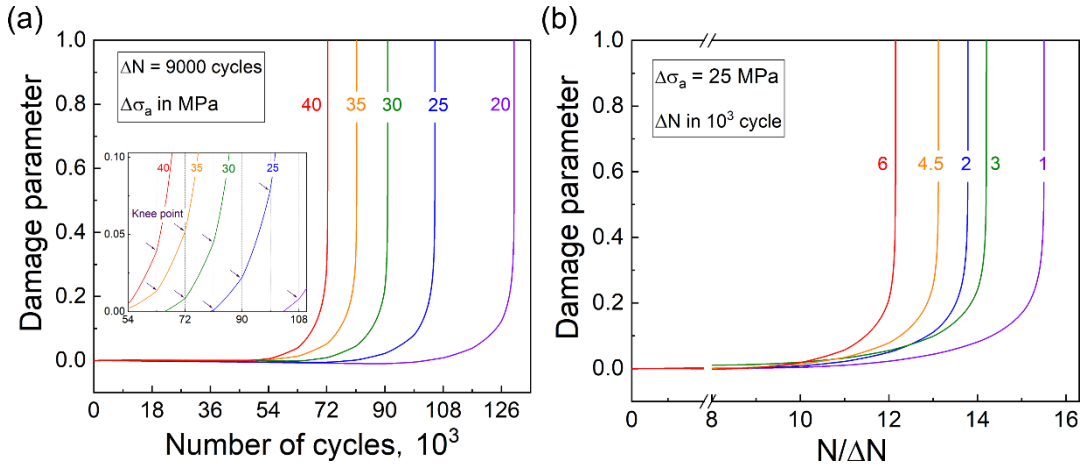

Fig. 8. Damage parameter vs. the number of cycles of the load increase tests: (a) in constant loading step length; (b) in constant load increments.

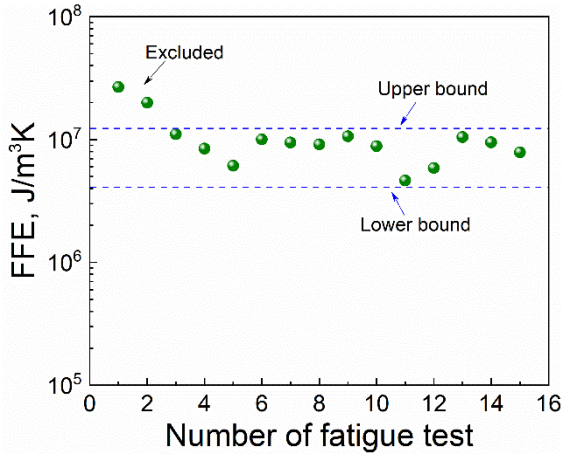

Fig. 9. The values of fatigue fracture entropy of SAE 1045 steel.

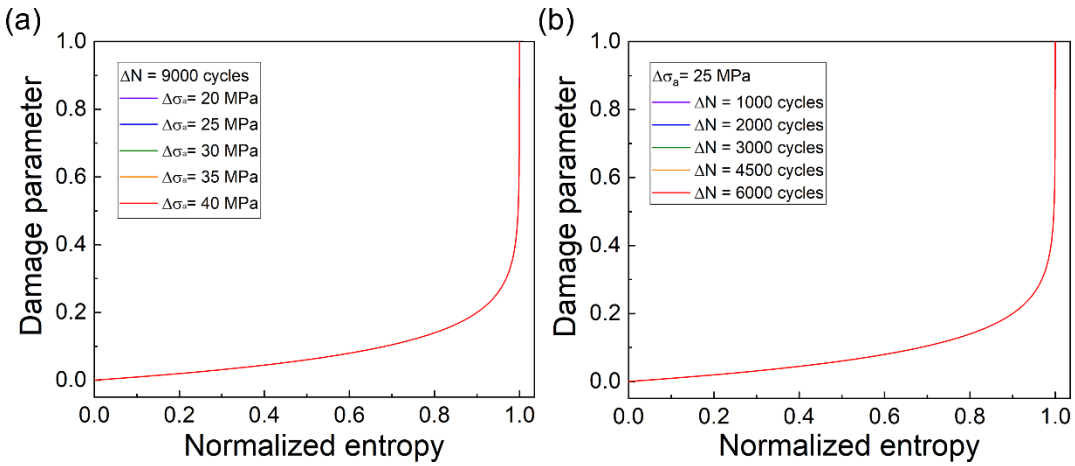

Fig. 10. Damage parameter vs. normalized entropy of load increase tests: (a) in constant loading step length; (b) in constant load increments.

PAPER 4

Characterization of the fatigue behaviour for SAE 1045 steel without and with load-free sequences based on non-destructive, X-ray diffraction and transmission electron microscopic investigations

H. Wu*, T. Bill, Z.J. Teng, S. Pramanik, K.-P. Hoyer, M. Schaper, P. Starke

Mater Sci Eng A, 2020; 794: 139597. DOI: 10.1016/j.msea.2020.139597

Copyright:

The following part is reproduced with permission from (2020) Elsevier B.V.

Characterization of the fatigue behavior for SAE 1045 steel without and with load-free sequences based on non-destructive, X-ray diffraction and transmission electron microscopic investigations

H. Wu [a, b, *], T. Bill [a], Z.J. Teng [a, b], S. Pramanik [c], K.-P. Hoyer [c], M. Schaper [c], P. Starke [a]

[a] *Department of Materials Science and Materials Testing, University of Applied Sciences Kaiserslautern, Schoenstr. 11, 67659, Kaiserslautern, Germany*

[b] *Chair of Non-Destructive Testing and Quality Assurance, Saarland University, Am Markt, Zeile 4, 66125, Saarbrücken, Germany*

[c] *Chair of Materials Science, Paderborn University, Warburger Strasse 100, 33100, Paderborn, Germany*

Abstract

The change of mechanical stress-strain-hysteresis and different physical parameters during fatigue tests have been measured to demonstrate the fatigue behavior and damage evolution processes of metallic materials. The electrical resistance e.g., can provide important information regarding the microstructural alteration by indicating the development of dislocation density. The states of such parameters of a fatigue specimen in a load-free sequence can represent the state of a component with a defined cyclic loading history. Therefore, conventional techniques measuring these parameters of common fatigue tests or even of service load tests with additional load-free sequences should have the application potential of remaining service life estimation and must be experimentally validated. In the scope of this paper, characteristic cycle-dependent changes of diverse physical parameters of fatigue specimens made from normalized SAE 1045 steel were determined and correlated with the residual stress state and dislocation density quantified by X-ray diffraction (XRD) and transmission electron microscopy (TEM) respectively.

Keywords: Fatigue behavior; Load-free sequence; Thermography; Electrical resistance measurement; TEM; XRD

1. Introduction

For a suitable dimensioning and material selection, the understanding of the cyclic deformation behavior is fundamental for reliable and economical operation of fatigue-loaded components. The underlying mechanisms are very closely linked to the present microstructure characterized by the complexity of the interrelated processes within the fatigued material volume. Cyclic loadings cause micro- and microplastic deformation of metallic materials, while characteristic dislocation structures and deformation properties are formed during cyclic softening and hardening processes. It is the initial point for fatigue, which will consequently lead to failure and eventually the fracture of the component in service, if the applied load level is beyond a critical threshold value.

From the conventional point of view, changes in the mechanical behavior under stress-controlled fatigue loading are in general characterized by the evolution of the plastic strain amplitude $\varepsilon_{a,p}$ [1,2]. Hence, they are expressed as a function of the number of cycles N and providing so-called cyclic deformation curves. For the fatigue experiments within this work, the change in temperature ΔT [3–5] and the change in electrical resistance ΔR [6–9] are determined from additional non-destructive measurement technologies with high accuracy. The electrical resistance mentioned within this paper is measured just for the test section in the middle of the fatigue specimen, where the most microscopic changes take place in the whole volume of the bulk material. It depends on the specimen geometry as well as on the material-dependent resistivity ρ_{Total}, which changes during plastic deformation due to variations in defect, i.e., predominantly the changes in dislocation structure and density in the first fatigue state up to 15% of the lifetime. Within that range, no micro-crack formation or propagation takes place. It is therefore the motivation and also the focus of this work, to look closely at the correlation between the macroscopic change in electrical resistance and the changes taken place on the microscopic scale. A DC-based electrical resistance measurement has been applied for evaluating progressive fatigue damage [10,11]. Especially the potential drop measurement is an established method to characterize the fatigue crack growth behavior [12]. In contrast to the method presented within the scope of this paper, the former methods of measuring electrical resistance were mostly aimed at the crack-related change in specimen geometry (remaining cross-section area) but not at the damage-related change in the microstructure of the material,

although the interpretation of the measurement curves requires generally other considerations [13]. Methods for measuring the change in electrical resistance are also suitable for continuous application to complex components in load-free sequences referring to condition monitoring.

Referring to the microscopic damage characterization, dislocations can be observed by means of etch pit, X-ray diffraction or transmission electron microscopy (TEM) [14], but they do not provide an accurate spatial distribution of the depicted dislocations. Thus, formation of dislocation cell boundaries and micro-bands in deformed steel cannot be detected using the former two techniques. In this regard, TEM provides the highest spatial resolution for the characterization of dislocations. Multiple measurements are needed for a statistically significant result, as only a local sample area is analyzed.

During TEM measurements, thin samples (with a thickness of approx. 100 nm) are exposed to a high-energy electron beam (200 keV). Due to the strain field associated with dislocations, lattice planes are locally bent. The bending decreases for an increasing distance from dislocations. Depending on the diffraction condition from the bent planes, a diffracted beam with a dark contrast can be formed. Therefore, dislocations appear as dark lines in a bright field TEM image [15]. The width of the dark contrast is related to the strain field of the dislocations. Based on this, the observation of dislocation networks and pileups at boundaries can be performed by using TEM [14]. Quantitative information such as the Burgers vector and the slip plane of dislocations can be obtained. By analyzing the TEM images, the dislocation density, i.e., the number of dislocations per unit area or the length of dislocation lines per unit volume, can also be calculated.

Thin samples could be troublesome, since they are mostly bent and show therefore high internal stress. On the other hand, comparably thick samples would show a dark contrast [16]. Because the sample thickness affects the dislocation density measurements. The sample thickness needs to be measured accurately. The foil thickness can be determined in a TEM using a wedge sample, convergent beam electron diffraction (CBED), electron energy loss spectroscopy or the projection of inclined stacking faults [17]. However, there are certain drawbacks in applying these techniques.

If the region of interest (ROI) does not show any formation of bend contours, the sample thickness cannot be determined by using a wedge sample. Also, the error involved in thickness calculation using the CBED technique is approx. 10% under certain condition [18].

2. Material, specimen geometry and methods

2.1. Material and specimen geometry

The material investigated is SAE 1045 (C45E) steel, which is in accordance to DIN EN 10083–2:2006–10 [19]. The raw material was delivered as round bars with a length of 5000 mm, a diameter of 20 mm and a scaly surface due to the heat treatment, which was performed by the manufacturer. The steel experiences at first an austenitisation at 850 ◦C, which is followed by a controlled slow cooling to ambient temperature, with the aim to obtain an almost ferritic-pearlitic microstructure, which is as depicted in Fig. 1a. In the micrograph, ferrite is displayed in light gray and represents about 50% of the displayed microstructure. Pearlite occurs near the ferrite regions in-between the cementite lamellas (black).

The hourglass-shaped specimen geometry, which applied identically for all fatigue tests, is shown in Fig. 1b. The surface of the test section is polished and the roughness afterwards could be determined as R_a = 0.25 µm and R_z = 5.99 µm by a confocal microscope (Smartproof 5, company Zeiss).

The SAE 1045 (C45E) steel in the normalized condition is a ductile material and exhibits a Brinell hardness of 210 HB. The chemical composition from the manufacturer's report in comparison with DIN EN 10083-2 is summarized in Table 1, the mechanical and quasi-static properties are summarized in Table 2.

2.2. Fatigue testing system and test procedures

All tests were performed at laboratory ambient conditions and room temperature (RT) with a servo-hydraulic testing system (EHF-U, company Shimadzu). The load capacity of the servo-hydraulic testing system is ±50 kN and the applied load cell allows to measure in force with an accuracy of ±0.5% of the nominal load range. One load increase test (LIT) and several constant amplitude tests (CAT) were conducted stress-

controlled with a constant stress ratio of R = -1, a test frequency of f = 5 Hz and a sinusoidal load-time function. The total fracture of the fatigue specimen or an ultimate number of cycles N_{max} = 2 × 106 was defined for the stop criterion. In case of total fracture, the number of cycles would be counted as N_f. The procedure of the LIT is determined as starting at a stress amplitude of $\sigma_{a,start}$ = 100 MPa with a stepwise increase of $\Delta\sigma_a$ = 20 MPa after every $\Delta N = 9 \times 10^3$ cycles until specimen fracture.

Fig. 2 shows schematically the different experimental procedures. In addition to LIT and CATs, one CAT with load-free sequences (σ_a = 0 MPa) were carried out to evaluate measured values load- and temperature-independently, in order to characterize the intermediate damage state as it was done for railway wheel steel [11]. The result of a LIT describes the cyclic stress-strain behavior and can be used to estimate the fatigue limit at the same time with only one single test. The stress amplitude starts with a significantly low value and is increased each time after a certain number of cycles is reached.

Within the scope of this paper, M can represent the plastic strain amplitude $\varepsilon_{a,p}$, the change in temperature ΔT or the change in electrical resistance ΔR of the specimen, respectively, which were continuously and simultaneously measured during fatigue tests. For strain measurements, an extensometer (Dynastrain, company Shimadzu) was fixed to the specimen's gauge length. To prevent leakage of electric current through the machine frame during the electrical resistance measurement, the grips were electrically isolated.

The characterization of the fatigue behavior is based on measurement data from mechanical stress-strain hysteresis, quantitative thermography and particularly resistance measurement using a test setup shown in Fig. 3 [20,21].

2.3. Quantitative thermography

The change in temperature was measured via an infrared camera (thermoIMAGER TIM 450, company Micro-Epsilon). This system provides a spectral range of 7.5 µm–13 µm, an optical resolution of 382 pixels × 288 pixels and a thermal sensitivity of min. 40 mK. The data was acquired by the supplied software. For the temperature measurements, three ROIs of 10 pixels × 10 pixels were defined along with the specimen in certain

pixel positions in the field of view (FOV) of the IR-camera: one in the middle of the gauge length (T_1) and two at each shaft (T_2 and T_3). The cross-sectional area of the shafts is much bigger than that of the gauge length. Due to this, temperatures on the shaft are subtracted from the temperature in the middle of the specimen, in order to eliminate the influences caused by the elastic portion and the surrounding. The change in temperature was calculated according to following equation:

$$\Delta T = T_1 - 0.5 \cdot (T_2 + T_3) \quad (1)$$

Due to the push-pull fatigue loading without mean stress (R = -1), there is only a negligible elongation of the specimen during the fatigue test and the effects from the transverse strain was neglected.

The reasonableness of the application of quantitative thermography in fatigue behavior characterization can be derived from the consideration of the stress-strain hysteresis loop. The enclosed area of a single hysteresis loop describes the energy from plastic deformation per cycle per unit volume of the specimen [22], which will be transformed into other kinds of energy [4,23–25]. Thus, microstructural changes such as dislocation reactions, micro- and macro-cracking and their propagation can be activated. The predominant proportion of about 90%–95% of the deformation energy turns into heat dissipation, which is the reason why the temperature change can be correlated directly with the plastic deformation or the cumulative damage [26]. In general, for metallic materials, the dissipated energy can be characterized easily by measuring the change in temperature on the specimen surface, since the thermal conductivity is mostly quite high.

For the temperature measurement, all specimens were sprayed with a matt black paint, obtaining an emission factor of ~0.97 on the surface of the specimen. Since the maximum temperature change occurring during the tests was only approx. 13 K, the change in the emissivity during fatigue tests can be neglected. For the sake of thermal stability as well as the accuracy during long durations of the experiments, the infrared camera system has been improved by an active cooling system (Fig. 3, detail 3).

In addition, to stabilize the temperature of specimen grips, a separate cooling system based on Peltier-elements with liquid coolant was developed, which is an essential

precondition for using sensitive thermometric techniques.

2.4. Resistometry

For highly sensitive resistance measurements, the specimen was subjected to a direct current of I = 3 A and the electrical resistance R of the test section was accurately measured by applying the common four-point technique [27]. The DC is supplied via a pair of copper electrodes on the shafts of the fatigue specimens. The voltage across the test section is picked up through two wires, which are attached closely to the edges of the shafts at Ø12, by a highly sensitive 24-bit data acquisition card. The R value can be then calculated with the known current value according to the Ohm's law. Besides negligible geometry-changes under mean stress-free loading, the electrical resistance R and its change ΔR before micro-crack initiation and macro-crack propagation depend exclusively on the specific electrical resistance ρ_{Total}, which is a function of deformation-induced microstructural changes. The following equation reveals the relationship between the electrical resistance and the specific electrical resistance:

$$R = \rho_{Total} \cdot \frac{L}{A} \tag{2}$$

Where L and A are the length and the cross-sectional area, respectively, of the test piece.

According to the Matthiessen's rule [28], ρ_{Total} consists of at least 2 terms described as ρ_0 and ρ_{Ideal}, where ρ_0 is nominally temperature-independent, determined by the internal defect structure such as the concentration and distribution of dislocations, impurities, vacancies and grain boundaries, while ρ_{Ideal} is highly temperature-dependent:

$$\rho_{Total} = \rho_0 + \rho_{Ideal}(T) \tag{3}$$

If the temperature is stabilized, it can be assumed that ρ_{Total} is only dependent on ρ0, i.e., the internal defects. Micro-cracks result in material separation, as well as the reduction of the effective specimen cross-section, increase additionally the electrical resistance of the investigated volume.

2.5. XRD

X-ray diffraction (XRD) investigation is primarily used for phase analysis and

residual stress evaluation of crystalline materials. Residual stresses of a component or a specimen can be influenced e.g., by manufacturing processes as well as by mechanical load and can, therefore, indicate their durability.

The diffraction of the incident X-ray occurs, when the spacings of the crystal lattice planes are in the same order of the wavelength, which is in the range of 0.01 nm–10 nm, corresponding the case of crystalline materials. Due to the 3-dimensional lattice structure, a spatial diffraction grating is generated. The X-rays are diffracted under the Bragg angle θ at the electron shells of the irradiated atoms, whereby the diffracted waves interfere with each other. Depending on the distances between the atoms, diffracted waves have different path differences. At which angel a constructive or a destructive interference occurs, depends therefore on the distances between the atoms. Depending on the angular position for constructive interference, micro-strains can be determined, which in turn are used to evaluate the residual stresses in the crystalline metallic material.

For the evaluation of the load- and cycle-dependent change of residual stresses near to the surface, X-ray measurements were performed by using a diffractometer type Seifert XRD 3000 PTS with a primary Cr-Kα-beam having a diameter of 150 µm. The scanning range of 2θ (between the incident and the reflected beam) was set to angles between 148◦ to 162◦ to measure interferences at the {211} plane, were 2θ is 156.08◦ for a residual stress-free condition according to PDF-2 2016 Database Version 2.1603 [29]. For compression (tension) residual stresses, the interference peak is shifted to lower (higher) 2θ values. To consider different grain orientations, the specimen was tilted stepwise by 29 increments for Ψ angles in the range from -45◦ to +45◦ during the measurement. For the distribution of line positions, 2θ values are plotted vs. sin2 Ψ in equidistant increments. Based on this relationship and depending on the focus or cross-correlation method, the X-ray software calculates the residual stress values [30].

2.6. TEM

For TEM investigations, specimens were machined out from the gauge lengths of the fatigue specimens. Using focused ion beam (FIB) milling, thin lamellae of 2.7 µm × 6.7 µm (w × l) were prepared. All TEM measurements were conducted with a cold field emission gun (JEMARM 200F, company JOEL) equipped with a hexapole Cs corrector

(ASCOR). By using this type of TEM, dislocations can be observed when the sample is aligned in a specific position concerning the incident electron beam. For realising this arrangement, the sample is tilted using a double tilt holder.

A TEM-based dislocation density study is difficult to conduct for C45E steel because of its ferromagnetism, so that the objective lens astigmatism needs to be corrected [16] for different sample tilting positions. Progressing fatigue cycles lead to the formation of dislocations which create in turn internal stress fields. The stress fields lead further to the formation of diffuse Kikuchi diffraction pattern lines. Therefore, achieving the two-beam diffraction contrast condition for imaging dislocations becomes troublesome [16]. Furthermore, the two-beam diffraction contrast needs to be evaluated from each micro-grain. Due to the limitation of the maximum tilt angle in a TEM, the two-beam condition can only be achieved in a small number of grains. This results in the evaluation of a small sample area.

The local sample thickness was calculated by using energy-filtered transmission electron microscopy (EFTEM). In this regard, by measuring the local energy loss in EFTEM, the thickness to mean free path ratio (t/λ) maps are acquired by using (i) the zero-energy loss peak and (ii) the whole energy loss spectrum. Five t/λ maps were captured for samples in different fatigue conditions of the SAE 1045 (C45E) steel. The mean free path was calculated from the sample composition by using Digital Micrograph script [31]. The Digital Micrograph script is based on the model given in Ref. [32]. The mean free path λ of the SAE 1045 steel was calculated to be 110.5 nm. Thus, the sample thickness was obtained using Eq. (4) [33].

$$t = \lambda \cdot \ln (I_t/I_0) \tag{4}$$

In equation (4), t is the sample thickness (nm), λ is the mean free path (nm), It is the total area of the energy loss spectrum (nm^2) and I_0 is the area under the zero-loss peak (nm^2). The zero-loss peak was estimated with a filter of width 10 eV. The mean sample thickness varied approximately between 160 nm and 350 nm for all specimens.

For measuring the dislocation density, a square grid containing equally spaced horizontal and vertical lines was drawn on the TEM micrograph. The total length of all the horizontal and vertical lines in the square grid L was determined. The total

intersection points of the horizontal and vertical lines with dislocations were counted as N, while the intersection points with the grain boundaries were disregarded. Afterwards, the dislocation density was calculated using equation (5) [34].

$$\rho = 2N/(L \cdot t) \tag{5}$$

where ρ is the dislocation density (m-1) and t is the local sample thickness (m).

3. Results and discussions

In Fig. 4, ΔT calculated according to equation (1) during the LIT is plotted beside σa versus the number of cycles. From σ_a = 280 MPa (N = 81 × 10^3) on, there is a slight change in the ΔT-N-slope indicating the first micro-plastic deformations (Fig. 4, detail). Based on this result, the fatigue limit (stress amplitude at transition) can be estimated with a value between σ_a = 280 MPa and 300 MPa agreeing very well with the transition to the fatigue strength of normalized SAE 1045 (C45E) steel evaluated in a conventional manner [35].

After the LIT, CATs were performed to validate the results of the LIT regarding the estimation of the fatigue limit and to acquire data for further fatigue life calculation methods (e.g., PhyBaL [36], StressLife [37], StrainLife [38]), which are less relevant to the purpose of this paper. Furthermore, the progress of different material responses measured simultaneously can be compared.

Fig. 5 proves that the progress of ΔT (Fig. 5b) is in good accordance with the results from conventional strain measurements using $\varepsilon_{a,p}$ (Fig. 5a). CATs at 320 MPa and 380 MPa were repeated once respectively, resulting in very similar courses of the measurands with only slightly change of N_f and the maximum of ΔT after the first cyclic softening, which can be explained by normal scattering of the material.

The cyclic deformation behaviour under different stress amplitudes is characterized for both measurands, $\varepsilon_{a,p}$ and ΔT, by the varying incubation intervals respectively, where the measurands are close to zero until the first cyclic softening coming up with obviously increasing $\varepsilon_{a,p}$ and ΔT values. After reaching the cyclic softening maximum, cyclic hardening process leads to decreasing measurand values until shortly before the final failure. The macroscopic crack formation and propagation leads to fictive

secondary cyclic softening. It can be seen from Fig. 5, that the cyclic deformation behavior can be equivalently described through measurands derived from mechanical stress-strain hysteresis as well as temperature measurements. This can be traced back to the common physical background of both methods and the related cross-effects described in the paragraph 2.3.

This finding is stated with the result of linear regression shown in Fig. 6, where ΔT and $\varepsilon_{a,p}$ values from the same CAT are compared at identical, logarithmically counted cycles (N = 1, 2, …, 10, 20, …, 100, 200, …1000, 2000, …), namely for all 6 conducted tests. From this diagram, it can be seen clearly that there is a reliable linear correlation between the two quantities with a high compliance factor (R2), independent from the load level of the CAT performed.

For the validation of the applied test strategy with load-free pauses as presented in Fig. 2c, CATs at σ_a = 343 MPa until a certain percentage of the estimated N_f are conducted, according to the S–N-curve calculation based on the results shown in Fig. 5. Here the values are determined as 5%, 15% and 50% of the number of cycles at specimen fracture. Besides ΔT and $\varepsilon_{a,p}$, the change in electrical resistance ΔR (averaged over several cycles) was also measured and calculated in this case, as shown in Fig. 7. It is to be seen at first, that all three measured parameters show congruent courses. Features of these curves like the length of the incubation phase, the cyclic softening and hardening effect are almost identical to the results of the CAT conducted under a very closed stress amplitude of 340 MPa (Fig. 5, green curves). While the values of the curves from the CAT stopped at 5% N_f are still increasing due to cyclic softening, at 15% N_f, all three measurands reach here almost the maxima of the curves. A tiny fallback can be observed at the end of the curves from the CAT until 50% N_f, since the test located then in the state of cyclic hardening.

Furthermore, there is indeed a different behavior of ΔR. Unlike ΔT and $\varepsilon_{a,p}$ with the typical “s-shape” increasing behavior during the cyclic softening, the courses show different linear-like increments in ΔR. This is a clear indication, that the change in ΔR is not totally depended on the temperature as it was already stated before.

Following the test strategy shown in Fig. 2c, a CAT with load-free (σ_a = 0 MPa) sequences having the same holding time of 1800 s was performed, in order to determine

the change in electrical resistance $\Delta R_{load-free}$ at $\Delta T = 0$ K [11], so that $\Delta R_{load-free}$ can be determined without any temperature influence. The CAT was hold load-free when the incubation interval (100 cycles), as well as the 5%, 15% and 50% of N_f, are reached respectively. The change in electrical resistance detected in an unloaded condition, therefore, provides reproducible results on the proceeding fatigue damage due to increasing defect density and is virtually unaffected by phonons, which is in accordance to Matthiessen's rule [28].

Fig. 8 summarizes the results of ΔT and ΔR changing after the test time. The applied measurement methods are equally suitable for fatigue assessment. Within the incubation phase of 100 cycles, the both parameters show minimal changes. It is also hardly to see due to the short loading duration on the time axis with a unit of hour. After each load-free sequence, the last values of the previous loading sequence are "recovered" again with the same manner of the increment. The values and the increasing manner of the curves from the single CAT with pauses are almost identical, comparing to the results obtained from different CATs as shown in Fig. 7. This is an evidence, that the measured physical values are exclusively dependent on the applied loading but not affected by the load-free sequences. Therefore, the applied test strategy can lead to comparable results for CATs until the same phase of fatigue life, as demonstrated in Fig. 7.

The detail, that the first significant raise of the both curves are slightly different, can be observed in Fig. 8, too, as already mentioned for Fig. 7: While the slope of the raising part of the ΔR-Time-curve keeps almost constantly linear, the course of ΔT-Time has a special "s-shape". A maximum change in temperature of 5.38 K and a maximum change in electrical resistance of 5.12 μΩ are noted at the stage of maximum cyclic softening after 15% N_f at t = 1.5 h, respectively. Decreasing ΔT and ΔR values due to cyclic hardening in the fourth cyclic loading section can also be seen, as already confirmed from the results of CAT until 50% N_f shown in Fig. 7.

The specimen of the single CAT with pauses was neither for TEM sample preparation nor for investigations with in-situ TEM considered. Therefore, for TEM analysis, the three different CAT specimens from Fig. 7 along with one more specimen in an undeformed state as reference are used. These samples were also used for the

XRD measurements furtherly.

In Fig. 9a and b, the TEM results reveal the presence of ferrite (pointed out by light blue arrows) and cementite (dark red arrows). Cementite is observed to form an elongated lamellar morphology. The interlamellar spacing between cementite varies between 250 nm – 370 nm. The width of the cementite lamellae is 48 nm. A dark contrast due to dislocations can be noticed as well. In addition, Fig. 9b displays dislocations between two lamellas of cementite (red arrows). In the initial state (N = 0 cycles), a homogeneous dislocation distribution (yellow arrows) occurs in ferrite (Fig. 9c). Here, the dislocation lines appear intertwined. The dark contrast is either due to the strain field of the surrounding dislocations or diffraction contrast. In Fig. 9d, fatigue cycling to 5% N_f leads to a parallel array arrangement of the present dislocations. Moreover, in Fig. 9e, representing the point of maximum cyclic softening (N ≈ 15% N_f), elongated dislocations are observed, which is typical for normalized SAE 1045 steel. The dislocation contrast increases from 0% to 15% N_f. A fatigue loading up to 50% N_f leads to significant changes in both the dislocation arrangement and the dislocation density (Fig. 9f). Here, the dislocations (pointed out by yellow arrows) can be found to be isolated from each other. In addition, an apparent decrease in the dislocation density is noted.

In contrast to earlier investigations, e.g., Ref. [11], only the formation of dislocation walls but not dislocation cells were observed during fatigue loading. This can be explained by the fact that the stress amplitude with σ_a = 343 MPa is comparatively low and no sufficiently high wavy sliding behavior is obtained with regard to the dislocation movement.

The dislocation structure in combination with residual stress measurements indicates significant influences on the specific electrical resistance ρ_{Total}, which is directly linked to the electrical resistance. In view of the above, Fig. 10 summarizes the individual behaviour of all microstructure-related parameters determined from each measurement in different fatigue stages. The dislocation density ρ and the residual stress σ_{ES} were measured on CAT specimens until certain stages of the estimated fatigue life. The change in electrical resistance $\Delta R_{load\text{-}free}$ was calculated by averaging the ΔR values measured during the stable load-free period (Fig. 8). Until 15% N_f, all the three

parameters (electrical resistance, residual stress, and dislocation density) increase monotonously. Thereafter, all three parameters drop on different scales. At 50% N_f the σ_{ES} drops to a value similar to the original state. The $\Delta R_{load\text{-}free}$ value falls to a value in between it is measured for 0% and 15% N_f. The ρ decreases slightly from its estimated maximum at 15% N_f.

In the end, Fig. 11 shows the relation between the three parameters in detail. Besides the initial state (N = 0% N_f), pairs of values are specified for the state of pure cyclic softening (N = 5% N_f), for the beginning of cyclic hardening (N = 15% N_f) and in the saturation state (N = 50% N_f), connected with trend lines for the ρ-$\Delta R_{load\text{-}free}$ and σ_{ES}-$\Delta R_{load\text{-}free}$ data-pairs. Up to a fatigued state of 15% Nf, the change of the both values follow the increasing $\Delta R_{load\text{-}free}$ similarly in the positive direction, but not in a monotonous linear manner. Hereby the $\Delta R_{load\text{-}free}$ value increases up to 2.6 μΩ. Afterwards, all three values drop at 50% N_f, but differently. The $\Delta R_{load\text{-}free}$ falls more than 50% back to 1.1 μΩ, which is slightly lower than it was at 5% N_f, while ρ reduces only back to a level somewhat lower than the maximum at 15% N_f. σ_{ES} falls on the contrary completely back to the initial state, since the formation of microcracks releases the local residual stress.

Consequently, different microstructural mechanisms dominate the increasing change in the electrical resistance depending on the fatigue state. It can be assumed that up to 5% N_f, the increasing dislocation density is responsible for the comparatively slight increase in the change in electrical resistance. For N ≤ 50% N_f, micro-crack formation and propagation are decisive for the sharp decrease in the change in electrical resistance [11]. As a consequence of the progressive microcrack propagation and accumulation in the range of 15%–50% N_f, stresses in the microstructure are released, which causes the obvious drop of the residual stress value. This is also, but not exclusively, associated with a reduction in dislocation density, although its drop is not proportional to the change of residual stress.

4. Conclusions

In this paper, investigations by means of non-destructive testing (quantitative thermography, strain, and electrical resistance measurement), XRD and TEM were carried out to characterize the fatigue behavior of SAE 1045 steel. The potential of LIT,

conventional CAT and CAT with load-free sequences were introduced. According to the simultaneously measured change in temperature, electrical resistance and plastic strain amplitude during the whole test procedures, similar behavior indicating the fatigue damage development can be determined, whereby little difference of the cycle-dependent changes between ΔR and ΔT (as well as $\varepsilon_{a,p}$) can be identified, providing an evidence for the more sensitive reliability on microscopic change of the electrical resistance measurement. It can be summarized, that the change in electrical resistance is well suited to characterize fatigue induced deformation and damage processes.

Further experiment strategies, which aim at introducing load-free sequences and stop criterion till certain stadium of fatigue life into conventional CATs, have revealed further correlations between the macroscopic ΔR and the microscopic parameters, like the residual stress σ_{ES} and the dislocation density ρ. The investigations on SAE 1045 (C45E) steel specimens have shown, that fatigue tests under the same stress amplitude, no matter with or without load-free sequences, have comparable fatigue progresses. With the occurring of cyclic hardening, ρ decreased for about only 14% from the maximum until the saturated state at 50% N_f, whereas the change in electrical resistance in load-free sequences $\Delta R_{load\text{-}free}$ was reduced by 58%. The TEM image taken from the sample without damage show intertwined dislocations, while other TEM graphs taken from samples fatigue loaded up to 15% N_f indicate an increasing dislocation contrast. A formation of parallel arrays of dislocations takes place in the sample fatigued until 5% N_f. In the sample which has experienced the stage of maximum cyclic softening (15% N_f), elongated dislocations are observed. These dislocations become isolated in the 50% N_f-sample. Therefore, as proven by TEM investigations, changes of the dislocation structure e.g., decreasing cell diameters take place in this range of the number of cycles, where the distance and the possibility of dislocation movement are limited. As the formation and propagation of micro-cracks are intensified, $\Delta R_{load\text{-}free}$ depict the defect density of the material integrally. Thus, the implementation of ΔR measurement in structural integrity inspection can be therefore expected, when the specimen is thermal stabilized and also in a load-free situation.

Declaration of competing interest

The authors declare that they have no known competing financial interests or

personal relationships that could have appeared to influence the work reported in this paper.

Acknowledgment

The authors from the Department of Materials Science and Materials Testing would like to thank the German Research Foundation (Deutsche Forschungsgemeinschaft DFG, STA 1133/6-1) and the University of Applied Sciences Kaiserslautern for the financial support of this research. They would also thank Shimadzu Europe/Germany and Micro-Epsilon for their support in technical equipment provision.

References

[1] Lukáš P, Klesnil M. Cyclic stress-strain response and fatigue life of metals in low amplitude region. Mater Sci Eng. 1973; 11:345-356.

[2] Bražėnas A, Vaičiulis D. Determination of fatigue curve parameters at cyclic strain limited loading according to the mechanical characteristics of power energy structural materials. Nucl Eng Des. 2011; 241:3596-3604.

[3] Curà F, Gallinatti AE, Sesana R. Dissipative aspects in thermographic methods. Fatigue Fract Eng M. 2012; 35:1133-1147.

[4] Meneghetti G, Ricotta M, Atzori B. A two-parameter, heat energy-based approach to analyse the mean stress influence on axial fatigue behaviour of plain steel specimens. Int J Fatigue. 2016; 82:60-70.

[5] Rigon D, Ricotta M, Meneghetti G. An analysis of the specific heat loss at the tip of severely notched stainless steel specimens to correlate the fatigue strength. Theor Appl Fract Mech. 2017; 92:240-251.

[6] Omari MA, Sevostianov I. Estimation of changes in the mechanical properties of stainless steel subjected to fatigue loading via electrical resistance monitoring. Int J Eng Sci. 2013; 65:40-48.

[7] Omari MA, Sevostianov I. Evaluation of the growth of dislocations density in fatigue loading process via electrical resistivity measurements. Int J Fract. 2013; 179:229-235.

[8] Glushko O, Cordill MJ. Electrical resistance of metal films on polymer substrates

under tension. Exp Tech. 2014; 40:303-310.

[9] Sun B, Yang L, Guo Y. A high-cycle fatigue accumulation model based on electrical resistance for structural steels. Fatigue Fract Eng M. 2007; 30:1052-1062.

[10] Charsley P, Robins BA. Electrical resistance changes of cyclically deformed copper. Mater Sci Eng A. 1974; 14:189-196.

[11] Starke P, Walther F, Eifler D. Model-based correlation between change of electrical resistance and change of dislocation density of fatigued-loaded ICE R7 wheel steel specimens. Mater. Test. 2018; 60:669-677.

[12] Gandossi L, Summers SA, Taylor NG, Hurst RC, Hulm BJ, Parker JD. The potential drop method for monitoring crack growth in real components subjected to combined fatigue and creep conditions: application of FE techniques for deriving calibration curves. Int J Pres Ves Pip. 2001; 78:881-891.

[13] Motz C, Friedl O, Pippan R. Fatigue crack propagation in cellular metals. Int J Fatigue. 2005; 27:1571-1581.

[14] Dieter GE, Bacon D. Mechanical metallurgy SI metric edition. London: McGraw-Hill Book Company. 1988.

[15] Hull D, Bacon DJ. Introduction to dislocations. Elsevier Ltd. 2011.

[16] Pešička J, Kužel R, Dronhofer A, Eggeler G. The evolution of dislocation density during heat treatment and creep of tempered martensite ferritic steels. Acta Mater. 2003; 51: 4847-4862.

[17] Zuo JM, Spence JCH. Electron Microdiffraction. Springer US.1992.

[18] LeBeau JM, Findlay SD, Allen LJ, Stemmer S. Position averaged convergent beam electron diffraction: theory and applications. Ultramicroscopy. 2010; 110:118-125.

[19] e.V. Din, Hrsg. Steels for quenching and tempering - Part 2: technical delivery conditions for non-alloy steels. German version EN 10083-2. 2006.

[20] Walther F, Eifler D. Fatigue life calculation of SAE1050 and SAE 1065 steel under random loading. Int J Fatigue. 2007; 29:1885-1892.

[21] Starke P, Walther F, Eifler D. Fatigue assessment and fatigue life calculation of

quenched and tempered SAE 4140 steel based on stress-strain hysteresis, temperature and electrical resistance measurements. Fatigue Fract Eng M. 2007; 30:1044-1051.

[22] Morrow JD. Cyclic Plastic Strain Energy and Fatigue of Metals.1964.

[23] Wu H, Baumchen A, Engel A, Acosta R, Boller C, Starke P. SteBLife - a new short-time procedure for the evaluation of fatigue data. Int J Fatigue. 2019; 124:82-88.

[24] Teng ZJ, Wu H, Boller C, Starke P. A unified fatigue life calculation based on intrinsic thermal dissipation and microplasticity evolution. Int J Fatigue. 2020; 131:105370.

[25] Teng ZJ, Wu H, Boller C, Starke P. Thermography in high cycle fatigue short-term evaluation procedures applied to a medium carbon steel. Fatigue Fract Eng M. 2020; 43:515-526.

[26] Piotrowski A, Eifler D. Bewertung zyklischer Verformungsvorg¨ange metallischer Werkstoffe mit Hilfe mechanischer, thermometrischer und elektrischer Meßverfahren. Mater Werkst. 1995; 26:121–127.

[27] Heaney MB. Electrical conductivity and resistivity. In book: Electrical Measurement, Signal Processing, and Displays. CRC Press. 2003

[28] Schwerer FC, Conroy JW, Arajs S. Matthiessen's rule and the electrical resistivity of iron-silicon solid solutions. J Phys Chem Solid. 1969; 30:1513-1525.

[29] Gates-Rector S, Blanton T. The Powder Diffraction File: a quality materials characterization database. Powder Diffr. Cambridge University Press. 2019.

[30] Hoffmann JE, Zgani M, Scholz D, Altendorfer M, Clemens H, Kübler R. X-ray residual stress analysis of nitrided low alloyed steels. Mater Test. 2012; 54(6):395-407.

[31] Mitchell DRG, Schaffer B. Scripting-customised microscopy tools for digital MicrographTM. Ultramicroscopy. 2005; 103:319-332.

[32] Iakoubovskii K, Mitsuishi K, Nakayama Y, Furuya K. Mean free path of inelastic electron scattering in elemental solids and oxides using transmission electron microscopy: atomic number dependent oscillatory behavior. Phys Rev B. 2008; 77:

104102.

[33] Egerton RF. An introduction to EELS. Electron Energy-Loss Spectrosc. Electron Microsc. Springer US, Boston, MA. 2011; 1–28.

[34] Hirsch PB. Electron Microscopy of Thin Crystals. Butterworths, 1965.

[35] Starke P, Wu H. Use of non-destructive testing methods in a new one-specimen test strategy for the estimation of fatigue data. Int J Fatigue. 2018; 111:177-185.

[36] Starke P, Walther F, Eifler D, PHYBAL – A new method for lifetime prediction based on strain, temperature and electrical measurements. Int J Fatigue. 2006; 28:1028-1036.

[37] Starke P. StressLife$_{tc}$ – NDT-related assessment of the fatigue life of metallic materials. Mater Test. 2019; 61:297-303.

[38] K. Heckmann, Sievers J, Schopf T, Schuler X, De Acosta R, Starke P, Boller C, Jamrozy M, Knyazeva M, Walther F. StrainLife: efficient fatigue life data generation for an enhanced ageing assessment of metallic components. V06BT06A073.

Table 1

Chemical composition of normalized SAE 1045 (C45E) steel.

(wt%)		C	Si	Mn	P	S	Cr	Mo	Ni
DIN [13]	min.	0.42	-	0.50	-	-	-	-	-
	max.	0.50	0.40	0.80	0.030	0.035	0.40	0.10	0.40
Manufacturer's report		0.47	0.23	0.72	0.012	0.013	0.06	0.014	0.07

Table 2

Mechanical and quasi-static properties of normalized SAE 1045 (C45E) steel.

Parameters	DIN [13]	Manufacturer's information
Yield strength $R_{p0.2}$ (MPa)	min. 305	413
Tensile strength R_m (MPa)	min. 580	710
Ultimate strain A (%)	min. 16	23.5
Notch impact strength KCU ($J \cdot cm^{-2}$)	-	56
Hardness (HB)	-	210

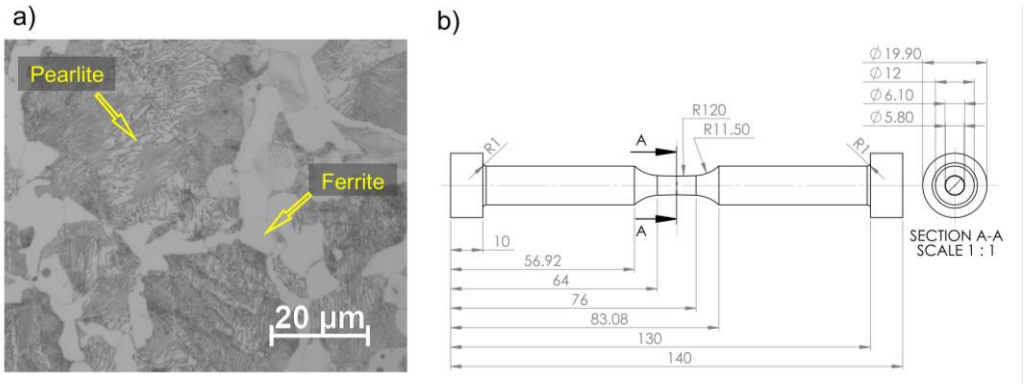

Fig. 1. (a) Ferritic-pearlitic microstructure of normalized SAE 1045 (C45E) steel; (b) hourglass-shaped fatigue specimen geometry.

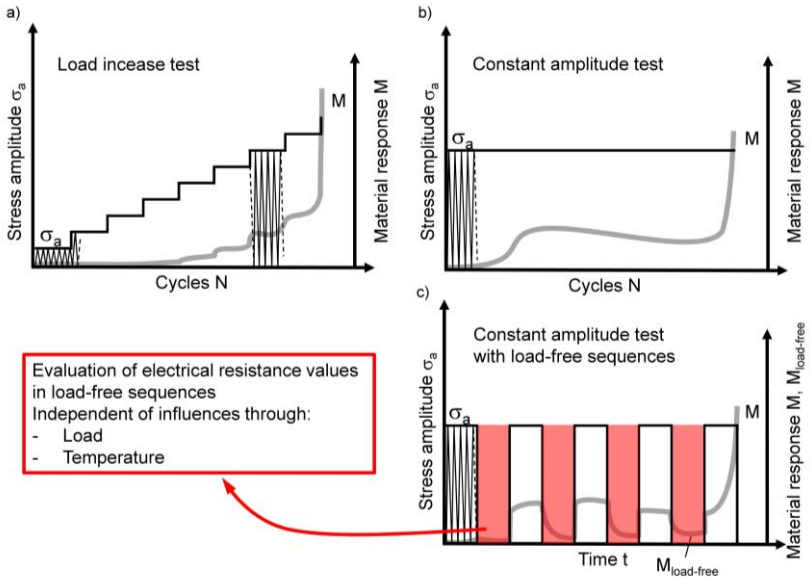

Fig. 2. Schematic representation of the experimental procedures, (a) LIT; (b) CAT; (c) CAT with load-free sequences, M represents the measured material response, i.e., different physical quantities.

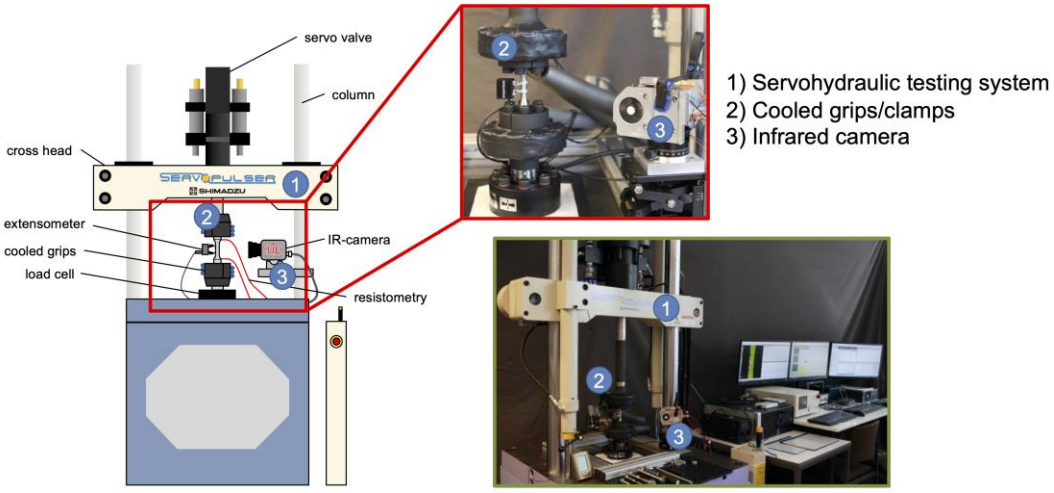

Fig. 3. Schematic illustration and photograph of the experimental setup for measurements of mechanical stress-strain hysteresis, temperature, and electrical resistance.

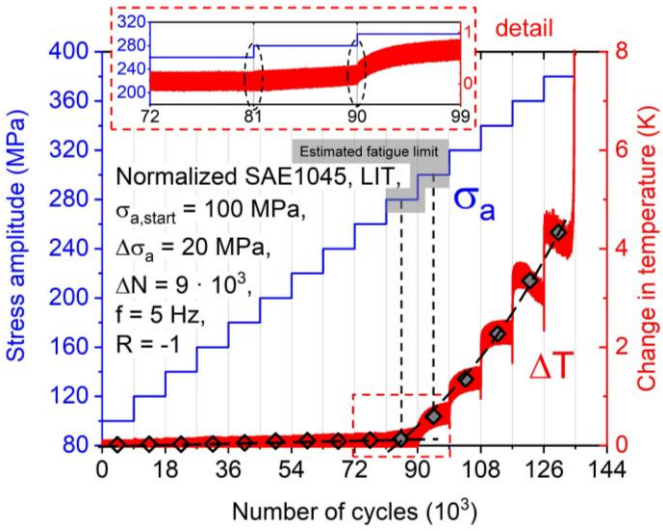

Fig. 4. Change in temperature and the stress amplitude versus the number of cycles of a LIT. The number of cycles is displayed linearly. The section of the estimated fatigue limit is shown in detail.

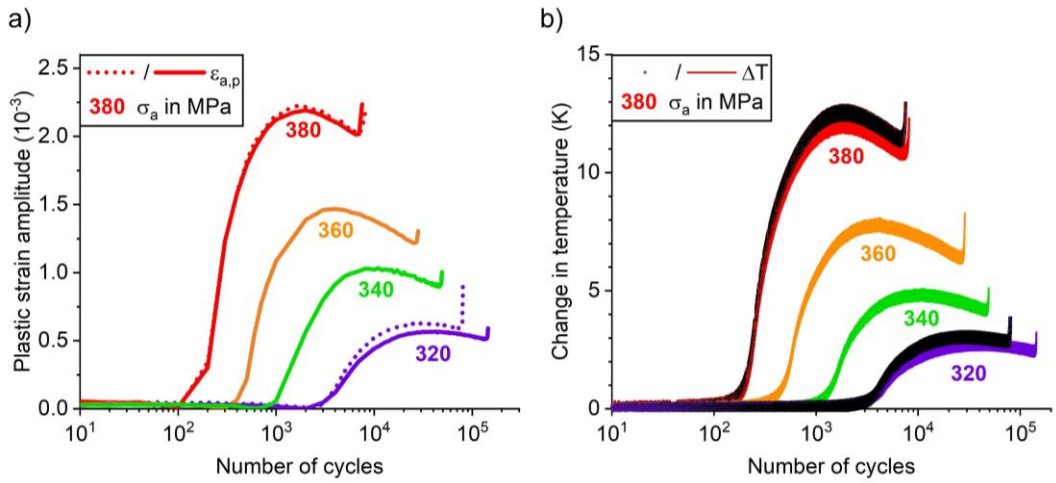

Fig. 5. Cyclic deformation curves based on the plastic strain amplitude (a) and the change in temperature (b) determined from constant amplitude tests for specimens of normalized SAE 1045 (C45E) steel. The number of cycles is displayed logarithmically.

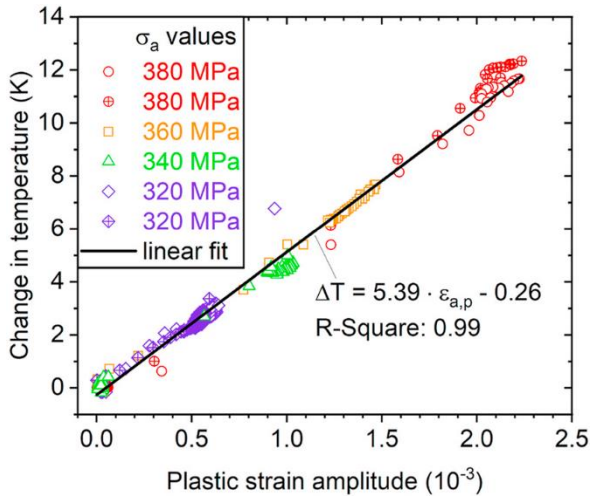

Fig. 6. Correlation between $\varepsilon_{a,p}$ and ΔT from different CATs shown in Fig. 5.

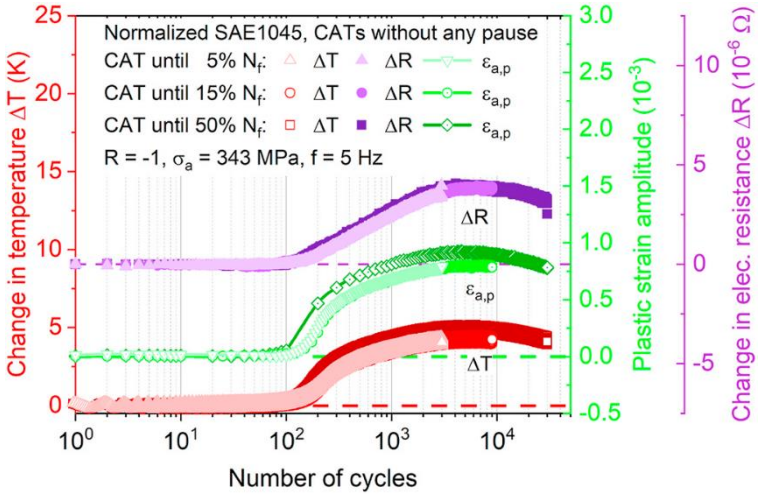

Fig. 7. Cyclic deformation curves based on the change in temperature (curves on the bottom), the plastic strain amplitude (curves in the middle) and the change in electrical resistance (curves on the top) determined from CATs at σ_a = 343 MPa until 5%, 15% and 50% of predicted N_f respectively. The number of cycles is displayed logarithmically.

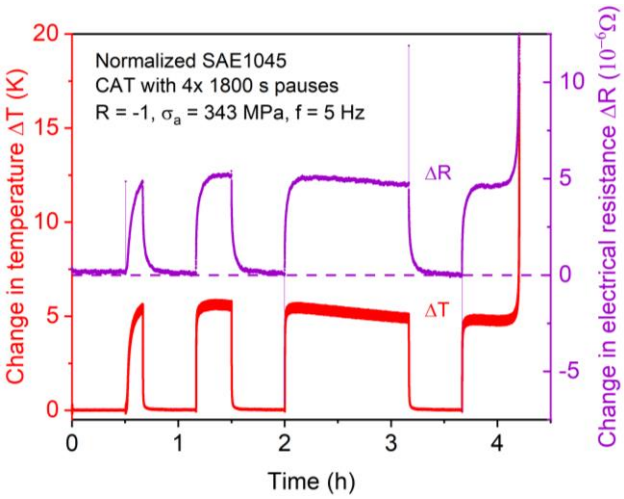

Fig. 8. Courses of the change in temperature and the change in electrical resistance of a CAT with load-free sequences (σ = 0 MPa) after incubation phase as well as after 5 %, 15 % and 50 % of N_f. The time is displayed linearly.

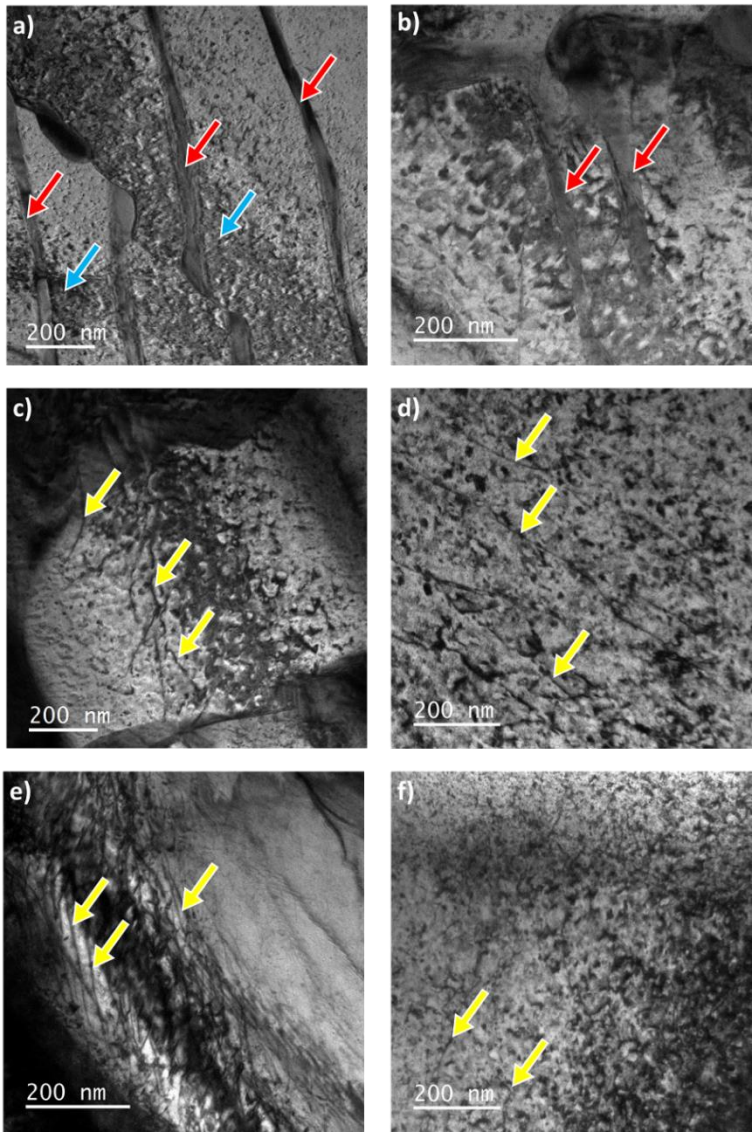

Fig. 9. Transmission electron microscopy (TEM) micrographs showing the dislocation structures for samples, after: (a)-(c) 0%; (d) 5%; (e)15%; and (f) 50 % of N_f from CATs with a stress amplitude of 343 MPa.

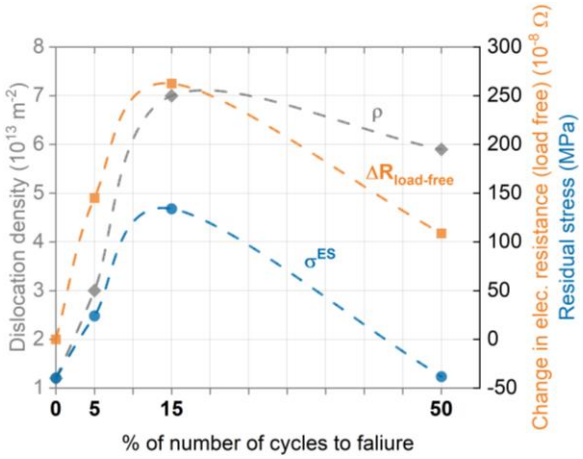

Fig. 10. Change in dislocation density, electrical resistance and residual stress with % of the number of cycles to failure (i.e., 0%, 5%, 15% and 50% of N_f). Data points are connected with smoothed trend lines.

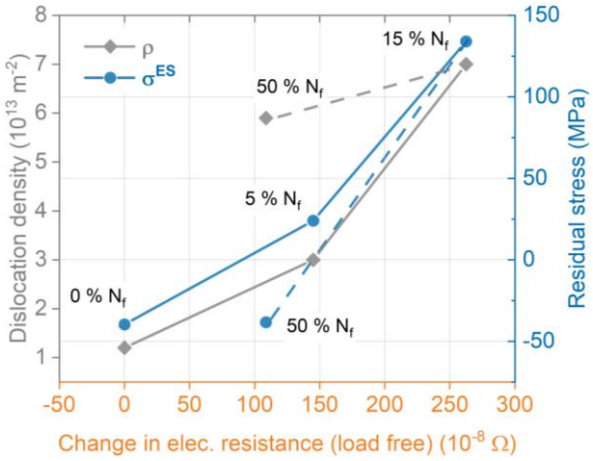

Fig. 11. Values of dislocation density and residual stress vs. the change in electrical resistance determined from specimens in the stage of 0%, 5%, 15% and 50% of N_f. Data points are connected with straight trend lines.

PAPER 5

Characterization and analysis of plastic instability in an ultrafine-grained medium Mn TRIP steel

Z.J. Teng*, H. Wu, S. Pramanik, K.-P. Hoyer, M. Schaper,

H.L. Zhang, C. Boller, P. Starke

In manuscript

Characterization and analysis and characterization of plastic instability in an ultrafine-grained medium Mn TRIP steel

Z.J. Teng[a,b,*], H. Wu[a,b], S. Pramanik[c], K.-P. Hoyer[c], M. Schaper[c], H.L. Zhang[d], C. Boller[a], P. Starke[b]

[a] *Chair of Non-Destructive Testing and Quality Assurance, Saarland University, Saarbrücken 66125, Germany*

[b] *Department of Materials Science and Materials Testing, University of Applied Sciences Kaiserslautern, Kaiserslautern 67659, Germany*

[c] *Chair of Materials Science, Paderborn University, Paderborn 33100, Germany*

[d] *Baoshan Iron & Steel Co., Ltd. & State Key Laboratory of Development and Application Technology of Automotive Steels (Baosteel), Shanghai 201900, China*

Abstract

This paper is focused on the mechanical and magnetic behavior of an ultrafine-grained (UFG) medium manganese (Mn) transformation-induced plasticity (TRIP) steel in its plastic instability. The in-situ methods of digital image correlation (DIC) and magnetic Barkhausen noise (MBN) are used to macroscopically characterize the propagation of the Lüders band (stretcher-strain marks) and the evolution of MBN activities during quasistatic tensile deformation. The evolution of microstructure during the plastic instability is ex-situ investigated using X-ray diffraction (XRD) and transmission electron microscopy (TEM) for selected plastic strain states. The results show that the plastic instability of this steel is associated with an increase of hardness and enrichment of dislocation density, which can also amplify the MBN signal, while the derived coercivity behaves reversely on an overall trend due to work hardening. The different stress response of the medium Mn steel is closely related to the kinetic martensite microstructure, which in turn modifies the domain-structure response. Thus, the MBN can be used as a potential means for non-destructive evaluation (NDE) for the strengthening of the UFG medium Mn TRIP steel.

Keywords: Medium manganese steel; Plastic instability; Magnetic Barkhausen noise; X-ray diffraction; Transmission electron microscopy

1. Introduction

The increasing demand for crashworthiness-improvement and weight-reduction in the automotive and other transportations vehicles has led to the development of the third generation of advanced high strength steels (AHSSs) [1,2]. Moreover, long-term use of lightweight steels can lead to a reduction in fuel consumption and thus detrimental emissions, contributing to carbon-neutrality targets in the longer term. Among those steels, the ultrafine-grained (UFG) medium Mn (3-12 wt.%) transformation-induced plasticity (TRIP) steels, containing retained γ-austenite islands or films dispersed in an α-ferrite or α′-martensite matrix, emerge a great potential to be a strong candidate due to its excellent strength, ductility, and toughness performance [3].

The TRIP effect leads to big advantages with respect to forming processes, being specifically relevant for automotive application. On the one hand, this includes hardening due to martensitic transformation and higher stiffness due to the forming of profiles on the other. The TRIP effect normally appears at higher strains during the tensile loading, where retained γ-austenite presented in the medium Mn steel transforms to α′-martensite resulting in high strength and elongation since the metastable austenite structure has higher ductility and a better ability to accommodate plastic strain. However, a discontinuous yielding phenomenon is the main drawback in such steels [4], which is to be observed from the yield point, followed by a stress plateau in the tensile stress-strain curve, where the Lüders band normally forms and propagates in such a stage. As a kind of plastic instability or localized deformation behavior, the Lüders band, which occurs in the tensile test is not desired in cases such as for automotive application, as such a behavior can deteriorate the surface quality of the material and result in an unexpected weakening of the material's structural stability and even premature failure in some cases [5]. Hence, such a plastic instability problem was investigated previously by a considerate number of studies with different characterization methods, e.g., in-situ measurements including digital image correlation (DIC) [5-7], neutron diffraction [8,9], infrared thermography (IRT) [5,6] and ex-situ methods like Electron Back Scatter Diffraction (EBSD) [10,11], X-ray diffraction (XRD) [12,13], as well as transmission electron microscopy (TEM) [14-16]. Moreover, the underlying mechanisms for the plastic instability of medium-Mn steel can be referred from the review literature [17,18]. Nowadays, non-destructive testing (NDT)

is in huge demand due to its enhanced capabilities for evaluating mechanical properties. With many of those techniques the operation becomes increasingly intuitive, the measurement is non-invasive, and can even be contactless. Amongst the wide range of NDT techniques, magnetic Barkhausen noise (MBN) has been chosen to characterize the plastic instability/work-hardening of the medium Mn TRIP steel analyzed along tensile tests to be presented here.

In contrast to ferromagnetic body-centered cubic (bcc) α-ferrite/body-centered-tetragonal (bct) α′-martensite, face-centered cubic (fcc) γ-austenite is paramagnetic. The cold-worked medium Mn TRIP steel therefore has detectable magnetic properties, which can be determined by MBN. MBN is emerged from the ferromagnetic materials through the discontinuous domain wall (DW) movements [19], which can be induced across a sample by applying a time-varying magnetic field. The MBN recorded in the form of an electrical voltage pulse, measured through applying a pick-up coil or any similar sensing device located near the sample's surface. Furthermore, the MBN is strongly influenced by the types and numbers of pinning sites of the domain walls within the material being tested, where the pinning sites act as barriers for the DW movement and are resulted of various microstructural defects, e.g., voids, inclusions, phase transformations, grain boundaries, and dislocations [20,21]. However, it is not easy to directly link the magnetic properties with the amount of deformation-induced martensite directly. The MBN is very sensitive to the microstructure and applied/residual stress. The lattice defects induced by strain hardening can temporarily pin the domain walls, and the high internal stress which is generated due to an incompatible phase transformation strain, can also affect the motion of the magnetic domain [22]. The gradual deformation-induced martensite transformation will increase the work hardening of the medium Mn TRIP steel, and the fine martensite grains that generate inside the austenite grains will make the dislocation movement more difficult [23]. Thus, monitoring the MBN properties can be helpful for the evaluation of the Lüders band formation or the deformation degree of medium Mn TRIP steel, even in the relatively early stages before the ultimate fracture, which seems to have been barely studied and understood, as can be concluded from lack of literature so far.

What follows, details of the experiments are presented first, which includes the material information, test procedures of in-situ DIC, MBN, and ex-situ XRD as well as

TEM. The MBN profile curves, dislocation densities, hardness, and phase content determined for selected strains are compared to find out, what changes in microstructural, mechanical, and magnetic properties occur, where the Lüders propagation is then given and discussed systematically. The results are discussed systematically to draw final conclusions.

2. Material and methods

An ultrafine-grained (UFG) medium Mn TRIP steel with a chemical composition of Fe-7Mn-0.14C-0.2Si (in wt.%) is studied in the current investigation. The steel was cold-rolled and annealed, in which the material was heated at a rate of 5 ℃/s until 620±15 ℃ was reached and then kept for 24 h in a nitrogen atmosphere protection. The intercritical annealing temperatures range from 593.7 ℃ (A1) to 691.3 ℃ (A3). After that, the steel was cooled in air to room temperature. The microstructure consists of two dominant phase contents: ferrite and retained austenite. The grain size of the annealed material is ~360 nm, and the overall γ-austenite has ~34.7% volume fraction measured by XRD. The inverse pole figure map and the phase map of the material are observed by EBSD as shown in Fig. 1. The magnetic domain images of the annealed material can be visualized by using magneto-optical Kerr effect microscopy (MOKE). Fig 2 shows the evolution of the intensity of the magnetic domain images at 4.96 mT, 19.97 mT, 35.01 mT, and 40.01 mT, respectively, with the range of magnetic field from -170 mT to 170 mT.

In this investigation, a standard dog-bone-shaped specimen with a gauge dimension of 35×6×1.4 mm^3 was designed and machined along the rolling direction from the annealed steel plate. The entire specimens' surfaces were polished to a mirror-like finish before uniaxial tensile tests were carried out with a universal tester (SHIMADZU AGS-X, 10 kN) and performed at a cross-head constant speed of 1 mm/min at room temperature.

The surfaces of the specimen-were speckled patterned with white and black paints to obtain a better contrast for the DIC measurement. To evaluate the strain distribution, optical photos of such prepared sample surfaces were taken at a framerate of 1 fps during the test. The kinematic strain field measurement was performed by a Canon 6D Market II camera with an EF 100mm f/2.8L IS USM lens.

The MBN was investigated by using a μmagnetic measurement system of QASS. The sinusoidal magnetic signal was excited at a frequency of 10 Hz with a coil voltage amplitude of 955 mV. Each excitation lasted 500 ms (5 cycles). The applied sensor was positioned with a minimal lift-off of ~0.3 mm, perpendicularly to the surface of the specimen. The raw signal was processed by selecting a region of interest (ROI) within a frequency band of 120 Hz -500 Hz, while denoising of the signal was made in both frequency and time domain. To avoid phase shift, only envelope curves were extracted rather than using a smoothing algorithm. The MBN signal peaks (unitless) and their positions (in mV regarding the coil voltage) were determined and used to characterize the microstructural changes on the specimens. The peak positions are considered to be correlated with the coercivity.

Quantitative XRD measurements were performed to examine the distribution and transition of the phases for the selected strains of the tensile deformation using a Seifert XRD 3000 PTS diffractometer equipped with monochromatic Cr Kα radiation (lambda = 2.2897 Å) with a scanning range (2θ) of 35°-160°. The voltage applied to the X-ray tube was 40 kV with a current of 40 mA in a scanning step of 2θ of 0.01°. The measured area was located in the middle center of the interrupted samples, however, for the final fractured sample, it was measured close to the fracture surface.

For the transmission electron microscopy (TEM) investigations, the samples from the gauge section after the interrupted tensile tests were thinned to a thickness of ~400 μm (Struers Secotom-5). The sides of the samples cut in rolling direction (RD) to the transverse direction (TD) were polished to a thickness of ~100 μm using abrasive papers. After that, disks with a diameter of 3 mm were punched from these samples. Electron transparent samples were prepared by twin jet electropolishing (Struers Tenupol-5). The electropolishing was conducted at 21 V, 18 mA, -21 °C using a solution with 5% perchloric acid and methanol. TEM was performed with a JEOL JEM-ARM 200F microscope operating at 200 kV acceleration voltage. For dislocation imaging, suitable tilting of the samples was undertaken in a double tilt sample holder. The sample thickness was measured using the energy-filtered transmission electron microscopy (EFTEM) mode. During EFTEM operation images of the same region were taken (i) using a 10-eV energy filter placed on the zero-loss peak and (ii) without an energy filter. For dislocation density calculation, equally spaced horizontal and vertical

lines were drawn on the TEM images of samples taken at the same magnification. The intersection points of the lines with dislocations were counted. Subsequently, the dislocation density was calculated by $\rho = 2N/Lt$ [24], where ρ is the dislocation density, N the total intersection points, L the total length of the horizontal and vertical lines, and the sample thickness.

3. Results and discussion

3.1. Mechanical behavior and damage

Two exemplary tensile stress-strain curves obtained at room temperature of the medium Mn TRIP steel tests are illustrated in Fig. 3. One of them was accompanied by DIC and the other by MBN measurement. The result shows a 0.2% offset stress of 1025 MPa, with total elongation of ~28%. Such excellent strength-ductility trade-offs have been reported elsewhere for the medium Mn steels having ultrafine-grained (UFG) microstructures [8,25,26]. Furthermore, this behavior is contributed from the deformation-induced $\gamma \rightarrow \alpha'$-martensitic transformation, where significant grain refinement and a high strain hardening rate occurs [27].

The material shows an elastoplastic behavior, after reaching the upper-yield point. Here, the stress rapidly decreases from 1060 MPa to 985 MPa (from point A to B) when strain is increased, with a small step in between, before this stress is becomes a nearly ~~a~~ constant value until a strain of 11.8% (from point B to C) is reached. Such stress plateau indicates the Lüders deformation behavior, of which the first Lüders strain of ~11% tensile elongation is measured as the strain magnitude of the stress plateau on the engineering stress-strain curve. After such a stress plateau, a slight strain softening and hardening occurs, and is noticeably followed by the second Lüders band formation, which reaches a strain of 23.5%, corresponding to point D, and then disappears. When the second pass of the Lüders band is over, the ultimate tensile strength of 1020 MPa is shortly achieved at a strain of 28%. Afterwards, necking occurs and is followed by a final failure.

The corresponding evolution of the 2D-distribution of the strain rate during the tensile test at selected points in time, calculated on the basis of the DIC results, is illustrated in Fig. 4a, while Fig. 4b highlights the details of the Lüders band nucleation

from a strain of 0.9% up to 1.65% sequentially in correspondence to Fig. 4a. It has been observed from a strain level at point B (Fig. 3), which corresponds to the lower-yield point at a strain of 0.9%, that a Lüders band nucleates first at the upper-right shoulder of the sample, and then develops across the gauge of the sample, showing a +60° angle to the tensile direction. After the band fully penetrates the width of the sample, a second band is initiated and develops through the first band, being inclined under -60° to the tensile direction. Hence, both overlapped bands form an X-shaped strain field in a localized region, which propagates continuously downwards and eventually stops at point C as to be seen in Fig. 3. By using a confocal microscope (Zeiss Smartproof 5), it can be observed, that the Lüders band (area C in Fig. 5) does extrude, forming a protrusion with larger positive measured values than the undeformed area B. When continuing to apply tensile deformation, such bands further nucleate, almost at the same former position, and then propagated similarly from the upper to the lower end of the gauge section and are stopped in the end at a strain level corresponding to point D in Fig. 3. After that, the X-shaped strain pattern shows up once again at the original position and stays saturated with necking until the final fracture. Such an observation suggests that the deformation-induced γ→α′-martensite transformation, which promotes the enhancement of strength and ductility through the TRIP effect.

One of the microscopic models of the occurrence of Lüders band are related to the Cottrell atmosphere, the formation of atmospheres around dislocations, which was proposed by Cottrell and Bilby [28]. It is postulated that the initial yielding needs high stress for pulling out of those atmospheres and be once released, the dislocations can be moved by lower stress. However, it is reported the Cottrell mechanism fails to explain the discontinuous yielding behavior in the current ultrafine-grained medium Mn steel in recent years [29-31]. With the help of advanced characterization technology, e.g., atom probe tomography [29] and in situ synchrotron high-energy X-ray diffraction [29,30], it is investigated that grain morphology and interface chemical decoration have direct influence on the yielding phenomenon in this air-cooled medium Mn steel grade. The rapid dislocation nucleation at the austenite-ferrite phase boundaries is responsible for the discontinuous yielding. The Lüders band governed elongation was explained in detail by Zhang [32], such as (1) Strain softening: The plastic instability emerges instantly once yielding occurs due to the UFG microstructure’s low work hardening

ability. This behavior results in a reduction in the cross-sectional area of the sample, and then an abrupt drop happens at the yielding point. With the development of inhomogeneous strain, deformation will then be localized in a narrow band; (2) Strain hardening: The TRIP effect induced by inhomogeneous strain is a very effective way to display the work-hardening ability. Such strain hardening counteracts the plastic instability and further restrain localized deformation; (3) Strain transfer: The inhomogeneous strain transfers from a hardened to an adjacent undeformed region, due to further localized deformation suppressed by the TRIP effect.

3.2. Variation in the magnetic Barkhausen noise

The variation in the curves of MBN signal intensities recorded versus coil voltage applied throughout the gauging zone is presented in Fig. 6a. The measurement was undertaken with a cyclic magnetization along the same direction in the sample as the tension stress was applied. It can be noticed, that the MBN intensity is highest in the unloaded condition, where no deformation has occurred. With increasing tensile deformation, the MBN signal intensity decreases as an overall trend. The variation of the MBN signal peak intensity and its peak position, where the peak position can be correlated to the coercivity of the material, were plotted together against the strain applied along the whole test procedure, as shown in Fig. 6b.

It can be recognized that the 180° domain walls grow at the expense of the 90° domain walls during the elastic deformation, and thus the more obvious DW motion leads to the higher MBN response [19]. The MBN signal intensity in the elastic regime decreases nearly linearly, this is attributed to the stress-sensitive feature of MBN, which results in the reduced peak height. In the plastic regime, as the deformation increases, the reduction continues, followed by a plateau until the end of the test. In the plastic instable stage until the first Lüders band initiation takes place, which corresponds to the region from point B to C in Fig. 3, the change in MBN signal intensity is of special interest. From the upper-yield point to the valley of the σ-ε curve at a strain of ~4%, the MBN peak value undergoes an irregular evolution, which may be caused by the stress relaxation of the compressive residual stress in the steel from the cold rolling process [33]. After that, the MBN peak value decreases continuously till the strain of 7.5% is reached and then fluctuates around ~9.5×10^3. The fluctuation of the MBN signal

intensity is likely to be related to the plastic flow during the tensile deformation, and the macroscopic phenomenon of the plastic flow observed can be correlated to the Lüders band propagation. The signal intensity of the MBN drops to a negligible value (not shown in Fig. 6) at the point where the specimen reaches final fracture, since the local magnetization is interrupted.

The hardness of the material increases with the elongation due to the increased dislocation density caused by tensile deformation and the thereon related cold work processes, which impedes the dislocation motion and works to harden the material [33]. The magnetic DWs can be held in place because of dislocation interactions or microstructural defects, so the magnetizing force is not strong enough to set the interactions free. Thus, the reduced DW motion will result in decreased Barkhausen activities [34]. This phenomenon is called the “pinning” of DWs, which was proposed by Kittel [35] and whose model takes the potential energy for the DW motion associated with the position to the potential obstacles, and further considers the inflexible wall whose motion is retarded by the defects density. If the defects are evenly distributed on both wall sides, then the force is zero, but otherwise, the force tends to move the wall to a more favorable position [19]. The plastic deformation creates an increase in dislocation which acts as the pinning site to the DW motion, and further increases the potential wells for DW motion [36].

The increase in hardness of the medium Mn steel is due to the increase in pinning density for the magnetic DW motion and dislocation motion by the deformation-induced martensitic transformation (DIMT) and the dislocation structures around the ferrite and martensite grains [33]. With the increase in $\gamma \rightarrow \alpha'$-martensitic transformation and the dislocation density during the tensile deformation, strong pinning for the magnetic DW motion will emerge to decrease the signal intensity of the MBN which increases the coercivity of the material. When the magnetic field strength is fixed and higher than the maximum saturation level of the material even at a high deformation, the Barkhausen activity would be effected by the magnetic domains, and those domains will have enough energy to free them from the pinning sites. Thus, the increased plastic deformation results in the reduced DW motion, and which will, in turn, reduce the Barkhausen activity at a fixed applied magnetic excitation field [19].

Magnetic materials with ultrafine grain normally reveal a high coercivity, because the high density of grain boundaries can provide more pinning sites for the DW motion [37]. Additionally, as mentioned above, the magnetic coercivity is a physical quantity reflecting the dislocation density, which prevents the reversible magnetic domain rotation if the applied magnetic field is not strong enough to free them from the pinning sites. Thus, the increased dislocation density will result in an increased coercivity [38], i.e., the coercivity can be used as a quantitative means to evaluate dislocation during tensile deformation of the medium Mn TRIP steel.

3.3. Microstructural changes along with the tensile deformation

The phase deformation and its resulting statistical analysis in terms of material characteristics can be supplied by XRD. The results for different states of the strain of the medium Mn steel are given in Fig. 7. The fcc austenite phase shows the diffraction peaks of {111}, {200}, and {220}, while the bcc ferrite/ bct martensite phases contribute the peaks of {110}, {200}, and {211}. As shown in Fig. 7a, as a result of the increasing tensile strain, the intensity of austenite peaks is decreased ({111} and {220}) and has even disappeared ({220}), while the intensity of ferrite/martensite peaks is increased with increasing tensile deformation. The volume fraction of retained austenite-V_γ was determined from the XRD analysis and decreased to ~9% at the final fracture as given in Fig. 7b, which indicates that a considerable portion of γ-austenite is transformed into α′-martensite. Hardness measurement with a load of 5 N and a holding time of 15 s was conducted on the samples using a Vickers hardness tester (Fig. 7b). It becomes obvious that the hardness of the samples increased due to the martensitic phase transformation, and the increased dislocation density, as to be seen with the tensile deformation increasing from 370 HV in the annealed condition to 427 HV in the final fracture state.

The microstructure of the specimen before the tensile test observed by TEM is shown in Fig. 8a, and enlarged in Fig. 8b, showing the region of interest marked in (a), which contains only a few grains. It is observed from the TEM images that the amount of dislocation contained in the microstructure is considerably low: a few dislocation lines emerge in the ferrite grain and barely appear in the neighboring grains. The dislocation density of the initial sample is ~2.5×10^{13} m^{-2}. Such a result is consistent with the

annealing process. It is therefore ensured that the initial dislocation density in the annealed material is at a reasonably low level before the Lüders deformation is reached.

It should be noted that the martensitic transformation is not the cause of the Lüders band. Martensitic transformation and Lüders band generation are two independent mechanisms, that happen simultaneously under certain applied stress conditions [25]. The deformation-induced γ→α′-martensite transformation normally results in z hard and brittle martensitic phase with high dislocation density and high density of geometrically necessary dislocations (GNDs) in adjacent ferrite grains [39]. Then the samples were individually analyzed using a TEM at different strain states, as shown in Fig. 9 for the phase with ongoing Lüders deformation (ε = 7%, 17%, 25%) as well as for the final fracture at 28%. It can be recognized from the microstructures that massive dislocations appeared in the deformed condition. Comparison of Fig. 9 with Fig. 8 allows to conclude, that the dislocation multiplications are on a very high level and lead to a high dislocation density generated during the Lüders band propagation. Thus, the reason why the deformation-induced γ→α′-martensitic transformation plays a role in the hardness increase, as shown before in Fig. 7b, is explained. The quantitative measurement of dislocations was conducted from the region of interest (ROI) of Fig. 8b and Figs. $9a_1$ to $9d_1$, and the dislocation density versus the tensile deformation diagram is given in Fig. 10, where both of the quantities are positively correlated, as discussed before. The dislocation density for the final fracture reached a very high value of $\sim 10^{14}$ m^{-2}. Thus, more and more magnetic DWs will get pinned or arrested in their position by the dislocation interactions and the magnetizing force is not high enough to set them free. Finally, the reduced domain motion will result in the decreased MBN [40].

In the high-level deformation, the high-density GNDs normally work as the obstacles to hinder the dislocation to slide in the ferrite grains and further provide the extra strain hardening ability. Furthermore, the plastic deformation of the martensite with high dislocation density will also increase the strain hardening ability [15]. Such a behavior has a very close relation to the MBN activity and affects coercivity. Moreover, the deformation-induced γ→α′-martensitic transformation provides a minor contribution to sustain the Lüders band propagation by dislocation strength for the UFG medium Mn TRIP steel investigated here.

4. Conclusions

The mechanical and magnetic behavior of UFG medium Mn TRIP steel has been investigated and presented here with the following main conclusions to be made:

1. Nucleation and propagation of Lüders bands in plastic instability – at least for the TRIP steel presented here – can be visualized and possibly also further quantified by using digital image correlation (DIC). The Lüders band-governed elongation can be correlated to the plastic instability, which includes strain-softening, strain hardening, and strain transfer.

2. Deformation-induced martensitic transformation (DIMT) during plastic instability was analyzed applying a transmission electron microscopy (TEM), which indicates that a minor contribution of this sustains the Lüders band propagation by dislocation strength and affects the deformation process of the Lüders band.

3. Phase content, hardness, and dislocation density of the samples at different selected strains, measured ex-in-situ, allows the evolution of DIMT during tensile deformation roughly to be quantified. This affects the pinning sites of the domain walls and can further help to understand the mechanical and magnetic behavior in the material exposed to tensile deformation.

4. DIMT behavior affects the MBN signal intensity and coercivity of the material. This non-destructive technique opens a wide range of possibilities to characterize and understand the deformation process in ferromagnetic materials, such as the UFG medium Mn TRIP steel.

Declaration of Competing Interest

The authors declare that they have no known competing financial interests or personal relationships that could have appeared to influence the work reported in this paper.

Acknowledgment

Z.J. Teng would like to acknowledge the support from China Scholarship Council. The authors also thank the Carl-Zeiss-Stiftung for the funding of the Kerr microscope

within the scope of the TELMa project and the University of Applied Sciences Kaiserslautern for the financial support with regard to further measurement technology.

Reference

[1] Benzing JT, Kwiatkowski da Silva A, Morsdorf L, Bentley J, Ponge D, Dutta A, Han J, McBride JR, Leer B, Gault B, Raabe D, Wittig JE. Multi-scale characterization of austenite reversion and martensite recovery in a cold-rolled medium-Mn steel. Acta Mater 2019; 166:512-530.

[2] Tan X, Ponge D, Lu W, Xu Y, He H, Yan J, Wu D, Raabe D. Joint investigation of strain partitioning and chemical partitioning in ferrite-containing TRIP-assisted steels. Acta Mater 2020; 186:374-388.

[3] Sun B, Krieger W, Rohwerder M, Ponge D, Raabe D. Dependence of hydrogen embrittlement mechanisms on microstructure-driven hydrogen distribution in medium Mn steels. Acta Mater 2020; 183:313-328.

[4] Sun B, Palanisamy D, Ponge D, Gault B, Fazeli F, Scott C, Yue S, Raabe D. Revealing fracture mechanisms of medium manganese steels with and without delta-ferrite. Acta Mater 2019; 164:683-696.

[5] Wang XG, Wang L, Huang MX. Kinematic and thermal characteristics of Lüders and Portevin-Le Châtelier bands in a medium Mn transformation-induced plasticity steel. Acta Mater 2017; 124:17-29.

[6] Wang XG, Wang L, Huang MX. In-situ evaluation of Lüders band associated with martensitic transformation in a medium Mn transformation-induced plasticity steel. Mater Sci Eng A 2016; 674:59-63.

[7] Qiu H, Inoue T, Ueji R. Experimental measurement of the variables of Lüders deformation in hot-rolled steel via digital image correlation. Mater Sci Eng A 2020; 790:139756.

[8] Zhang M, Li L, Ding J, Wu Q, Wang YD, Almer J, Guo F, Ren Y. Temperature-dependent micromechanical behavior of medium-Mn transformation-induced-plasticity steel studied by in situ synchrotron X-ray diffraction. Acta Mater 2017; 141:294-303.

[9] Kwok T, Rahman K M, Xu X, Bantounas I, Kelleher JF, Dasari S, Alam T, Banerjee R, Dye D. Design of a high strength, high ductility 12 wt% Mn medium manganese steel with hierarchical deformation behaviour. Mater Sci Eng A 2020; 782:139258.

[10] Yan S, Li T, Liang, T, Chen J, Zhao, Y, Liu, X. By controlling recrystallization degree: a plain medium Mn steel overcoming Lüders deformation and low yield-to-tensile ratio simultaneously. Mater Sci Eng A 2019; 758:79-85.

[11] Benzing JT, Liu Y, Zhang X, Luecke WE, Wittig JE. Experimental and numerical study of mechanical properties of multi-phase medium-Mn TWIP-TRIP steel: influences of strain rate and phase constituents. Acta Mater 2019; 177:250-265.

[12] Wang JJ, Hui WJ, Xie ZQ. Zhang YJ, Zhao XL. Influence of pre-strain on microstructural characteristics and tensile deformation behaviour of a cold-rolled Al-containing medium Mn steel. J Mater Sci 2020; 55:5296-5310.

[13] Jeong MS, Park TM, Choi S, Lee SJ, Han J. Recovering the ductility of medium-Mn steel by restoring the original microstructure. Scripta Mater 2021; 190:16-21.

[14] De Cooman BC, Gibbs P, Lee S, Matlock DK. Transmission electron microscopy analysis of yielding in ultrafine-grained medium Mn transformation-induced plasticity Steel. Metall Mater Trans A 2013; 44:2563-2572.

[15] Ma J, Liu H, Lu Q, Zhong Y, Wang L, Shen Y. Transformation kinetics of retained austenite in the tensile Lüders strain range in medium Mn steel. Scripta Mater 2019; 169:1-5.

[16] Wang XG, Liu CH, He BB, Jiang C, Huang MX. Microscopic strain partitioning in Lüders band of an ultrafine-grained medium Mn steel. Mater Sci Eng A 2019; 761:138050.

[17] Ma Y. Medium-manganese steels processed by austenite-reverted-transformation annealing for automotive applications. Mater Sci Tech 2017; 33:1713-1727.

[18] Lee YK, J. Han J. Current opinion in medium manganese steel. Mater Sci Tech 2015:31:843-856.

[19] O'Sullivan D, Cotterell M, Tanner DA, Mészáros I. Characterisation of ferritic stainless steel by Barkhausen techniques. NDT&E Int 2004; 37(6):489-496.

[20] Hristoforou E, Ktena A, Vourna P, Argiris K. Dependence of magnetic

permeability on residual stresses in alloyed steels. AIP Adv 2018; 8:047201.

[21] Lindgren M, Lepisto T. (2004). On the stress vs. Barkhausen noise relation in a duplex stainless steel. NDT&E Int 2004; 37:403-410.

[22] Haušild P, Kolařík K, Karlík M. Characterization of strain-induced martensitic transformation in a 301 stainless steel by Barkhausen noise measurement. Mater Design 2013; 44:548-554.

[23] O'Sullivan D, Cotterell M, Meszaros I. The characterisation of work-hardened austenitic stainless steel by NDT micro-magnetic techniques. NDT&E Int 2004; 37(4):265-269.

[24] Hirsch PB, Electron microscopy of thin crystals., Butterworths, 1965.

[25] Wang XG, He BB, Liu CH, Jiang C, Huang MX. Extraordinary lüders-strain-rate in medium Mn steels. Materialia 2019; 6:100288.

[26] Hu B, Luo H. A novel two-step intercritical annealing process to improve mechanical properties of medium Mn steel. Acta Mater 2019; 176:250-263.

[27] Somani MC, Juntunen P, Karjalainen LP, Misra RDK, Kyröläinen A. Enhanced Mechanical Properties through Reversion in Metastable Austenitic Stainless Steels. Metall Mater Trans A 2009; 40:729-744.

[28] Cottrell AH, Bilby BA. Dislocation theory of yielding and strain ageing of iron. Proc Phys Soc 1949; 62(1):49-62.

[29] Ma Y, Sun B, Schökel A, Song W, Ponge D, Raabe D, Bleck W. Phase boundary segregation-induced strengthening and discontinuous yielding in ultrafine-grained duplex medium-Mn steels. Acta Mater 2020; 200:389-403.

[30] Sun B, Ma Y, Vanderesse N, Varanasi RS, Song W, Bocher P, Ponge D, Raabe D. Macroscopic to nanoscopic in situ investigation on yielding mechanisms in ultrafine grained medium Mn steels: Role of the austenite-ferrite interface. Acta Mater 2019,178:10-25.

[31] Steineder K, Krizan D, Schneider R, Béal C, Sommitsch C. On the microstructural characteristics influencing the yielding behavior of ultra-fine grained medium-Mn steels. Acta Mater 2017; 139:39-50.

[32] Zhang Y, Ding H. Ultrafine also can be ductile: On the essence of Lüders band elongation in ultrafine-grained medium manganese steel. Mater Sci Eng, 2018; 733:220-223.

[33] Mohapatra JN, Akela AK. (2019). Magnetic evaluation of tensile deformation behaviour of TRIP assisted steels. J Nondestruct Eval 2019; 38:22.

[34] Buttle DJ, Scruby CB, Briggs GAD, Little EA, Jakubovics JP. Magnetoacoustic and Barkhausen emission in ferromagnetic materials. Phil Trans R Soc Lond A 1986; 320:363-378.

[35] Kittel C, Galt JK. Ferromagnetic Domain Theory. Solid State Physics 1956; 3:437-565.

[36] Astie B, Degauque J, Porteseil JL, Vergne R. Predictions of the random potential energy models of domain wall motion: An experimental investigation on high-purity iron. J Magnetism Magn Mater 1982; 28:149-53

[37] Zhang JS, Li W, Liao XF, Yu HY, Zhao LZ, Zeng HX, Peng DR, Liu ZW. Improving the hard magnetic properties by intragrain pinning for ta doped nanocrystalline ce-fe-b alloys. J Mater Sci Technol 2019; 35:1877-1885.

[38] Taylor RA, Jakubovics JP. Direct observation of the interaction between magnetic domain walls and dislocations in iron J Magnetism Magn Mater 1983;31-34: 970-972.

[39] Ramazani A, Mukherjee K, Schwedt A, Goravanchi P, Prahl U, Bleck W. Quantification of the effect of transformation-induced geometrically necessary dislocations on the flow-curve modelling of dual-phase steels. Inter J Plasticity 2013; 43:128-152.

[40] O'Sullivan D, Cotterell M, Cassidy S, Tanner DA, Mészáros I. Magneto-acoustic emission for the characterisation of ferritic stainless steel microstructural state. J Magn Mang Mater 2004; 271(2-3):381-389.

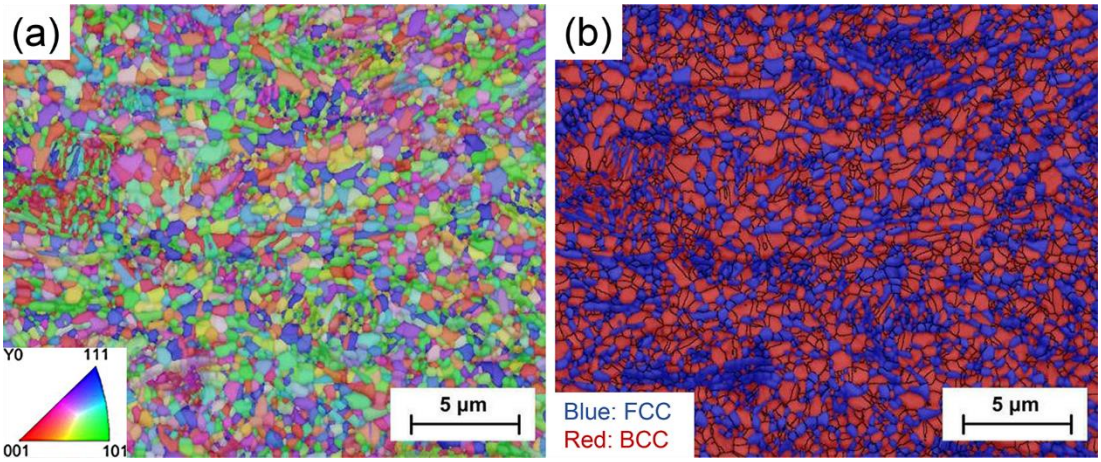

Fig. 1. Crystallographic characteristics of the medium Mn TRIP steel: (a) EBSD inverse pole figure map; (b) EBSD phase map, ferrite and austenite are represented by red and blue color, respectively.

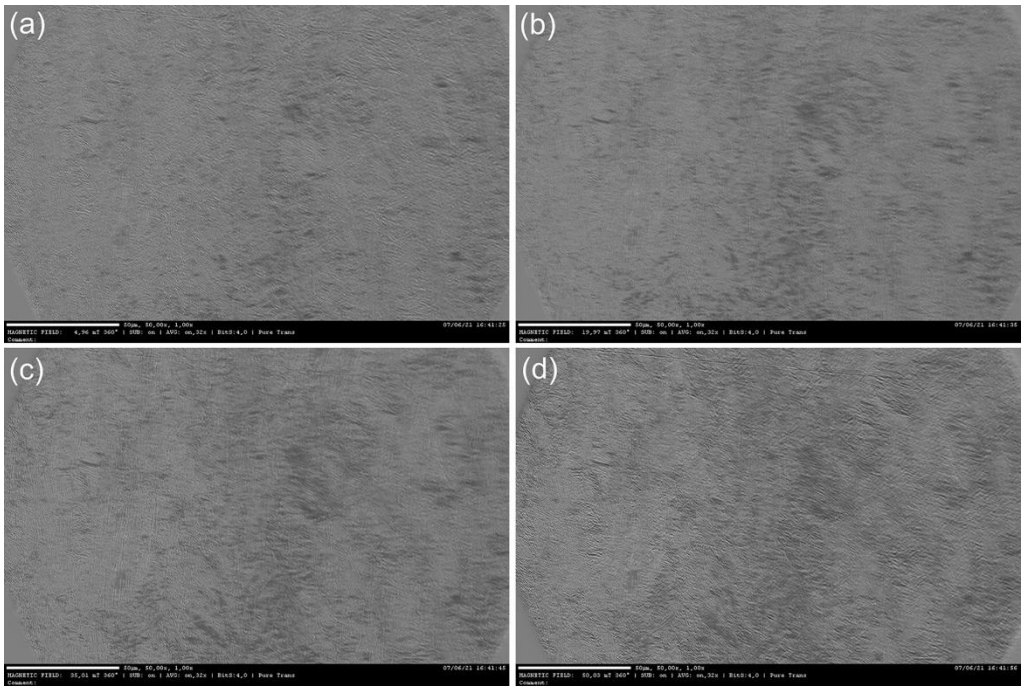

Fig. 2. The evolution of the intensity of magnetic domain images by using a Kerr-microscope at magnetic field of (a) 4.96 mT; (b) 19.97 mT; (c) 35.01mT; and (d) 40.01 mT, respectively.

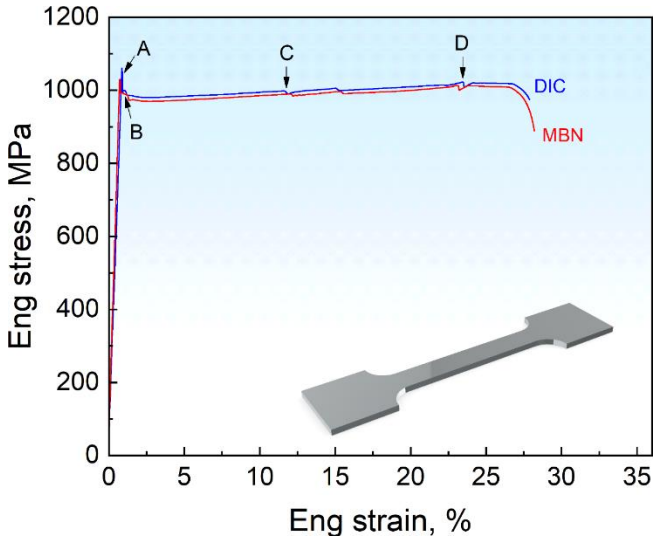

Fig. 3. Engineering stress-strain curves of the medium Mn TRIP steel obtained by tensile tests at room temperature until the rupture; and schematic geometry of the tensile specimen as the inset.

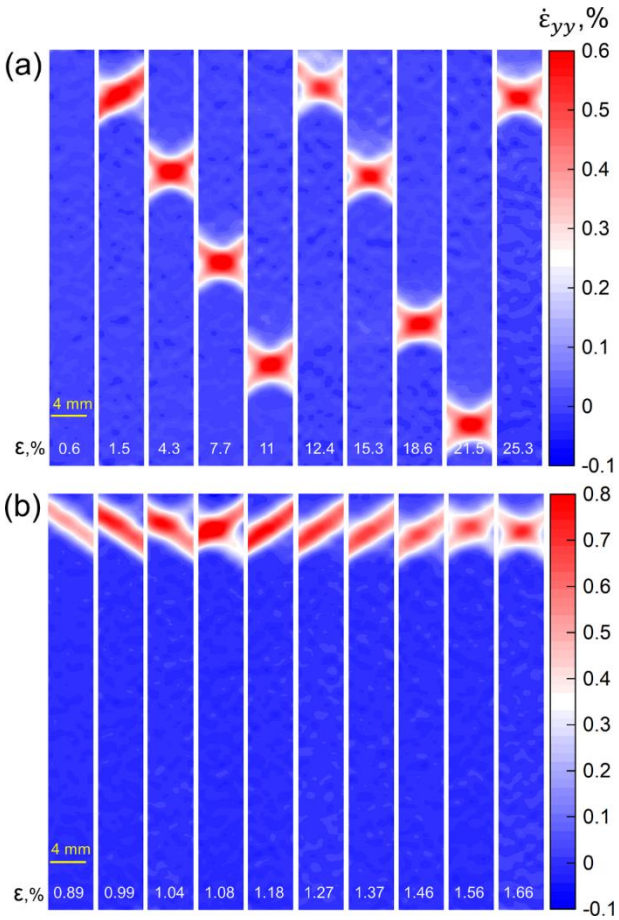

Fig. 4. (a) Ten strain-rate contour maps at the selected moments during the tensile test; (b) a succession of strain-rate contour maps at the selected moments during the Lüders band nucleation.

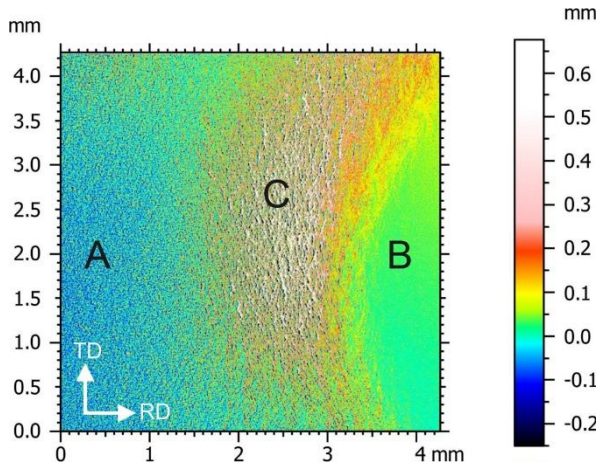

Fig. 5. Three-dimensional topography of the Lüders band and non-Lüders band areas within a 4.3×4.3 mm^2 area at a strain of 7%. The image is acquired by a confocal microscope. A and B represents the deformed and undeformed areas, respectively, while C the Lüders band.

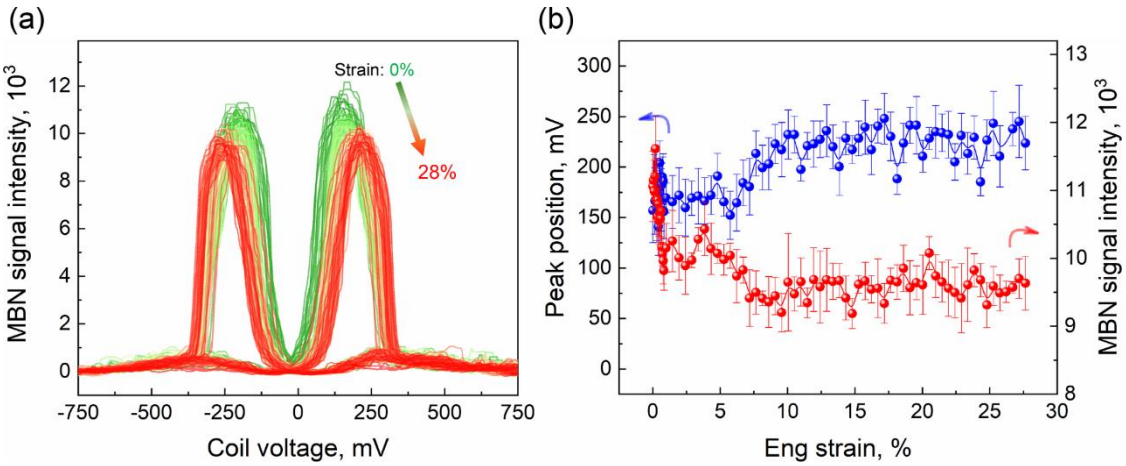

Fig. 6. (a) The MBN profiles measured at selected strains during the tensile test; (b) The MBN signal intensity and peak position versus the tensile strain.

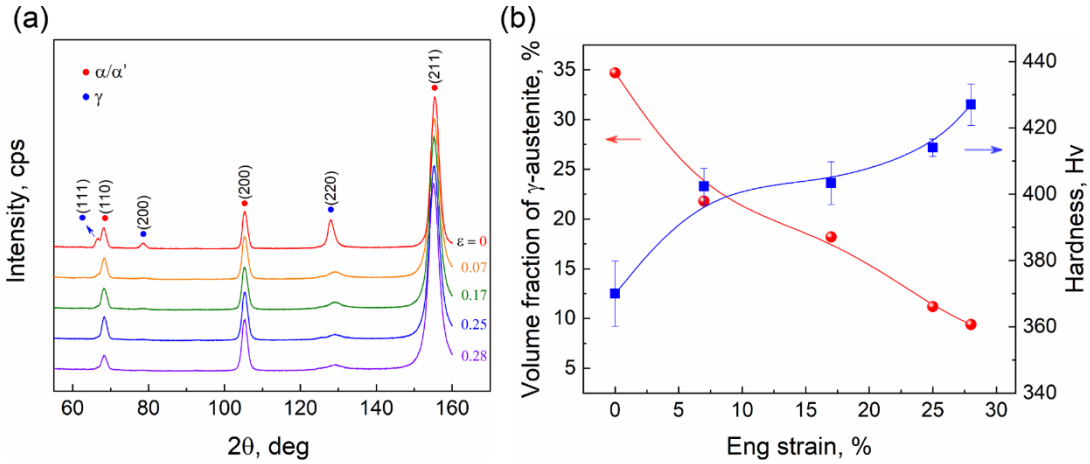

Fig. 7. (a) XRD spectra measured at selected strains of the as-received samples; (b) the transformation kinetics of retained γ-austenite measured from (a) and the corresponding statistical hardness of the samples.

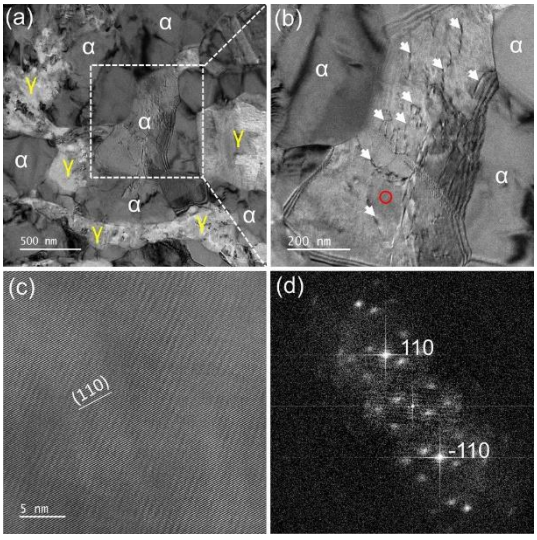

Fig. 8. (a) TEM bright-field image of the as-received specimen before the tensile test. α: ferrite, γ: austenite. (b) Magnified view of the white dashed rectangle marked in (a). The white arrows indicate the dislocations; (c) high-resolution TEM image taken from the grain containing dislocations of the red circular region marked in (b); (d) fast Fourier transformation of the high-resolution TEM image.

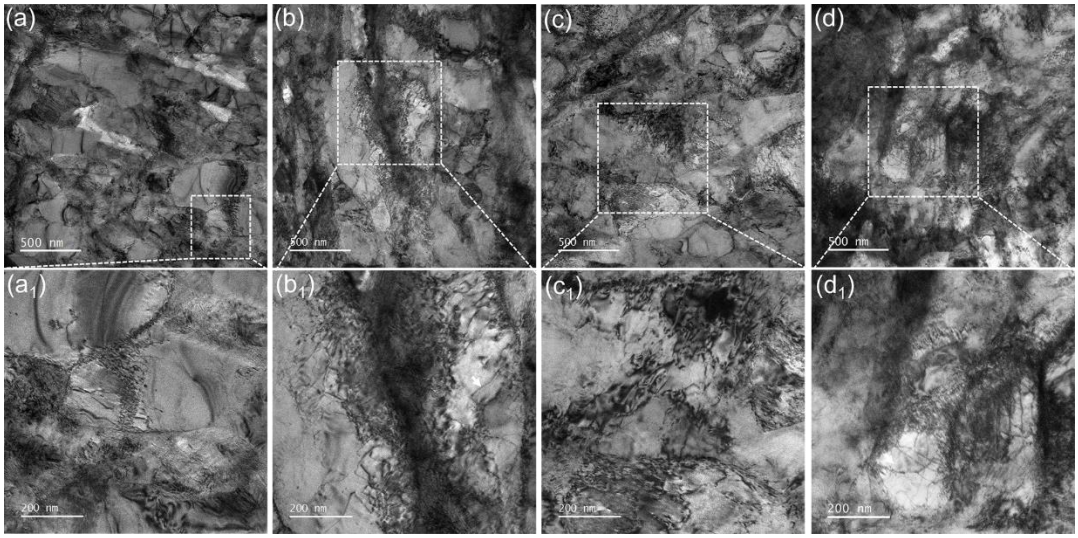

Fig. 9. TEM images showing the evolution of the microstructures at the selected strains of (a) 7%, (b) 17%, (c) 25%, (d) 28%, respectively. α/α′: ferrite or martensite, the white arrows indicate the dislocations.

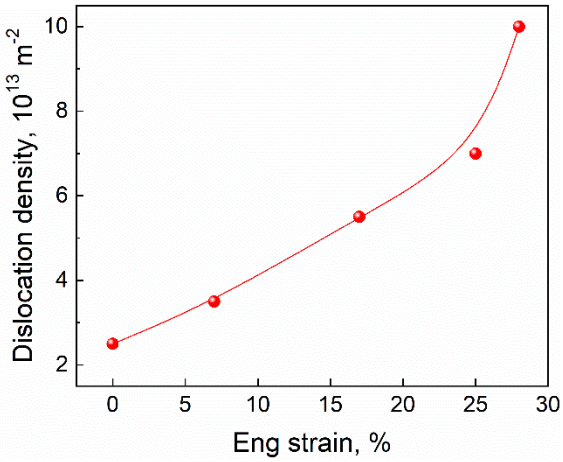

Fig. 10. The dislocation density at selected strains of the as-received samples.

Scientific Curriculum Vitae

Surname, First name	Date of Birth
Teng, Zhenjie	**18.10.1990**
Gender	Nationality
Male	**China**

Education Background:

2010.09 - 2014.06: Civil Aviation University of China, Bachelor of Safety Engineering

2014.09 - 2017.06: Sichuan University, Master of Solid Mechanics

2017.10 - 2022.03: Saarland University, PhD of Material Science and Engineering

Research Activities:

Fatigue & Fracture; Fatigue damage; Fatigue Life Calculation; Non-Destructive Testing; Fretting Fatigue

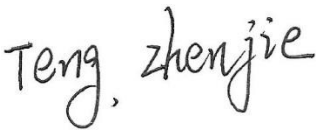

Saarbrücken, March 2022